ABSTRACT

Title of Document:	MESOSCOPIC THERMODYNAMICS IN SMOOTH AND CURVED INTERFACES IN ASYMMETRIC FLUIDS
	Heather Jane St. Pierre, Doctor of Philosophy, 2009
Directed By:	Professor Mikhail Anisimov Institute for Physical Science and Technology and Department of Chemical and Biomolecular Engineering

Phase separation has a significant impact on many chemical engineering applications, and since the phase transition of asymmetric one-component fluid or mixture interfaces can be gradual, or smooth, further analysis is warranted for fluid separation on the mesoscale. Complete scaling is applied to account for fluctuations in the critical region and to model the interfacial profiles of one-component and dilute binary mixtures, as well as calculate the curvature correction to the surface of tension (or Tolman length). Well-established symmetric profiles were selected for the order parameter and thermal scaling densities for use in complete scaling to model these asymmetric fluids. Real fluid asymmetry was applied to these profiles though the scaling coefficients of one-component fluids. Scaling coefficients for mixtures were introduced through the experimental critical parameters of the specific mixture;

characteristics accounted for included consideration of the difference in molar volume between solvent and solute, changes in critical temperature and pressure with concentration as well as the Krichevskii parameter. Flory theory was used to approximate the scaling coefficients in dilute polymer solutions to determine the Tolman length. These results indicated that Tolman's length diverges near the critical point of separation and with an increasing degree of polymerization. As an infinite degree of polymerization is approached, the Tolman length becomes half of the width of the interface. Since fluid behavior near the critical point of separation is universal, many of the theoretical expressions shown in this work can be applied to other asymmetric systems. The results of this analysis showed that a large difference in molecular volume led to a higher degree of fluid asymmetry in polymer solutions. The concentration of added solute, specifically in dilute *n*-heptane-ethane solutions resulted in increased fluid asymmetry in density profiles, as well as a shift toward the density of the added solute. When considering dilute mixtures of aqueous *n*-hexane and *n*-heptane-ethane solutions, a slight increase in concentration of solute, coupled with an increasing temperature distance to the critical point of separation, yielded the greatest increase in fluid asymmetry in concentration profiles.

MESOSCOPIC THERMODYNAMICS IN SMOOTH AND CURVED INTERFACES IN ASYMMETRIC FLUIDS

By

Heather Jane St. Pierre

Dissertation submitted to the Faculty of the Graduate School of the
University of Maryland, College Park, in partial fulfillment
of the requirements for the degree of
Doctor of Philosophy
2009

Advisory Committee:
Professor Mikhail A. Anisimov, Dept. of Chemical and Biomolecular Engineering, Chair
Professor Robert M. Briber, Dept. of Materials Science and Engineering
Professor Mohammed Al-Sheikhly, Dept. of Materials Science and Engineering
Professor Raymond A. Adomaitis, Dept. of Chemical and Biomolecular Engineering
Professor Sheryl H. Ehrman, Dept. of Chemical and Biomolecular Engineering

Acknowledgements

I would like to take the opportunity to thank the members of our research group, as all have provided invaluable thoughts and input. In particular, I would like to thank Chris Bertrand, as well as Daphne Fuentevilla and Deepa Subramanian for their incredible support throughout this process.

I also wish to thank the faculty and staff of the Chemical and Biomolecular Engineering Department for their assistance throughout this process. Specifically, I would like to thank my advisor, Professor Mikhail Anisimov for his guidance, patience and for keeping me motivated throughout this research, as well as Distinguished University Research Professor Jan Sengers for his guidance and review during completion of this work. Without them, this research would not have been possible.

Lastly, I would like to thank my husband, Eric, for his unending love and support throughout this research.

Table of Contents

List of Tables

List of Figures

Chapter 1: Introduction

The manner in which two phases separate from one another can have a significant impact on many engineering applications, whether these phases are the liquid and vapor phases of a pure (or one-component) fluid, or two phases of differing liquids. Directly related to interfacial phase separation is the concept of surface tension. Both interfacial behavior and surface tension are important for engineering applications when considering droplet formation, microemulsions, capillary action, nucleation, wettability, and fluid flow through micropores.

1.1 The Smooth Interface

In the study of interfaces, Gibbs[1] introduced the concept of the 'dividing surface,' which is an important baseline for establishing the location of where the surface of tension acts in a droplet.[2,3] In some fluids and on larger scales, the location of the 'dividing surface' can be the same as the 'thickness' or width of the interface between two fluids, where the interface is only on the order of the size of a molecule of fluid. This case is known as the 'sharp' interface, as the transition from one fluid phase to the other is very abrupt. In situations where the molecular size of a fluid is significantly large or the physical fluid properties are near the critical point of separation, the transition between two liquid phases becomes much more gradual, or smooth, shown in Fig. 1.1. In this figure, the darker color represents the gradient of the transition from one phase to another and the light color (or absence of color) indicates each of the bulk phases. This smooth interface illustrated in Fig. 1.1 is present in soft matter (i.e. polymer solutions and microemulsions) and in fluids near the critical point of separation.[4-9]

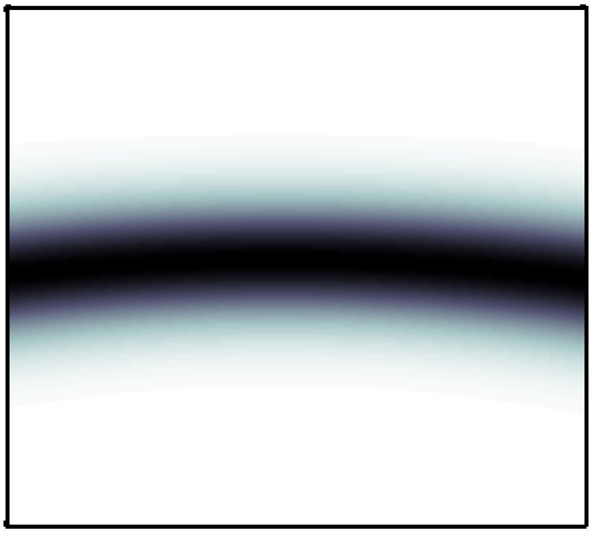

Figure 1.1. Simulated curved smooth interface of vapor-liquid separation in a droplet. The interface was simulated using toolboxes in MATLAB developed by Adomaitis[10] and Adomaitis and Chen.[11] The darker color indicates the steepest gradient of the interface of separation and the lightest color indicates the bulk phases on either side of the interface.

1.2 Surface Tension and Curved Smooth Interfaces

Many chemical engineering applications involve the formation or use of small droplets. For example, some targeted drug delivery systems utilize micro- or nanodroplets that form a flexible, biodegradable and hollow sphere into which a pharmaceutical can be inserted.[12,13] These tiny hollow spheres can be created dissolving a polymer in an immiscible solvent; this solution is then emulsified to form small droplets.[14] After the droplets are formed, the solvent is then removed from the polymer droplet through solvent evaporation, leaving behind hollow microspheres.[14]

Another example is the formation of aerosol micro- or nanodroplets for use in coatings. Ceramic coatings, due to their insulation and thermal properties, are of interest in many engineering applications. In order to create very thin ceramic films, small droplets must be used to create an ultra-fine spray. In one specific study, conducted by Balachandran, Miao and Xiao,[15] electrostatic atomization was used to generate 4-5 μm droplets of suspended ZrO_2 and SiC to create a homogeneous thin ceramic film on alloy substrates. Although there are countless other applications, given these engineering examples, it is important to recognize and account for the presence and behavior of smooth interfaces, especially in very small droplets.

Determining the surface tension at the separation boundary of small droplets that exhibit a smooth interface is not as straightforward as it might seem. In particular, the effects of curvature are typically considered negligible for surface tension on the macroscale. However, the curvature correction becomes increasingly more significant as applications and processes are scaled down, as has been the trend in many fields of engineering. As a result of downscaling, different physical effects and properties become more pronounced. One such effect is the curvature-correction to the surface tension.

In principle, the surface tension of a curved interface will behave differently than that of a planar interface,[2,3,16-31] but this curvature correction is typically ignored in engineering practice. This is mainly due to differing opinions regarding the net effect of curvature on the surface of tension, and as a result, the magnitude of this correction has been the subject of controversy for several decades.[2,12,18,20,22,24-28,30,32-43] In addition, when the mean-field approximation is used, the correction to the surface tension is insignificant, even when considering a nano-sized droplet.[44] However, more recent studies have shown convincing evidence to the contrary, indicating that this curvature correction can significantly alter surface tension calculations.[45]

1.3 Asymmetry and Its Effect on Interfacial Profiles

Another important concept in engineering applications is the impact of fluid asymmetry on the behavior of an interface. Whether or not a fluid is symmetric or asymmetric simply refers to the shape of its coexistence curve. If the phase coexistence is a symmetric parabola, the fluid is symmetric. Conversely, if the phase coexistence does not exhibit this symmetry, it is considered asymmetric. A simple illustration of an asymmetric phase diagram can be seen in Fig. 1.2. If the phase coexistence was completely symmetric in this figure, the coexistence would be a symmetric parabola about the critical point, denoted by the blue dot and critical density, ρ_c.

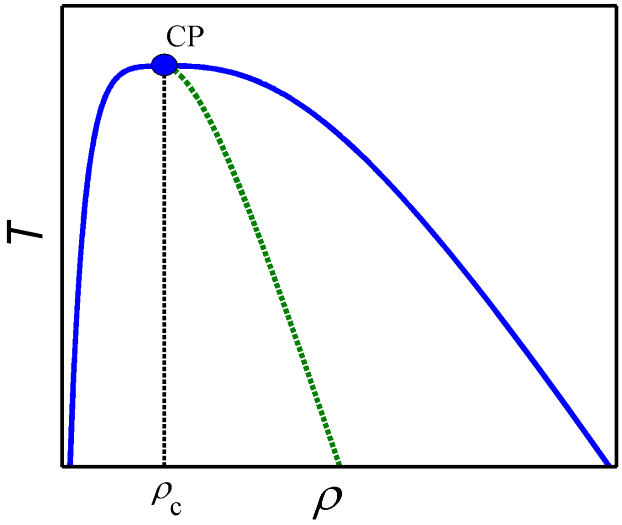

Figure 1.2. Schematic of an asymmetric vapor-liquid coexistence curve. The rectilinear (actual) diameter is given by the dashed green line.

Fluid asymmetry can be inherent both in pure (or one-component) fluids as well as in fluid mixtures. The addition of a small amount of solute to a one-component fluid with a vastly different molecular volume and chemical characteristics can result in new fluid asymmetry which can significantly impact the behavior of the mixture's interfacial profile.

Simple models, such as the lattice-gas model[46-48] offer means to model symmetric fluids and fluid mixtures, but do not account for asymmetry. Equations of state for a particular substance can account for fluid asymmetry, but may not accurately account for fluctuations near the critical point and can be particularly complicated if a significant amount of accuracy is desired. Therefore, we must look to a method that accounts for both asymmetry and fluctuations near the critical point of separation.

1.4 Methodology and Overview

In order to develop expressions to determine both the curvature correction to the surface tension and interfacial behavior of an asymmetric fluid, we must utilize a method that accounts for both fluctuations near the critical point of separation as well as fluid asymmetry. A method that has been shown to accurately model this behavior is known as 'complete scaling,' developed by Fisher and Orkulas[45] and Kim *et al.*[50]

Prior to exploring the results of complete scaling, the simple behavior of mean-field interfacial profiles will be addressed. The expressions for the mean-field interfacial profile and surface tension will be developed in Chapter 2 through a mesoscopic thermodynamic approach that utilizes the Landau-Ginsburg local free energy functional. As mean-field theories do not account for the effect of critical fluctuations, we must look to complete scaling to both account for these fluctuations and fluid asymmetry. The development of expressions describing one-component and binary fluid behavior using complete scaling will be shown in Chapter 3. The curvature correction to the surface tension, or Tolman's length,[2] and its implications will be discussed in Chapter 4. The near-critical and general thermodynamic expressions for Tolman's length will be presented as well.

Once the complete scaling approach has been presented, the behavior of real fluids can be approximated. As fluid asymmetry has been shown to be related to the Tolman length,[45,51] we will look to highly asymmetric fluids, such as polymer solutions, to further explore the magnitude of this correction in Chapter 5. Also in this chapter, the curvature correction will be addressed both near the critical point of separation as well as away from the critical region. These results will be used to develop a crossover expression for the Tolman length in polymer solutions.

As an alternative to the lattice-gas model, Chapter 6 provides the application of complete scaling to approximate the density and concentration profile behavior at the interface of asymmetric one-component fluids and dilute mixtures. Based on a good understanding of symmetric interfaces, as presented in Chapters 2 and 3, asymmetry specific to a fluid or fluid mixture will be applied through scaling coefficients used in complete scaling. Lastly, conclusions and potential future work will be presented in Chapter 7.

Chapter 2: Mean-Field Approximation of the Smooth Interface

The interface of phase separation provides insight as to how the surface of tension, a concept important to engineering calculations, will behave as it is highly dependent on intermolecular interactions. As a result, not all interfaces are the same. A smooth interface exists when there is a gradual change in concentration at the phase boundary between liquid-vapor or liquid-liquid separation, and is frequently observed in soft matter. Conversely, a 'sharp' interface exists when the change between two phases is very abrupt, much like a step function.

Smooth interfaces are present in near-critical liquid-vapor and liquid-liquid interfaces, in polymer solutions and polymer blends as well as liquid membranes and vesicles.[4-6,9,52,53] These interfaces can be represented by an interfacial density (or concentration) profile, which will be used to determine a characteristic length scale or interfacial "thickness." In order to determine this length scale, principles of mesoscopic thermodynamics will be utilized. For initial estimations of surface tension, density and concentration profiles, the effects of fluctuations near the critical point of phase separation will be ignored and mean-field—or van der Waals—theory will be used to approximate a symmetric smooth interface.

2.1 Determining the Local Helmholtz-Energy Density

While conventional statistical mechanics has been the longstanding methodology and basis for mesoscopic thermodynamics, other approaches that emphasize universality can be successfully applied to describe critical phenomena and interfacial density profiles. One such example of this approach is use of the Landau-Ginzburg functional. As fluctuations are prevalent in mesoscopic thermodynamics, we can consider a local—or coordinate-dependent—density of an appropriate thermodynamic potential in order to smooth these inhomogeneities.[50-52]

Because we are ultimately interested in calculating the surface tension, σ, we will start with the basic definition:

$$\sigma = \frac{d(\text{surface free energy})}{d(\text{area})}. \tag{2.1.1}$$

We can choose an appropriate thermodynamic potential, which in this case is the Helmholtz energy, because it is related to the property of interest. By using the total Helmholtz energy, $\underline{A}$, the following expression can be developed from Eq. (2.1.1):

$$\sigma = \frac{d(\Delta\underline{A})}{dxdy} = \rho_\mathrm{c} k_\mathrm{B} T \int_{-\infty}^{+\infty} \left[\text{local free energy density}\right] dz\,, \tag{2.1.2}$$

where $dxdy = d\Sigma$ for the surface, ρ_c is the critical density, k_B is the Boltzmann constant, and T is the temperature. The remaining unknown is the expression for the local free-energy density, and in our case, that is the local Helmholtz-energy density.

2.1.1 Landau Expansion and the Landau-Ginsburg Functional

To determine the local free energy density, we will review some basic definitions. The total Helmholtz-energy density, $\rho\underline{A}$, can be written as the integral taken over the total volume of the system:[55]

$$\rho\underline{A} = \int (\rho A) dV \,. \tag{2.1.3}$$

When integrated, the Helmholtz energy density can be considered as the sum of three terms, as indicated by the works of others:[57,58]

$$\rho \underline{A} = \Delta(\rho A) + \rho\mu_0(T, \rho = \rho_c) + A_0(T, \rho = \rho_c) \tag{2.1.4}$$

where the terms $\rho\mu_0$ and A_0 are two background terms that relate to the caloric properties and pressure, respectively. The last two terms on the right hand side of this equation are not affected by density fluctuations and are analytic functions of temperature and density. However, the first term, $\Delta(\rho A)$, is affected by local inhomogeneities, and, hence, density fluctuations and is therefore the function of interest.

Another important and related concept that addresses these inhomogeneities is the order parameter, φ. This position-dependent local order parameter is defined by an appropriate field-dependent thermodynamic potential. In the one-component fluid, density is the property of interest as it exhibits strong local fluctuations. Our dimensionless order parameter based on local density of the fluid is then defined as

$$\varphi(\vec{r}) \equiv \frac{\rho(\vec{r}) - \rho_\mathrm{c}}{\rho_\mathrm{c}}, \tag{2.1.5}$$

where $\rho(\vec{r})$ is the local density in three-dimensional space and ρ_c is the critical density.

The local Helmholtz-energy density can be expanded in powers of the order parameter and powers of gradient of the order parameter;[8]

$$\Delta(\rho A) = \rho_\mathrm{c} k_\mathrm{B} T_\mathrm{c} \int \left[\frac{1}{2} a_0 \Delta\hat{T} [\varphi(\vec{r})]^2 + \frac{1}{24} u_0 [\varphi(\vec{r})]^4 + \frac{1}{2} c_0 (\nabla\varphi)^2 \right] dxdydz, \tag{2.1.6}$$

where the dimensionless temperature distance to the critical point, $\Delta\hat{T}$, is defined as

$$\Delta\hat{T} \equiv \frac{T - T_c}{T_c}. \tag{2.1.7}$$

The remaining unknowns a_0 and u_0 are system-dependent coefficients, where u_0 reflects the energy of interaction between fluctuations,[59] and c_0 is a constant related to the range of intermolecular interactions.[8] These constants are also important in determining other thermodynamic quantities, and will be discussed in Section 2.5.

Note that the result in Eq. (2.1.7) takes into account that at the conditions that define the critical point, $\partial\mu / \partial\rho = \partial^2\mu / \partial\rho^2 = 0$, are met. In Eq. (2.1.6), the first terms within the brackets are a result of Landau expansion in terms of φ, and the last term is the result of expansion in powers of the gradient $\left(d\varphi / d\bar{r}\right)$. The entire bracketed expression is known as the Landau-Ginzburg functional for the local Helmholtz-energy density.[8] It should be noted that the order parameter symmetric, as is the Landau-Ginzburg functional.

In this specific case, the interest lies with the height-dependent coordinate, z, which gravity selects as the direction normal to the planar surface. Since only the bracketed portion of Eq. (2.1.6) can be re-written in terms of z, we can write the local Helmholtz-energy density, f as

$$f[\varphi(z)] = \frac{1}{2} a_0 \Delta\hat{T}[\varphi(z)]^2 + \frac{1}{4} u_0 [\varphi(z)]^4 + \frac{1}{2} c_0 \left(\frac{d\varphi}{dz}\right)^2. \tag{2.1.8}$$

Comparing this expression for the local Helmholtz-energy density to that in Eq. (2.1.6), you can see that this is merely the integrand in brackets in Eq. (2.1.6). In the previous equation, the definition of the order parameter (Eq. (2.1.5)) in terms of z only becomes

$$\varphi(z) \equiv \frac{\rho(z)-\rho_\mathrm{c}}{\rho_\mathrm{c}}. \tag{2.1.9}$$

The expression for the local Helmholtz-energy density in Eq. (2.1.8) can be simplified by carefully choosing values for the constants with physical meaning and by analyzing the derivatives, or conditions, of the order parameter and what it represents in terms of real physical properties. As with other thermodynamic potentials, the first derivative of the local Helmholtz energy determines the conditions for equilibrium, or chemical potential, when equal to zero: $df / d\varphi = \Delta\mu / k_\mathrm{B}T_\mathrm{c} = 0$. The second and third derivatives, when equal to zero, determine the spinodal (or region of instability) and critical point conditions, respectively. In the case of the local Helmholtz-energy density, only the portion of Eq. (2.1.8) from the expansion of powers of the gradient (i.e. the first and second terms) will be considered:

$$f_0 = \frac{1}{2}a_0\Delta\hat{T}[\varphi(z)]^2 + \frac{1}{4}u_0[\varphi(z)]^4. \tag{2.1.10}$$

The equilibrium, spinodal and critical point conditions are then:

$$\varphi_0 = \left(\frac{a_0(-\Delta\hat{T})}{u_0}\right)^{1/2} \quad \text{at} \quad \frac{df_0}{d\varphi} = 0 \tag{2.1.11}$$

$$\varphi_\mathrm{sp} = \left(\frac{a_0(-\Delta\hat{T})}{3u_0}\right)^{1/2} \quad \text{at} \quad \frac{d^2 f_0}{d\varphi^2} = 0 \tag{2.1.12}$$

and

$$\varphi_\mathrm{CP} = 0 \quad \text{at} \quad \frac{d^3 f_0}{d\varphi^3} = 0, \tag{2.1.13}$$

respectively. By applying the expression for the equilibrium condition in Eq. (2.1.11) to the local Helmholtz-energy density in Eq. (2.1.10), we can complete the square to simplify the equation so that

$$f_0 = \frac{1}{4} u_0 (\varphi^2 - \varphi_0^2)^2 - \frac{1}{4} u_0 \varphi_0^4 . \qquad (2.1.14)$$

The plot of this equation is given in Fig. 2.1, where $u_0 = 9/16$. This value of u_0 was chosen to match the equilibrium result in Eq. (2.1.11) along the mean-field coexistence curve for $a_0 = 9/4$ and facilitate completing the square in Eq. (2.1.14). This value is similar to the results of Anisimov and Sengers[60] and Agayan,[58] given the prefactors for each term in Eq. (2.1.8).

This 'extra' second term in Eq. (2.1.14) subtracted from the squared term represents the reference value of local Helmholtz-energy density. As this term is independent of density, it will not affect the overall shape or behavior of a dimensionless density profile. Therefore we will consider only the first term in Eq. (2.1.14), re-writing the expression as

$$f_0 = \frac{1}{4} u_0 (\varphi^2 - \varphi_0^2)^2 . \qquad (2.1.15)$$

The plot of Eq. (2.1.15) is given in Fig. 2.2. As expected, there is overlap at $\varphi = 0$ for sets of $\pm \Delta\hat{T}$ values when the reference value of local Helmholtz-energy density is included. In comparing these figures, it is important to note that the minima on the axis of the order parameter and shape of in each of the plots for a given temperature distance remain the same.

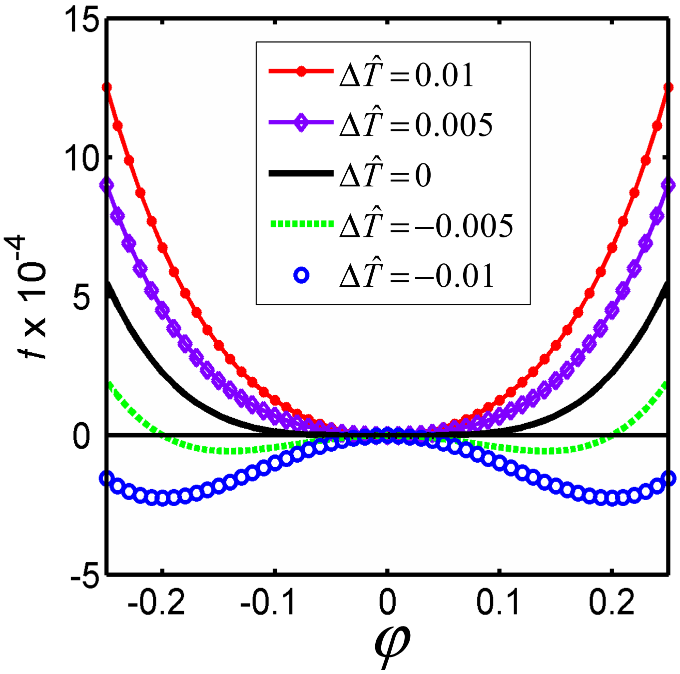

Figure 2.1. Local Helmholtz-energy density from Landau expansion (in terms of the order parameter) given in Eq. (2.1.14) for $u_0 = 9/16$ and varying temperature distances, $\Delta\hat{T}$.

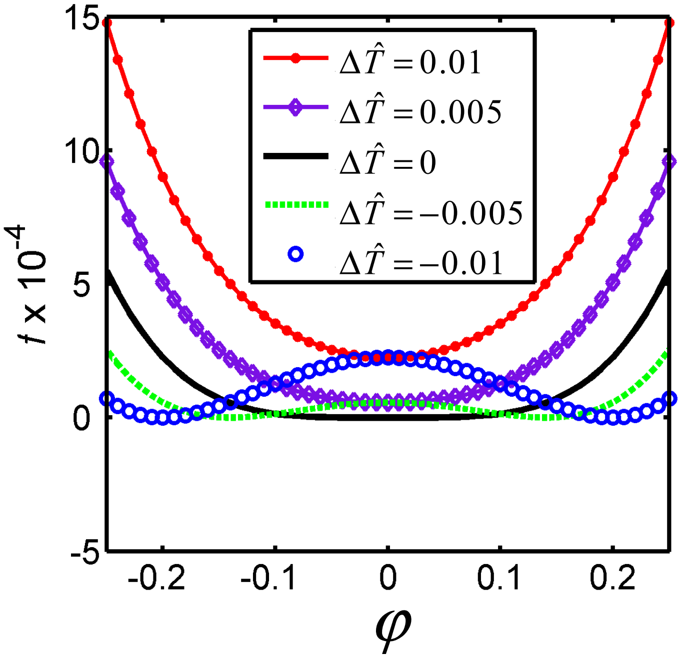

Figure 2.2. Local Helmholtz-energy density from Landau expansion (in terms of the order parameter) given in Eq. (2.1.15) – which includes the reference value for the local free energy density – for $u_0 = 9/16$ and varying temperature distances, $\Delta\hat{T}$.

Now that the first term in the local Helmholtz-energy density in Eq. (2.1.8) has reasonably been simplified to that in Eq. (2.1.15), the new full expression for the local Helmholtz-energy density becomes

$$f = \frac{1}{4}u_0[\varphi^2 - \varphi_0^2]^2 + \frac{1}{2}c_0\left(\frac{d\varphi}{dz}\right)^2 . \qquad (2.1.16)$$

Then the complete expression for the surface of tension (Eq. (2.1.2)) can be re-written as

$$\sigma = \frac{d(\Delta \underline{A})}{dxdy} = \rho_\mathrm{c} k_\mathrm{B} T_\mathrm{c} \int_{-\infty}^{+\infty} \left[\frac{1}{4}u_0[\varphi^2 - \varphi_0^2]^2 + \frac{1}{2}c_0\left(\frac{d\varphi}{dz}\right)^2 \right] dz \, , \qquad (2.1.17)$$

which will assist in simplifying future calculations.

2.2 Approximating the Density Profile near the Interface

Now that the expression for the surface of tension has been established, we can determine the interfacial or density profile for a symmetric fluid or fluid mixture. How can this interface be determined? The surface tension can be found by dividing the surface—or excess Helmholtz-energy—between two bulk phases, either vapor-liquid or liquid-liquid phases.[56] The inhomogeneous fluid maintains stability at the interface because the interfacial tension compensates for the unfavorable gain in Helmholtz energy between the two stable densities, explained by the two terms in the Landau-Ginzburg functional in brackets in Eq. (2.1.17). To maintain stability, the generalized local chemical potential must be constant along the interfacial profile, meaning

$$\frac{\mu(z)}{k_\mathrm{B} T_\mathrm{c}} = \frac{df}{d\varphi} = u_0 \varphi\left(\varphi^2 - \varphi_0^2\right) + c_0 \frac{d^2\varphi}{dz^2} = 0 \, . \qquad (2.2.1)$$

As a result, the quadratic and gradient terms must be equal to one another when considering the fluid characteristics below the critical point:

$$\frac{1}{4}u_0[\varphi^2 - \varphi_0^2]^2 = \frac{1}{2}c_0\left(\frac{d\varphi}{dz}\right)^2 . \tag{2.2.2}$$

This shows that to minimize the surface tension and attain a finite interface, a balance between a sharp interface and an infinitely diffuse interface between the two bulk-phase densities must be achieved.[56]

To determine the interfacial—or density—profile, Eq. (2.2.2) is simply solved in terms of the order parameter, or dimensionless density, φ:

$$\frac{\varphi}{\varphi_0} = -\tanh\left[z\varphi_0\left(\frac{u_0}{2c_0}\right)^{1/2}\right]. \tag{2.2.3}$$

Eq. (2.2.3) can also be re-written as

$$\frac{\varphi}{\varphi_0} = -\tanh\left[z\left(\frac{2c_0}{a_0(-\Delta\hat{T})}\right)^{-1/2}\right]. \tag{2.2.4}$$

This dimensionless profile can also be re-written in terms of the characteristic microscopic length scale related to the thickness of the interface, or ξ, which for the mean-field approximation is

$$\xi = \left(\frac{c_0}{2a_0(-\Delta\hat{T})}\right)^{1/2} = \bar{\xi}_0^-(-\Delta\hat{T})^{-1/2} . \tag{2.2.5}$$

Here, $\bar{\xi}_0^-$ is the mean-field amplitude of the correlation length below the critical point,

$$\bar{\xi}_0^- = \left(\frac{c_0}{2a_0}\right)^{1/2} , \tag{2.2.6}$$

and the bar denotes that this is the result for the mean-field approximation. Now the dimensionless interfacial profile can be written in terms of a dimensionless characteristic length scale, $z/2\xi$:

$$\frac{\varphi}{\varphi_0} = -\tanh\left[\frac{z}{2\xi}\right]. \tag{2.2.7}$$

The behavior of this mean-field profile can be seen in Fig. 2.3. Notice that the phase with the higher density, or larger value of φ/φ_0, has the lesser 'height' on the $z/2\xi$ axis. This represents the separation of two fluids with two differing densities. It should be noted that for the purposes of this analysis, the effect of gravity on an infinite planar interface, insofar that the height of the dividing surface along its horizontal axis will fluctuate as a result of capillary waves,[56,61] will be ignored.

2.3 Determining the Width of the Interface

As discussed previously, the characteristic length, ξ, was chosen as the length scale to determine the 'thickness' or width of the interface. There are methods to approximate the interface thickness; however, we can opt to choose multiples of this characteristic length as a unit to represent this width to model interfacial behavior, as the interfacial thickness may occur at a multiple[56] of ξ. The best and most accurate approximation of this 'thickness' from the mean-field approximation should be determined from the gradient of the interfacial profile, which will allow for better accuracy in calculating interfacial properties.

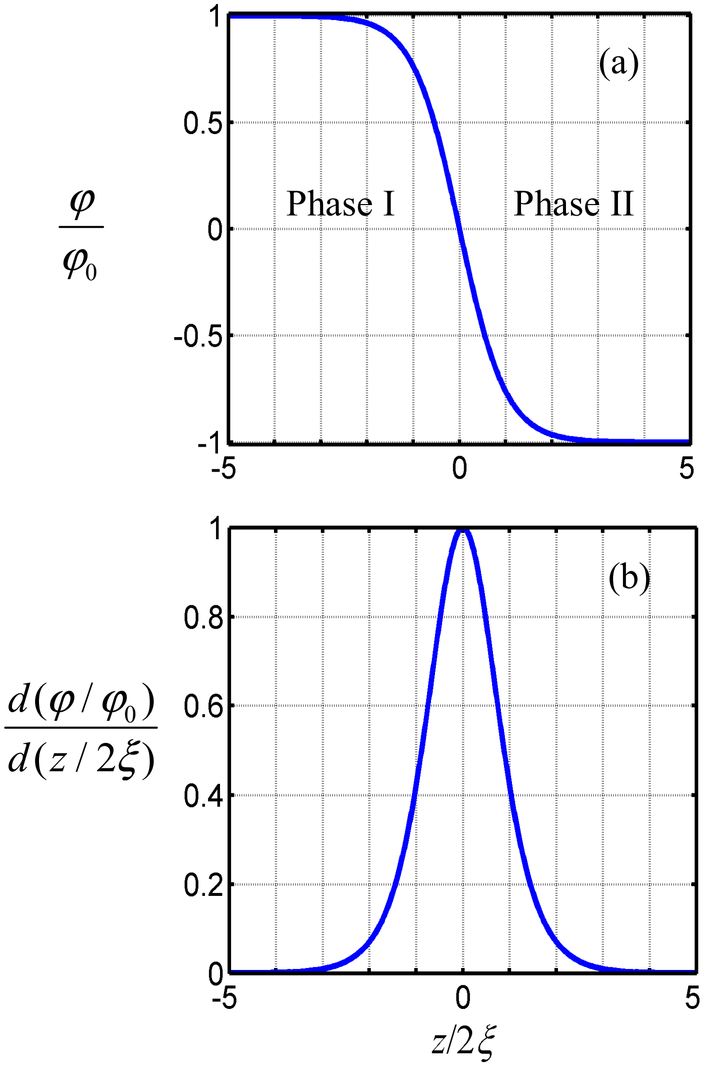

Figure 2.3. Mean-field dimensionless density profile (a) and gradient (b) as a function of height. The dimensionless density profile is given in Eq. (2.2.7) .

The gradient, or the probability of the location of the interface, can be seen by calculating at the slope of this density profile with respect to dimensionless height:

$$\frac{d(\varphi/\varphi_0)}{d(z/2\xi)} = -\operatorname{sech}^2\left(\frac{z}{2\xi}\right). \tag{2.3.1}$$

By looking at this gradient, the concept of the smooth, diffuse, or 'fuzzy' interface can be better visualized. As shown in Fig. 2.4, we see a smooth, gradual transition between both phases at their interface.

Also, in the case of the mean-field smooth interface in Fig. 2.4, the steepest gradient, and therefore the majority of the interface, lies between $\pm \xi$, yielding an approximated interfacial thickness of 2ξ. When looking at Fig. 2.3(b), it can be seen that nearly 95% of the gradient's behavior is accounted for between $\pm 2\xi$. Due to this difference, it is important to consider the behavior of the gradient when choosing the interface width in order to make the most accurate calculation.

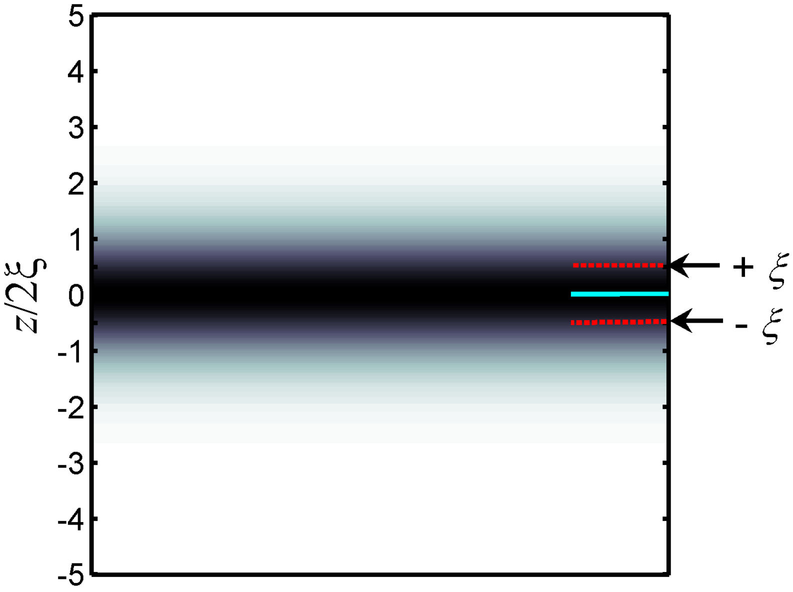

Figure 2.4. Contour plot of the interface between two fluid phases as predicted by mean-field theory. The shading indicates a larger slope of the density profile. The dotted red lines bound $\pm \xi$ and the solid blue line indicates $z / 2\xi = 0$.

2.4 Position and Density Dependence of the Local Helmholtz-Energy Density

We have discussed the equation for the symmetric smooth interfacial profile; however, it is important to remember that this determination was based on the local Helmholtz-energy density. Therefore, the behavior of the local Helmholtz-energy density itself should be noted. Considering the dependence on density and height, we can obtain a better understanding of the contribution of these individual effects.

Starting with the full equation for the local Helmholtz-energy density in Eq. (2.1.16), using the same approximation that the quadratic and gradient terms are equal as before, and inserting the expression for the interfacial profile in Eq. (2.2.7), we obtain

$$\frac{f}{\varphi_0^4} = \frac{1}{2} u_0 \left(\tanh^2\left(\frac{z}{2\xi} \right) - 1 \right)^2 . \tag{2.4.1}$$

This result is a universal dimensionless expression for the Helmholtz energy density. This is a universal equation as it is independent of temperature due to the arrangement of dimensionless groups. Its three-dimensional graphical representation, illustrating the individual dependences on density and height can be seen in Fig. 2.5.

Looking more closely at this figure, one can observe the individual affects of height and density on the local Helmholtz-energy density (given by the broken blue line), each contribute to the resultant mean-field interfacial profile, represented by the solid red line. The dotted gray and solid light blue lines show the individual effects of density and height, respectively, on the local Helmholtz energy density.

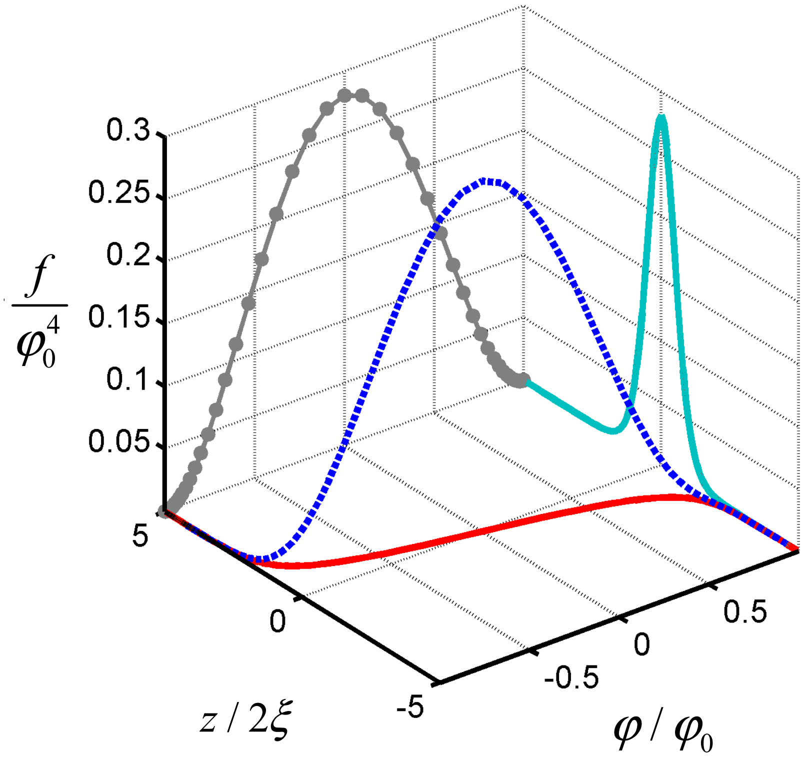

Figure 2.5. Three-dimensional universal plot of the dimensionless local Helmholtz-energy density (f / φ_0^4) and its dependence on height and density. The dimensionless local Helmholtz-energy density is given in Eq. (2.4.1). The solid red line shows the density profile in Eq. (2.2.7) and the dashed blue line indicates the dependence of f on both vertical position and density. The gray line with circles and the solid light blue line indicate the dependence of f on density and vertical position, respectively.

2.5 Mean-Field Estimation of Interfacial Tension

As we are ultimately interested in the behavior of the surface tension, there are several ways in which we can approximate the surface of tension based on the interfacial profile itself. For now, mean-field theory will be used to estimate this important engineering property.

Since we have a mean-field expression for the smooth interface, we can now develop expressions to estimate the interfacial tension based on the thermodynamic properties specific to the fluid. Referencing Eq. (2.1.17), the mean-field approximation for the dimensionless surface tension is

$$\frac{\sigma}{\rho_{\mathrm{c}} k_{\mathrm{B}} T_{\mathrm{c}}} = \int_{-\infty}^{+\infty} \left[\frac{1}{4} u_0 [\varphi^2 - \varphi_0^2]^2 + \frac{1}{2} c_0 \left(\frac{d\varphi}{dz} \right)^2 \right] dz \,. \tag{2.5.1}$$

In Section 2.2, it was discussed that the energy is minimized when the two terms within the integral were equal to one another. Therefore, we can safely make this approximation by doubling either the first or the second term in the bracketed expression as follows:

$$\frac{\sigma}{\rho_{\mathrm{c}} k_{\mathrm{B}} T_{\mathrm{c}}} = \int_{-\infty}^{+\infty} \left[\frac{1}{2} u_0 [\varphi^2 - \varphi_0^2]^2 \right] dz = \int_{-\infty}^{+\infty} \left[c_0 \left(\frac{d\varphi}{dz} \right)^2 \right] dz \,. \tag{2.5.2}$$

For the sake of simplicity, we will use the quadratic term to evaluate Eq.(2.5.1):

$$\frac{\sigma}{\rho_{\mathrm{c}} k_{\mathrm{B}} T_{\mathrm{c}}} = \int_{-\infty}^{+\infty} \left[\frac{1}{2} u_0 [\varphi^2 - \varphi_0^2]^2 \right] dz \,. \tag{2.5.3}$$

Since the integral will be evaluated in terms of φ, the second expression in Eq. (2.5.2) containing the gradient will be used to perform a change of variables, which results in

$$dz = \frac{d\varphi}{\left(\frac{1}{2} \frac{u_0}{c_0} \right)^{1/2} \left(\varphi^2 - \varphi_0^2 \right)} \,.$$

It is important to note that while performing this change of variables, the limits of integration change sign because $d\varphi / dz$ is negative (i.e. when height increases, the density of the fluid (φ) decreases). Substituting this information into Eq. (2.5.3) and integrating the expression for the dimensionless surface tension we obtain:

$$\frac{\sigma}{\rho_{\mathrm{c}} k_{\mathrm{B}} T_{\mathrm{c}}} = \frac{2\sqrt{2}}{3} \left(u_0 c_0 \right)^{1/2} \varphi_0^3 . \tag{2.5.4}$$

As mentioned in Section 2.1, these mean-field constants can be used to describe important thermodynamic properties that can be measured experimentally. The mean-field correlation length amplitude, given in Eq. (2.2.6) is one of those values. Another important definition is that of phase coexistence or equilibrium, as given by Eq. (2.1.11) for the simple mean-field approximation. Using this relation shown earlier, the mean-field condition

$$\varphi_{\mathrm{cxc}} = \bar{B}_0 \left| \Delta \hat{T} \right|^{1/2} , \tag{2.5.5}$$

where the mean-field amplitude of the phase boundary parabola, $\bar{B}_0$, is

$$\bar{B}_0 = \left(\frac{a_0}{u_0} \right)^{1/2} . \tag{2.5.6}$$

The last important property is the isochoric heat capacity, classically defined as

$$C_V = T \left(\frac{\partial S}{\partial T} \right)_{\rho} = -T^2 \left(\frac{\partial^2 A}{\partial T^2} \right)_{\rho} . \tag{2.5.7}$$

At the critical point, the isochoric heat capacity exhibits a finite jump at the critical temperature, which can be represented in the mean-field approximation by

$$\Delta \bar{C}_V = \frac{a_0^2}{2u_0} , \tag{2.5.8}$$

for the parameters in this work, similar to the methodologies use by others.[57,58,60,62] Substituting the thermodynamic properties in Eqs. (2.2.6), (2.5.6) and (2.5.8) into Eq. (2.5.4), the expression for the mean-field estimation of surface tension becomes:

$$\frac{\sigma}{\rho_{\mathrm{c}} k_{\mathrm{B}} T_{\mathrm{c}}} = \frac{8}{3} \bar{\xi}_0^- \bar{C}_V (-\Delta \hat{T})^{3/2} . \tag{2.5.9}$$

This result in Eq. (2.5.9) is the result for the mean-field approximation as determined by both Landau and Lifshitz[63] and Rowlinson and Widom.[56] The density gradient from Landau and Lifshitz's[63] work corresponds term by term with the expression in Eq. (2.2.2). The work of Rowlinson and Widom[56] defines the density of a fluid near the critical point, and the expression for the chemical potential of this fluid corresponds term by term to Eq. (2.2.1). These comparisons to both Landau and Lifshitz and Rowlinson and Widom are given in greater detail in Appendix A. This mean-field result for the approximation of the surface tension will be compared to other methods that take into account the effect of fluctuations near the critical point in Chapter 3.

Chapter 3: Accounting for Fluctuations near the Critical Point

3.1 Effects of Critical Fluctuations and Fluid Asymmetry

In the traditional approach of using the mean-field approximation, inter-particle interactions are assumed to be identical and independent of coordinate.[64] However, near the critical point of phase separation, the correlation length of fluctuations exceeds the range of intermolecular interactions, and can significantly modify the physical properties of the system. The result is that the interfacial profile becomes very smooth and therefore infinitely thick as the critical point is approached.[56] This also has implications for the surface tension of a smooth interface as it becomes low as a result of strong fluctuations.[7] Mean-field approaches to the thermodynamics of surfaces,[12,42,65-67] as presented in Chapter 2, ignore the effects of these local fluctuations.

A schematic illustrating the effects of these fluctuations near the critical point can be seen in Fig. 3.1. The actual, or singular, diameter (indicated by the broken green line in Fig. 3.1) is curved near the critical point, significantly departing from the mean-field diameter (indicated by the dotted red line). In this figure, you can see that the effect of critical fluctuations causes the actual diameter to be different from the rectilinear diameter, or arithmetic mean between vapor and liquid densities, and not only changes the shape of the coexistence curve near the critical point, but lowers the critical point as well.[68] As our desire is to make accurate calculations and approximations in the critical region, methods that account for this effect must be applied.

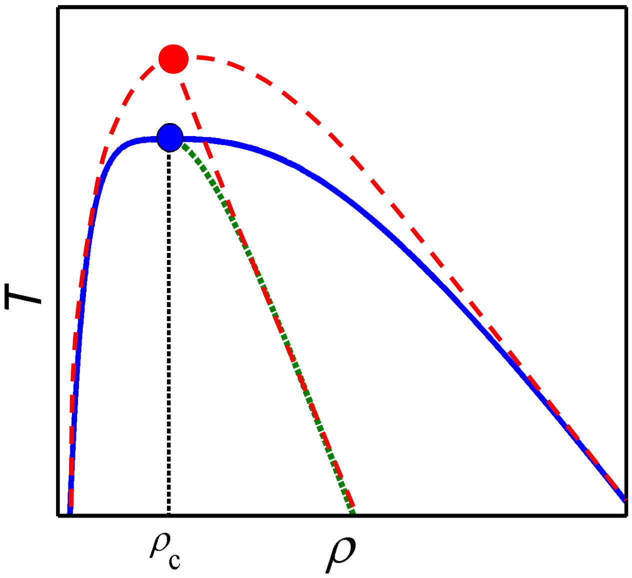

Figure 3.1. Schematic of an asymmetric vapor-liquid coexistence curve comparing mean-field (red lines) and scaling (blue and green lines) approximations near the critical point. The critical points are each represented by a circle. The dotted red line bisecting the curve represents the rectilinear (mean-field) diameter, the curved broken green line represents the actual (singular) diameter and the broken black line represents the actual critical density.

Another property that must be taken into account is fluid asymmetry, as it can impact the behavior of a fluid both near and far away from the critical point. This asymmetry is caused by the difference in interactions between phases of a single fluid or the difference in interactions between two or more kinds of molecules; the larger the differences, the larger the asymmetry.

In a symmetric system, such as the lattice-gas model with respect to density, the arithmetic mean of the coexisting densities, or 'diameter' of the coexistence curve, is a straight vertical line, indicating a symmetric parabola. In an asymmetric system, this 'diameter' is often curved near the critical point and becomes a sloped straight line.[68] The slope of this line can vary dependent on the shape of the coexistence curve, and an illustration of this concept can also be seen in Fig. 3.1. Note that for a symmetric system, the line of critical density (indicated by the broken black line in this figure) would also represent the arithmetic mean, whereas in an asymmetric system, the arithmetic mean (indicated by the green dashed line) would be sloped, similar to what is shown in Fig. 3.1.

3.2 Scaling Theory

One method of accounting for the effects of fluctuations as well as fluid asymmetry is known as scaling theory.[69] Scaling theory connects classical thermodynamics to experimental observations (thermodynamic space to experimental space). This theory accounts for the fact that near the critical point, all physical properties follow simple power laws, also referred to as scaling laws,[60] and the universal exponents used within these scaling laws are known as critical exponents.

Although various fluids and fluid mixtures display a wide range of behaviors, these critical exponents for analogous properties remain universal. Scaling theory establishes universal relationships between power laws, and a theory known as renormalization group theory provides a method to calculate these universal critical exponents. [69] The basis for both renormalization group and scaling theories is the divergence of the correlation length of the fluctuations in the order parameter near the critical point. The expression for the near-critical correlation length has been determined to be[56,64,70]

$$\xi = \xi_0 \left|\Delta\hat{T}\right|^{-\nu} \tag{2.2.1}$$

and Fisher and Zinn[70] and Pelisetto and Vicari.[71] have established $\nu \cong 0.630$. In this section and throughout this document, $\cong$ means approximately equal and $\approx$ means asymptotically equal.

3.2.1 General Scaling Equations

The critical behavior of real fluids and their mixtures can be asymptotically described by scaling theory;[72] in other words, a system's actual behavior can be related to that of a symmetric system. This behavior is described in terms of two independent fields, h_1 and h_2, and one dependent field, h_3. The 'ordering' or 'strong' field—the field that exhibits strong fluctuations—is represented by h_1; the 'thermal' or weakly fluctuating field is represented by h_2. These fields are all functions of physical fields in real space and can be combined into a form that can be used in a general case for fluids, using thermodynamic potentials expressed through conjugate order parameters. The general form for an equation of state for any fluid in terms of thermodynamic potentials is:

$$h_3 \approx |h_2|^{2-\alpha} f^{\pm}\left(\frac{h_1}{|h_2|^{2-\alpha-\beta}}\right), \qquad (2.2.2)$$

where $f^{\pm}$ is a scaling function.[51, 73] Within this function, the superscript $\pm$ refers to the sign of the independent field h_2, where $h_2 > 0$ references the region above the critical point and $h_2 < 0$ references that below the critical point. The critical exponents α and β are universal in terms of critical point universality; these exponents only depend on the type of scaling or modeling used and are independent of the specific fluid. The Ising values of $\alpha \cong 0.109$ and $\beta \cong 0.326$ have been well-established and verified experimentally.[70,71,74-77]

Related to the two independent fields (h_1 and h_2) are two conjugate scaling densities, φ_1 and φ_2, where φ_1 represents the strongly fluctuating order parameter and φ_2 represents the weakly fluctuating scaling density. These scaling densities are defined as:

$$\varphi_1 = \left(\frac{dh_3}{dh_1} \right)_{h_2} \tag{2.2.3}$$

and

$$\varphi_2 = \left(\frac{dh_3}{dh_2} \right)_{h_1} . \tag{2.2.4}$$

These fields and densities can be expressed in a differential form,[51,73]

$$dh_3 = \varphi_1 dh_1 + \varphi_2 dh_2 . \tag{2.2.5}$$

There are also three scaling susceptibilities, or second derivatives defined in terms of scaling densities: χ_1, the 'strong' susceptibility associated with strong fluctuations, similar to compressibility; χ_2, the 'weak' susceptibility associated with weak fluctuations, similar to heat capacity; and $\chi_{12,}$ the cross susceptibility. These are defined by the following equations:

$$\chi_1 = \left(\frac{d\varphi_1}{dh_1} \right)_{h_2} = \left(\frac{d^2 h_3}{dh_1^{\ 2}} \right)_{h_2} \tag{2.2.6}$$

$$\chi_2 = \left(\frac{d\varphi_2}{dh_2} \right)_{h_1} = \left(\frac{d^2 h_3}{dh_2^{\ 2}} \right)_{h_1} \tag{2.2.7}$$

and

$$\chi_{12} = \left(\frac{d\varphi_1}{dh_2} \right)_{h_1} = \left(\frac{dh_3^{\ 2}}{dh_1 h_2} \right)_{h_1} . \tag{2.2.8}$$

Since we are ultimately interested in modeling the equilibrium conditions of the interface, the simplification for zero ordering field ($h_1 = 0$) can be applied to the general scaling equations. Zero ordering field exists along the critical isochore and coexistence curve as shown in Fig. 3.2.

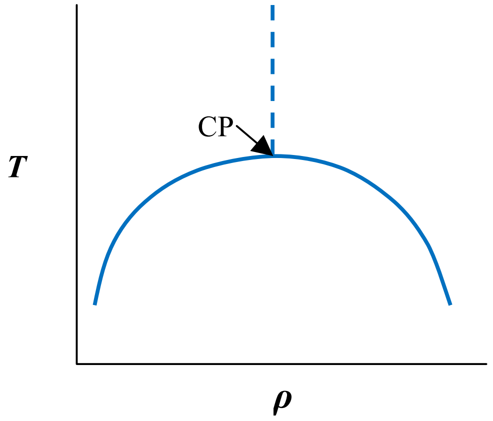

Figure 3.2. Schematic of a *T*-*ρ* diagram indicating the location of zero ordering field ($h_1 = 0$). The solid line represents the coexistence curve and the dashed line represents the critical isochore; both lines together represent $h_1 = 0$.

The expressions for the scaling densities (Eqs. (2.2.3) and (2.2.4)) and scaling susceptibilities (Eqs. (2.2.6), (2.2.7), and (2.2.8)) at zero order field become

$$\varphi_1 = \left(\frac{dh_3}{dh_1}\right)_{h_2} \approx f'(0)\left|h_2\right|^{\beta} \approx \pm\hat{B}_0\left|h_2\right|^{\beta} \tag{2.2.9}$$

$$\varphi_2 = \left(\frac{dh_3}{dh_2}\right)_{h_1} \approx (2-\alpha)f(0)h_2\left|h_2\right|^{-\alpha} \approx \frac{A_0^{\pm}}{1-\alpha}h_2\left|h_2\right|^{-\alpha} \tag{2.2.10}$$

$$\chi_1 = \left(\frac{d\varphi_1}{dh_1}\right)_{h_2} \approx f''(0)\left|h_2\right|^{2\beta+\alpha-2} \approx \hat{\Gamma}_0^{\pm}\left|h_2\right|^{2\beta+\alpha-2} \tag{2.2.11}$$

$$\chi_2 = \left(\frac{d\varphi_2}{dh_2}\right)_{h_1} \approx (1-\alpha)(2-\alpha)f(0)\left|h_2\right|^{-\alpha} \approx \hat{A}_0^{\pm}\left|h_2\right|^{-\alpha} \tag{2.2.12}$$

and

$$\chi_{12} = \left(\frac{d\varphi_1}{dh_2}\right)_{h_1} \approx \beta f'(0)\frac{\left|h_2\right|^{\beta}}{h_2} \approx \beta\hat{B}_0\frac{\left|h_2\right|^{\beta}}{h_2} \qquad (\text{for } h_2 < 0)\,. \tag{2.2.13}$$

Here, $\hat{B}_0$, the critical amplitude derived from the order parameter; $A_0^{\pm}$, the heat capacity amplitude; and $\hat{\Gamma}_0^{\pm}$, the susceptibility amplitude; are all system-dependent. As before, the $\pm$ superscript refer to $h_2 > 0$ and $h_2 < 0$, respectively. The $\pm$ sign in Eq. (2.2.9) refers to the two branches of the order parameter, $h_1 > 0$ and $h_1 < 0$, respectively, as they approach the limit $h_1 = 0$ at the phase boundary. These approximations in Eqs. (2.2.9)-(2.2.13) were verified against the work of Agayan.[60]

3.2.2 Complete Scaling for a One-Component Fluid

Now that the general scaling equations have been established, we can use the concept of complete scaling, as developed by Fisher[49] and Kim, Fisher and Orkoulas[50] to model the behavior of a pure fluid. Compared to the symmetric lattice-gas model, complete scaling has the ability to model the asymmetric behavior in real fluids though scaling coefficients. As our interest lies in the region near the vapor-liquid critical point, the independent theoretical scaling fields h_1 and h_2 can be written as linear combinations of physical fields. Therefore, in linear approximation, the scaling fields become

$$h_1 = a_1 \Delta\hat{\mu} + a_2 \Delta\hat{T} + a_3 \Delta\hat{P}, \tag{2.2.14}$$

$$h_2 = b_1 \Delta\hat{T} + b_2 \Delta\hat{\mu} + b_3 \Delta\hat{P}, \tag{2.2.15}$$

$$h_3 = c_1 \Delta\hat{P} + c_2 \Delta\hat{\mu} + c_3 \Delta\hat{T}, \tag{2.2.16}$$

where the sets of coefficients a_i, b_i and c_i represent the effects of asymmetry dependent on the type of fluid. The dimensionless physical fields in the previous equations are defined as

$$\hat{\mu} \equiv \frac{\mu}{k_{\mathrm{B}} T_{\mathrm{c}}} \qquad \Delta\hat{\mu} \equiv \frac{\mu - \mu_{\mathrm{c}}}{k_{\mathrm{B}} T_{\mathrm{c}}} \tag{2.2.17}$$

$$\hat{T} \equiv \frac{T}{T_{\mathrm{c}}} \qquad \Delta\hat{T} \equiv \frac{T - T_{\mathrm{c}}}{T_{\mathrm{c}}} \tag{2.2.18}$$

$$\hat{P} \equiv \frac{P}{\rho_{\mathrm{c}} k_{\mathrm{B}} T_{\mathrm{c}}} \qquad \Delta\hat{P} \equiv \frac{P - P_{\mathrm{c}}}{\rho_{\mathrm{c}} k_{\mathrm{B}} T_{\mathrm{c}}}. \tag{2.2.19}$$

Although they may appear to be complicated, the expressions in Eqs. (2.2.14)-(2.2.16) can be further simplified. Careful choice of the value of the dimensionless critical entropy, $\hat{S}_{\mathrm{c}}$, where[51,68]

$$\hat{S}_{\mathrm{c}} = \frac{S_{\mathrm{c}}}{k_{\mathrm{B}}} = \left(\frac{\partial P}{\partial T}\right)_{h_1=0,\mathrm{c}} (k_{\mathrm{B}}\rho_{\mathrm{c}})^{-1} = \left(\frac{d\hat{P}}{d\hat{T}}\right)_{\mathrm{cxc,c}} \tag{2.2.20}$$

allows the simplification of $c_3 = -\hat{S}_{\mathrm{c}}$. Using the value of the critical entropy in Eq. (2.2.20), the scaling coefficients can be further reduced. From thermodynamics and in terms of these dimensionless variables used in this section,

$$d\hat{P} = \hat{\rho}\, d\hat{\mu} + \hat{\rho}\hat{S}\, d\hat{T}. \tag{2.2.21}$$

Considering this expression in zero ordering field ($h_1 = 0$), we find that

$$\left(\frac{d\hat{P}}{d\hat{T}}\right)_{h_1=0,\mathrm{c}} = \left(\frac{d\hat{\mu}}{d\hat{T}}\right)_{h_1=0,\mathrm{c}} + \hat{S}_c,$$

therefore

$$\left(\frac{d\hat{\mu}}{d\hat{T}}\right)_{h_1=0,\mathrm{c}} = 0. \tag{2.2.22}$$

Also in zero ordering field close to the critical point,

$$\left(\frac{dh_1}{dT}\right)_{h_1=0,c} = 0 = a_1\left(\frac{d\hat{\mu}}{d\hat{T}}\right)_{h_1=0,\mathrm{c}} + a_2\left(\frac{d\hat{T}}{d\hat{T}}\right)_{h_1=0,\mathrm{c}} + a_3\left(\frac{d\hat{P}}{d\hat{T}}\right)_{h_1=0,\mathrm{c}}.$$

Therefore, based on the results in Eq. (2.2.22)

$$a_2 = -a_3 \left(\frac{d\hat{P}}{d\hat{T}} \right)_{h_1=0,\mathrm{c}} . \tag{2.2.23}$$

Since only two of the physical fields are independent in each of the equations for the thermodynamic fields, only two of the coefficients in each equation are independent. Eq. (2.2.14) can be significantly simplified[51,68] as the coefficients a_1 and b_1 can be absorbed by the scaling amplitudes in $f^{\pm}$, allowing $a_1 = b_1 = 1$. Therefore, the simplified scaling equations for a one-component fluid become

$$h_1 = \Delta\hat{\mu} + a_3 \left[\Delta\hat{P} - \left(\frac{d\hat{P}}{d\hat{T}} \right)_{\mathrm{cxc,c}} \Delta\hat{T} \right] \tag{2.2.24}$$

$$h_2 = \Delta\hat{T} + b_2\Delta\hat{\mu} + b_3\Delta\hat{P} \tag{2.2.25}$$

and

$$h_3 = \Delta\hat{P} - \Delta\hat{\mu} - \left(\frac{d\hat{P}}{d\hat{T}} \right)_{\mathrm{cxc,c}} \Delta\hat{T} . \tag{2.2.26}$$

In many cases, the scaling coefficients a_3 and either b_2 or the sum $b_2 + b_3$ can be approximated or determined experimentally.

We can use the definition in Eq. (2.2.20) and the result in Eq. (2.2.22) to re-write the temperature derivative of h_2 in Eq. (2.2.15), which becomes

$$\left(\frac{dh_2}{d\hat{T}} \right)_{h_1=0,\mathrm{c}} = 1 + b_3 \left(\frac{d\hat{P}}{d\hat{T}} \right)_{h_1=0,\mathrm{c}} . \tag{2.2.27}$$

Therefore, by integration of Eq. (2.2.27) and incorporating the results in Eq. (2.2.23), the results for zero ordering field are

$$\begin{aligned} h_1 &= 0 \\ h_2 &= \Delta\hat{T}\left(1 - b_3\frac{a_2}{a_3}\right) \\ h_3 &= \Delta\hat{P} - \Delta\hat{\mu} - \hat{S}_{\mathrm{c}}\Delta\hat{T}. \end{aligned} \tag{2.2.28}$$

It is important to note that the expression for h_2 in Eq. (2.2.28) can be further simplified by considering basic thermodynamic definitions in terms of the dimensionless variables established thus far:

$$\hat{\rho} = \frac{\rho}{\rho_{\mathrm{c}}} = \left(\frac{d\hat{P}}{d\hat{\mu}}\right)_{\hat{T}} \qquad \text{and} \qquad \hat{\rho}\hat{S} = \frac{\rho S}{\rho_{\mathrm{c}} k_{\mathrm{B}}} = \left(\frac{d\hat{P}}{d\hat{T}}\right)_{\hat{\mu}}. \tag{2.2.29}$$

Considering Eqs. (2.2.5) and (2.2.20), the differential expression for h_3 in Eq. (2.2.28) can be solved in terms of the dimensionless entropy density in Eq. (2.2.29):

$$dh_3 = d\hat{P} - d\hat{\mu} - \hat{S}_{\mathrm{c}} d\hat{T} = 0 + \varphi_2\left(1 + b_3\hat{S}_{\mathrm{c}}\right) d\hat{T}$$

$$\left(\frac{d\hat{P}}{d\hat{T}}\right)_{\hat{\mu}} - \left(\frac{d\hat{\mu}}{d\hat{T}}\right)_{\hat{\mu}} - \hat{S}_{\mathrm{c}}\left(\frac{d\hat{T}}{d\hat{T}}\right)_{\hat{\mu}} = \varphi_2\left(1 + b_3\hat{S}_{\mathrm{c}}\right)\left(\frac{d\hat{T}}{d\hat{T}}\right)_{\hat{\mu}}$$

$$\hat{\rho}\hat{S} = \left(\frac{d\hat{P}}{d\hat{T}}\right)_{\hat{\mu}} = \hat{S}_{\mathrm{c}} + \varphi_2\left(1 + b_3\hat{S}_{\mathrm{c}}\right). \tag{2.2.30}$$

This follows that by the definition of the dimensionless entropy density,

$$\Delta\left(\hat{\rho}\hat{S}\right) = \hat{\rho}\hat{S} - \hat{\rho}_{\mathrm{c}}\hat{S}_{\mathrm{c}} = \hat{\rho}\hat{S} - \hat{S}_{\mathrm{c}}$$

the result in Eq. (2.2.30) yields:

$$\Delta\left(\hat{\rho}\hat{S}\right) = \varphi_2\left(1 + b_3\hat{S}_{\mathrm{c}}\right) \tag{2.2.31}$$

indicating that the entropy density is proportional to the weakly fluctuating scaling density, φ_2. As shown here, and as discussed by Wang and Anisimov,[68] the coefficient b_3 does not appear to play a significant role in affecting fluid asymmetry and was assumed to be zero. However, later works by Wang *et al.*[51] consider and include the effects of b_3 in an effective constant, b_{eff} such that

$$b_{\mathrm{eff}} = \frac{b_2 + b_3}{1 + \hat{S}_{\mathrm{c}} b_3} . \tag{2.2.32}$$

3.2.3 Complete Scaling for a Dilute Binary Mixture

Another case that can be modeled by complete scaling is a dilute binary fluid mixture. As two components are now being considered, an additional field is considered in the linear combination of the scaling fields near the critical point, namely the exchange chemical potential ($\hat{\mu}_{21}$), such that

$$h_1 = \Delta\hat{\mu}_1 + a_2 \Delta\hat{T} + a_3 \Delta\hat{P} + a_4 \Delta\hat{\mu}_{21} , \tag{2.2.33}$$

$$h_2 = \Delta\hat{T} + b_2 \Delta\hat{\mu}_1 + b_3 \Delta\hat{P} + b_4 \Delta\hat{\mu}_{21} , \tag{2.2.34}$$

$$h_3 = c_1 \Delta\hat{P} + c_2 \Delta\hat{\mu}_1 + c_3 \Delta\hat{T} + c_4 \Delta\hat{\mu}_{21} . \tag{2.2.35}$$

Here, $\Delta\hat{\mu}_1 = (\mu_1 - \mu_{1\mathrm{c}}) / k_{\mathrm{B}} T_{\mathrm{c}}$ where μ_1 is the chemical potential of the pure solvent and $\Delta\hat{\mu}_{21} = (\mu_{21} - \mu_{21\mathrm{c}}) / k_{\mathrm{B}} T_{\mathrm{c}}$, where μ_{21} is the difference in chemical potential between the solvent and solute, dependent on mole fraction. Not shown are coefficients a_1 and b_1, as only three of the scaling coefficients in each scaling field are independent, as discussed in the previous subsection. It should be noted that all scaling coefficients and the critical parameters depend on the location of the critical locus, which can be specified by any of the four critical parameters:[73] T_{c}, P_{c}, $\mu_{1\mathrm{c}}$ and $\mu_{21\mathrm{c}}$.

These scaling equations for a dilute mixture can then be written in terms of concentration and density. Given that from thermodynamics

$$d\hat{P} = \hat{S}d\hat{T} + \hat{\rho}d\hat{\mu}_1 + \hat{\rho}xd\hat{\mu}_{21},$$

where x represents the mole fraction of solute, the expression for concentration of solute in terms of scaling fields and densities can be written as[51]

$$x = \frac{x_c + a_4\varphi_1 + b_4\varphi_2}{1 + \varphi_1 + b_2\varphi_2}. \tag{2.2.36}$$

The density and entropy density can be written as[51]

$$\hat{\rho} = \frac{1 + \varphi_1 + b_2\varphi_2}{1 - a_3\varphi_1 - b_3\varphi_2} \tag{2.2.37}$$

and

$$\hat{\rho}\hat{S} = \frac{\hat{S}_c + a_2\varphi_1 + \varphi_2}{1 - a_3\varphi_1 - b_3\varphi_2}, \tag{2.2.38}$$

respectively. It should be noted that the full expressions in both Eq. (2.2.37) and (2.2.38) are identical to those for one-component fluid.[51,68] Also, similar to a one-component fluid as discussed previously, $c_1 = 1$, $c_2 = -1$ and $c_3 = -\hat{S}_c$, while $c_4 = -x_c$.

As given by the expression for concentration in Eq. (2.2.36), asymmetry in the mixture must now be accounted for in the remaining coefficients. As we are considering the dilute solution, where a very small amount of solute added to a pure fluid or binary fluid mixture, the coefficient b_2 will be approximated to be the same as for a pure fluid and unaffected by a small addition of solute. However, the coefficients a_4 and b_4 must be calculated from properties of the mixture itself.

Using a method developed by Anisimov *et al.*,[78] a_4 and b_4 can be approximated using the derivatives of h_1 and h_2 with respect to the mixture term, μ_{21}. Along the critical line, h_1 and h_2 vanish, therefore a_4 can be determined from Eq. (2.2.33):

$$h_1 = 0 = \Delta\hat{\mu}_1 + a_2\Delta\hat{T} + a_3\Delta\hat{P} + a_4\Delta\hat{\mu}_{21}$$

$$0 = \frac{d\mu_{1\mathrm{c}}}{d\mu_{21}} + a_2\frac{dT_\mathrm{c}}{d\mu_{21}} + a_3\frac{dP_\mathrm{c}}{d\mu_{21}} + a_4\frac{d\mu_{21}}{d\mu_{21}}$$

To solve for a_4 in terms of dimensionless groups, we obtain:

$$a_4 \square -\left[\frac{d\mu_{1\mathrm{c}}}{d\mu_{21}} + a_2 k_\mathrm{B}\frac{dT_\mathrm{c}}{d\mu_{21}} + a_3\frac{1}{\rho_\mathrm{c}}\frac{dP_\mathrm{c}}{d\mu_{21}}\right] \tag{2.2.39}$$

Note that also along the critical line, $\mu_{21} = k_\mathrm{B}T_\mathrm{c}\ln x_\mathrm{c}$, therefore:

$$\frac{d\mu_{21}}{dx} = \frac{k_\mathrm{B}T_\mathrm{c}}{x_\mathrm{c}}. \tag{2.2.40}$$

The unknown temperature and pressure derivatives in Eq. (2.2.39) can then be determined as

$$\frac{dT_\mathrm{c}}{d\mu_{21}} = \frac{dT_\mathrm{c}}{dx}\frac{dx}{d\mu_{21}} = \frac{dT_\mathrm{c}}{dx}\frac{x_\mathrm{c}}{k_\mathrm{B}T_\mathrm{c}} \tag{2.2.41}$$

and

$$\frac{dP_\mathrm{c}}{d\mu_{21}} = \frac{dP_\mathrm{c}}{dx}\frac{dx}{d\mu_{21}} = \frac{dP_\mathrm{c}}{dx}\frac{x_\mathrm{c}}{k_\mathrm{B}T_\mathrm{c}}$$

$$\frac{dP_\mathrm{c}}{dx}\frac{x_\mathrm{c}}{\rho_\mathrm{c}k_\mathrm{B}T_\mathrm{c}} = x_\mathrm{c}\frac{d\hat{P}_\mathrm{c}}{dx}. \tag{2.2.42}$$

The unknown derivative $d\mu_{1\mathrm{c}} / d\mu_{21}$ can be found from the Gibbs-Duhem relation:

$$\sum N_i d\mu_i = -\underline{S}dT + \underline{V}dP$$

$$d\mu_1 = -SdT + VdP - xd\mu_{21}.$$

Therefore, at critical conditions

$$d\mu_{1\mathrm{c}} = -S_\mathrm{c}dT_\mathrm{c} + V_\mathrm{c}dP_\mathrm{c} - x_\mathrm{c}d\mu_{21} \tag{2.2.43}$$

Taking the derivative of Eq. (2.2.43) with respect to $d\mu_{21}$ the expression becomes

$$\frac{d\mu_{1\mathrm{c}}}{d\mu_{21}} = -S_\mathrm{c}\frac{dT_\mathrm{c}}{dx}\frac{dx}{d\mu_{21}} + V_\mathrm{c}\frac{dP_\mathrm{c}}{dx}\frac{dx}{d\mu_{21}} - x_\mathrm{c}. \tag{2.2.44}$$

As the reference value of entropy of the fluid is completely arbitrary (as only the value of the entropy difference is of concern), the critical value of entropy can be chosen in such a way that is simplifies the overall expression. In this case, the definition in Eq. (2.2.20) will be used, where $S_\mathrm{c} = k_\mathrm{B}\left(\partial\hat{P}/\partial\hat{T}\right)_{h_1=0,\mathrm{c}}$. Given this relation and noting that $V_\mathrm{c} = 1/\rho_\mathrm{c}$, Eq. (2.2.44) becomes

$$\frac{d\mu_{1\mathrm{c}}}{d\mu_{21}} = \frac{x_\mathrm{c}}{\rho_\mathrm{c}k_\mathrm{B}T_\mathrm{c}}\left[-\left(\frac{\partial P}{\partial T}\right)_{h_1=0,\mathrm{c}}\frac{dT_\mathrm{c}}{dx} + \frac{dP_\mathrm{c}}{dx} - \rho_\mathrm{c}k_\mathrm{B}T_\mathrm{c}\right]. \tag{2.2.45}$$

Noting that the Krichevskii parameter is defined as

$$K \equiv \frac{dP_\mathrm{c}}{dx} - \left(\frac{\partial P}{\partial T}\right)_{h_1=0,\mathrm{c}}\frac{dT_\mathrm{c}}{dx}, \tag{2.2.46}$$

Eq. (2.2.45) can be re-written as

$$\frac{d\mu_{1\mathrm{c}}}{d\mu_{21}} = \frac{x_\mathrm{c}}{\rho_\mathrm{c}k_\mathrm{B}T_\mathrm{c}}\left(K - \rho_\mathrm{c}k_\mathrm{B}T_\mathrm{c}\right). \tag{2.2.47}$$

The Krichevskii parameter represents is the difference in slope between the critical line and saturation curve and applies the physical characteristics of the mixture and its dependence on concentration of solute.

Now that the derivatives have been determined in terms of known and measurable values, the expression in Eq. (2.2.23) can be re-written with dimensions as

$$a_2 = -a_3 \frac{1}{\rho_{\mathrm{c}} k_{\mathrm{B}}} \left(\frac{\partial P}{\partial T} \right)_{h_1 = 0,\mathrm{c}} .$$

Given this expression, Eq. (2.2.39) can be simplified as

$$a_4 \cong -x_{\mathrm{c}} \left[\left(1 + a_3\right) \hat{K} - 1 \right], \tag{2.2.48}$$

noting that the dimensionless Krichevskii parameter is defined as $\hat{K} \equiv K / \rho_{\mathrm{c}} k_{\mathrm{B}} T_{\mathrm{c}}$.

Similar to the method used previously for the scaling coefficient a_4, a relationship can be established between the scaling coefficient b_4 with respect to coefficients b_1, b_2 and b_3 along the critical line, where $h_2 = 0$, using the method developed by Anisimov *et al.*,[78] this time in terms of dimensionless variables:

$$b_4 \cong -\left[k_{\mathrm{B}} \frac{dT_{\mathrm{c}}}{d\mu_{21}} + b_2 \frac{d\mu_{1\mathrm{c}}}{d\mu_{21}} + b_3 \frac{1}{\rho_{\mathrm{c}}} \frac{dP_{\mathrm{c}}}{d\mu_{21}} \right]. \tag{2.2.49}$$

Using the derivatives previously determined in Eqs. (2.2.40), (2.2.42) and (2.2.47), the expression for the scaling coefficient b_4 can be written as

$$b_4 \cong -x_{\mathrm{c}} \left[\frac{d\hat{T}_{\mathrm{c}}}{dx} + b_2 \left(\hat{K} - 1 \right) + b_3 \frac{d\hat{P}_{\mathrm{c}}}{dx} \right]. \tag{2.2.50}$$

Depending on how the effects of b_2 and b_3 are to be considered, there are two possible treatments of their approximation. As they cannot be determined independently by experiment, they can be considered in two cases: one approximation in which $b_2 = b_3$, and in the other approximation, where $b_3 = 0$. In the case of the approximation were $b_2 = b_3$, Eq. (2.2.50) becomes

$$b_4 \cong -x_\mathrm{c}\left[\frac{d\hat{T}_\mathrm{c}}{dx} + b_2\left(\hat{K} - 1 + \frac{d\hat{P}_\mathrm{c}}{dx}\right)\right] \quad (\text{for } b_1 = 1 \text{ and } b_2 = b_3). \tag{2.2.51}$$

Alternately, in the case of the approximation where $b_3 = 0$, Eq. (2.2.50) becomes

$$b_4 \cong -x_\mathrm{c}\left[\frac{d\hat{T}_\mathrm{c}}{dx} + b_2\left(\hat{K} - 1\right)\right] \quad (\text{for } b_1 = 1 \text{ and } b_3 = 0). \tag{2.2.52}$$

These expressions can now be used to model the behavior of real dilute solutions, accounting for asymmetry.

Similar to the effect of solute concentration on the scaling coefficients a_4 and b_4, the scaling coefficients a_3 and b_2 can also be impacted by concentration. Cerdeiriña *et al.*[79] and Wang and Anisimov[68] have shown that these scaling coefficients show a strong dependence on molecular volume. Therefore, when there is a large difference in molecular volume between solvent and solute, especially when a large amount of solute is present, the calculation of fluid density is affected.

Based on the findings of Wang and Anisimov,[68] a potential solution to this issue is to approximate the dependence of a_3 on the change in critical volume with a change in critical concentration of a fluid mixture as

$$a_3(x_\mathrm{c}) \cong a_3^0 + \frac{x_\mathrm{c}}{V_\mathrm{c}}\frac{dV_\mathrm{c}}{dx}, \tag{2.2.53}$$

where a_3^0 is the scaling coefficient of the pure solvent. Note that the correction factor is added to the pure component. This is because a_3 should increase if the critical density decreases when the concentration of solute is increased (i.e. dV_c / dx is positive). Conversely, an increased concentration of solute with a smaller molecular volume and larger critical density (i.e. dV_c / dx is negative) will decrease the asymmetry of the solution.

In a similar manner, we can approximate that the coefficient b_2 is also dependent on concentration as,

$$b_2(x_c) \cong b_2^0 + k \frac{x_c}{V_c} \frac{dV_c}{dx} \tag{2.2.54}$$

where b_2^0 is the scaling coefficient of the pure solvent and k is an empirical constant approximated to be $k \sim 1/3$ in this work, based upon the findings of Wang and Anisimov.[68] Since the values of b_2 tend to be much smaller in magnitude[68] relative to a_3 and due to a reduction by an empirical constant k, the coefficient b_2 may not have a significant impact on fluid asymmetry.

3.3 The Smooth Interface

Since the modeling of real fluids, which now takes into account the affect of critical fluctuations, the same should also be considered for the behavior of the smooth interface. The mean-field approximation of the smooth interface was discussed in Chapter 2; however, the effect of critical fluctuations is not considered in this method. To account for these fluctuations, and their impact on the smooth interface, the results of renormalization group theory can be applied. In general terms, renormalization group theory utilizes the Ising model, accounting for fluctuations near the critical point by including the effect of directional spin densities.[56] This theory shows that the universal expression for the density profile can be written in the form,

$$\frac{\varphi}{\varphi_0} = \Psi(z/2\xi), \tag{2.3.1}$$

similar to what was expressed in Chapter 2. Ohta and Kawasaki[80] suggested that the profile for the surface can be written as follows to more accurately fit the actual density profile for a given substance:

$$\Psi(z/2\xi) = \tanh(-z/2\xi)\left[1 + \frac{2a}{3+a}\operatorname{sech}^2(-z/2\xi)\right]^{-1/2} \tag{2.3.2}$$

where

$$a = \frac{\sqrt{3}}{6}\pi\varepsilon \qquad\qquad \varepsilon = 4 - d,$$

and d is the number of dimensions. The same coordinate system as before, where the more dense fluid lies in the $-z$ direction, is applied to Ohta and Kawasaki's result in Eq. (2.3.2). Note that when $\varepsilon = 0$ (for $d = 4$), the mean-field approximation result is obtained as in Eq. (2.2.7). A comparison of these results can be seen in Fig. 3.3, where the profile gradient is smoothed further when accounting for the effects of critical fluctuations.

The interface thickness can be approximated in terms of ξ by assessing the magnitude of the profile gradient of the renormalization group theory results shown in Fig. 3.4. This figure illustrates the dimensionless density gradient based on Eq. (2.3.2). The shading indicates where the magnitude of the gradient is the greatest, from which we can estimate the interface thickness to be $\pm\ \xi$, or 2ξ. This can be confirmed by a visual inspection of Fig 3.3, where the largest gradient of the density profile resides between ± ξ .

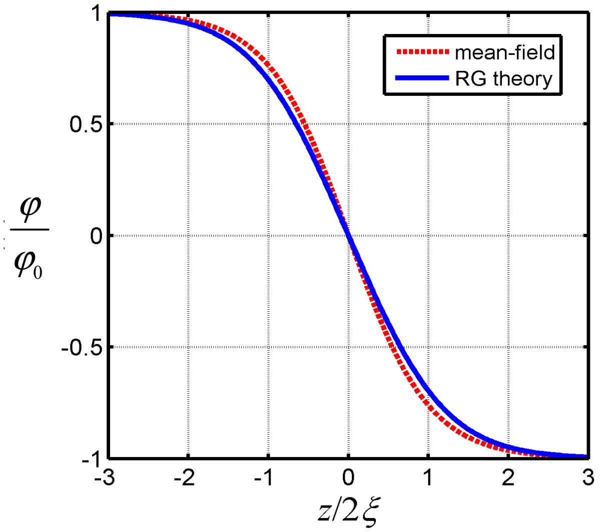

Figure 3.3. Comparison of mean-field and renormalization group theory density profiles as a function of height. The mean-field theory profile (based on Landau expansion of the local Helmholz energy density, shown in Chapter 2) in Eq. (2.2.7) is represented by the dashed red line. The results renormalization group (RG) theory[76] in Eq. (2.3.2) are represented by the solid blue line.

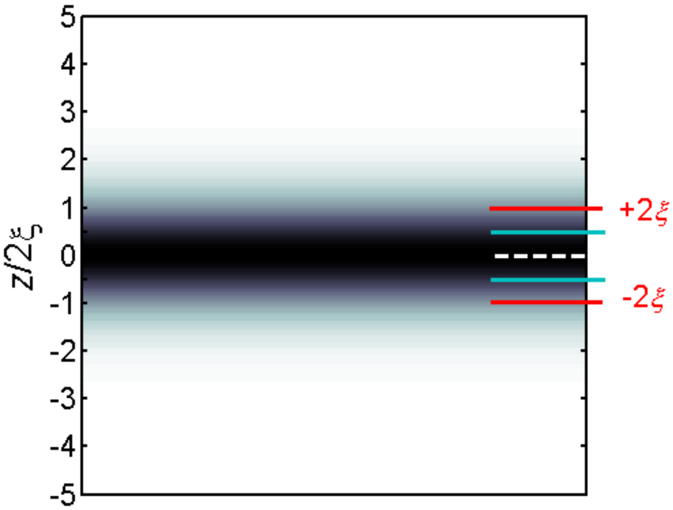

Figure 3.4. Contour plot of the interface between liquid and vapor phases as predicted by renormalization group theory.[80] The shading indicates a larger slope of the density profile. The solid blue lines bound ± ξ and the two solid red lines bound ± 2ξ .

The significance of the interfacial thickness is highlighted by the example of a sub-micron droplet of water near the vapor-liquid critical point. A simple simulation of this droplet was created using toolboxes in MATLAB developed by Adomaitis and Chen[10,11] and is shown in Fig. 3.5. Based on this simulation, the interfacial thickness $2\xi \cong 0.2R$, therefore, for a droplet 200 nm in radius, the interfacial width would be 40 nm. Taking into account Eq. (2.2.1) for the correlation length of fluctuations in density, approximating the correlation length amplitude as molecular size ($\xi_0 \cong 0.1\ \text{nm}$), and the critical temperature of water ($T_\text{c} \cong 647\ \text{K}$), this simulation represents a temperature $\sim 0.2\ \text{K}$ from the critical point of water.

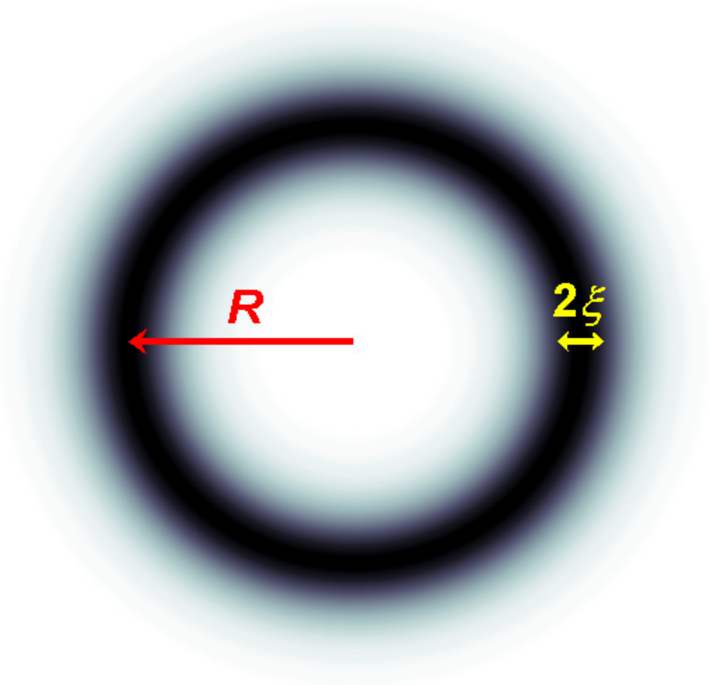

Figure 3.5. Simulation (applying toolboxes in MATLAB developed by Adomaitis and Chen[10,11]) of a smooth interface for a droplet near the critical point of fluid-fluid separation using RG theory.[76] The intensity of shadowing represents the square of the density/concentration profile in Eq. (2.3.2) The "thickness" of the interface, given by a characteristic decay-length scale of the profile, is indicated by 2ξ.

It should be noted that since the thickness of the smooth interface is mesoscopic in scale and can extend from nanometers to microns, the droplet size cannot be defined smaller than this characteristic thickness, as there would be no distinction between the behaviors of the bulk phases. This thickness is dependent on the properties of the fluid, but in the case of the symmetric interface given in Figures 3.3 and 3.4, the properties of the bulk phases are not apparent until $\pm 6\xi$.

3.4 Estimations of Surface Tension

Similar to the calculation of surface tension for the mean-field approximation given in Chapter 2, definitions of correlation length and amplitudes will be employed. However, in these calculations, the effects of critical fluctuations will be accounted for. The methodologies discussed will include the results from renormalization group theory, a local approximation of the slope of the renormalization group theory profile and dimensional scaling analysis.

3.4.1 Renormalization Group Theory Results

Not only does renormalization group theory provide the results for an interfacial profile, but this theory can also assist in the estimation of surface tension. This simple calculation can be made by using two definitions from this theory. The surface energy of an area of interaction, obtained from the Ising lattice model and renormalization group theory has been determined by Zinn,[81]

$$\frac{\sigma_0 \left(\xi_0^+\right)^2}{k_\mathrm{B} T_\mathrm{c}} \cong 0.377 \tag{2.4.1}$$

where the $+$ sign indicates the value above the critical point. This equation can be divided by the two-scale universality factor,[48,70]

$$A_0^+ \rho_\mathrm{c} \left(\xi_0^+\right)^3 \cong 0.171, \tag{2.4.2}$$

which yields the following expression for the coefficient of surface tension, based on the renormalization group theory, for amplitudes above the critical point:

$$\frac{\sigma_0}{\rho_c k_B T_c A_0^+ \xi_0^+} \cong 2.20\,. \tag{2.4.3}$$

Similarly, we can calculate the surface tension above the critical point by using the ratio of correlation lengths above and below the critical point,[82]

$$\frac{\xi_0^+}{\xi_0^-} \cong 1.96\,, \tag{2.4.4}$$

and the ratio of the critical value of the heat capacity above and below the critical point,[70]

$$\frac{A_0^+}{A_0^-} \cong 0.523\,, \tag{2.4.5}$$

where ± indicates the value above and below the critical point, respectively. Applying the ratios in Eqs. (2.4.4) and (2.4.5) to Eq. (2.4.3), the coefficient of surface tension for amplitudes below the critical point is

$$\frac{\sigma_0}{\rho_c k_B T_c A_0^- \xi_0^-} \cong 2.26\,. \tag{2.4.6}$$

3.4.2 Dimensional Scaling Analysis

We can also develop a more general result for the surface tension using dimensional scaling by estimating the surface tension as the product of the density of the Helmholtz-energy density and the width of the vapor-liquid interface. Because we are only considering the behavior below the critical point along the coexistence curve, we only need to consider only one variable—in this case, temperature—as density along the coexistence curve is a function of temperature. The Helmholtz energy per unit volume scales as[8]

$$\frac{\Delta A}{V} \propto \frac{A_0^-}{(2-\alpha)(1-\alpha)} \left|\Delta\hat{T}\right|^{2-\alpha}. \qquad (2.4.7)$$

Therefore taking into account this relation, the expression for the correlation length in Eq. (2.2.1) and assuming the interface thickness is 2ξ as before, the expression for the dimensionless surface tension can be approximated as

$$\frac{\sigma}{\rho_c k_B T_c} \propto \frac{\Delta A}{V} 2\xi = \frac{2A_0^-}{(2-\alpha)(1-\alpha)} \xi_0^- \left|\Delta\hat{T}\right|^{2-\alpha-\nu}. \qquad (2.4.8)$$

Noting that the universal exponents

$$2-\alpha-\nu = (d-1)\nu = \vartheta. \qquad (2.4.9)$$

Therefore, the relation in Eq. (2.4.8) can be written in terms of the general exponent in Eq. (2.4.9):

$$\frac{\sigma}{\rho_c k_B T_c} \propto \frac{2A_0^-}{(2-\alpha)(1-\alpha)} \xi_0^- \left|\Delta\hat{T}\right|^{\vartheta}. \qquad (2.4.10)$$

Note that van der Waals theory,[8,54,56] which neglects critical fluctuations, predicts an exponent of $\vartheta = 3/2$.

The expression for the dimensionless surface tension coefficient is

$$\frac{\sigma_0}{\rho_c k_B T_c A_0^- \xi_0^-} \cong 1.19, \qquad (2.4.11)$$

where in the case of $d = 3$,

$$\sigma = \sigma_0 \left|\Delta\hat{T}\right|^{2\nu}. \qquad (2.4.12)$$

Above the critical point, taking into account Eqs. (2.4.4) and (2.4.5), this expression for the surface tension coefficient becomes

$$\frac{\sigma_0}{\rho_c k_B T_c A_0^+ \xi_0^+} \cong 1.16 \tag{2.4.13}$$

If the surface tension is calculated for an interface thickness of $\pm 2\xi$, or 4ξ, these coefficients would be

$$\frac{\sigma_0}{\rho_c k_B T_c A_0^- \xi_0^-} \cong 2.37 \tag{2.4.14}$$

and

$$\frac{\sigma_0}{\rho_c k_B T_c A_0^+ \xi_0^+} \cong 2.32 \tag{2.4.15}$$

for values below and above the critical point, respectively.

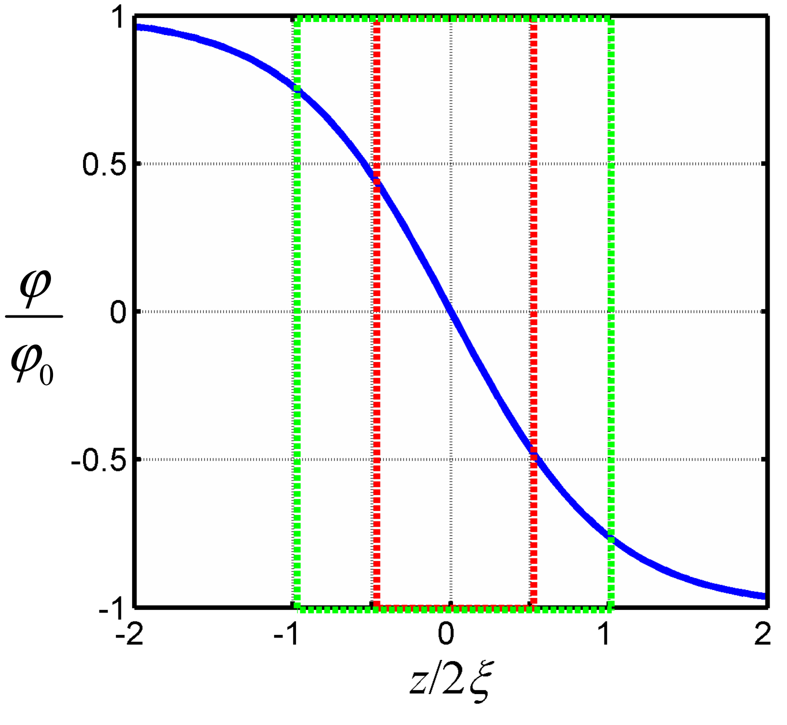

Figure 3.6. Representation of the interface thickness considered for the dimensional scaling analysis calculation of surface tension in Eqs. (2.4.11) and (2.4.13)-(2.4.15). The profile plotted is the result from RG theory in Eq. (2.3.2). The red box highlights the portion of the density profile used to calculate the surface tension in the dimensional scaling analysis between $\pm\xi$. The green box highlights the portion of the density profile between $\pm 2\xi$.

A graphical representation of the estimation of the interfacial thickness for the calculations in Eqs. (2.4.11) and (2.4.13)-(2.4.15) can be seen in Fig. 3.6. Note that a large portion of the profile slope is neglected by the small box, whereas the large box is more inclusive of the behavior of the gradient.

Table 3.1. Comparison of mean-field and scaling methods for the estimation of surface tension coefficients.

Method	Coefficients for Amplitudes below the Critical Point	Equation
Mean-field Approximation	$\frac{\sigma_0}{\rho_c k_B T_c \bar{C}_V \bar{\xi}_0^-} = \frac{8}{3}$	(2.5.9)
Renormalization Group Theory	$\frac{\sigma_0}{\rho_c k_B T_c A_0^- \xi_0^-} \cong 2.26$	(2.4.6)
Dimensional Scaling Analysis (2ξ)	$\frac{\sigma_0}{\rho_c k_B T_c A_0^- \xi_0^-} \cong 1.19$	(2.4.11)
Dimensional Scaling Analysis (4ξ)	$\frac{\sigma_0}{\rho_c k_B T_c A_0^- \xi_0^-} \cong 2.37$	(2.4.14)
Experimental Results[a]	$\frac{\sigma_0}{\rho_c k_B T_c A_0^- \xi_0^-} \cong 2.15 - 2.89$	N/A

[a] Reference 83

3.4.3 Comparison of Methodologies

This section and Section 2.5 both address methods to approximate the surface tension at an interface. A summary of these approximations is compared to experimental results in Table 3.1. Note that the result of renormalization group theory is well within the experimental range of values for the amplitude coefficients. The dimensional scaling analysis with the large interface thickness (4ξ) also provides an estimate close to experimental values as compared to the mean-field approximation and the results of the dimensional analysis with the small interface thickness (2ξ). These results highlight both the need to take into account the effects of critical fluctuations as well as a careful choice of the interfacial width.

Chapter 4: Curved Interfaces and Surface Tension

As discussed previously, surface tension is crucial for many engineering applications including droplet formation, microemulsions, nucleation, flow through micropores and capillary action. Usually, the effects of curvature are ignored as they are considered negligible on the macroscale. However, as processes are scaled down to consider small droplets, such as aerosol production or modeling of biological cells, surface curvature can play a more significant role on the calculation of surface tension.

4.1 Tolman's Length: Curvature Correction to the Surface Tension

4.1.1 Young-Laplace Approximation of Surface Tension

A well-known starting point for the calculation for the surface tension is the Young-Laplace equation,[84]

$$P_\alpha - P_\beta = \sigma_\infty \left(\frac{1}{R_1} + \frac{1}{R_2} \right). \qquad (4.1.1)$$

Here, P_α and P_β represent the pressures of the phases on the concave side (or inside) and outside, respectively, and the radii R_1 and R_2 represent the radii of curvature. The surface tension, σ_∞, is considered to be that of an infinite plane without curvature.

The Young-Laplace equation can be simplified for spherical bubbles and droplets when all radii of curvature are equivalent ($R = R_1 = R_2$), therefore

$$P_\alpha - P_\beta = \frac{2\sigma_\infty}{R}. \tag{4.1.2}$$

As before, the pressures P_α and P_β represent the pressures of the phases on the inside and outside, respectively, of the bubble or droplet. This is illustrated in Fig. 4.1.

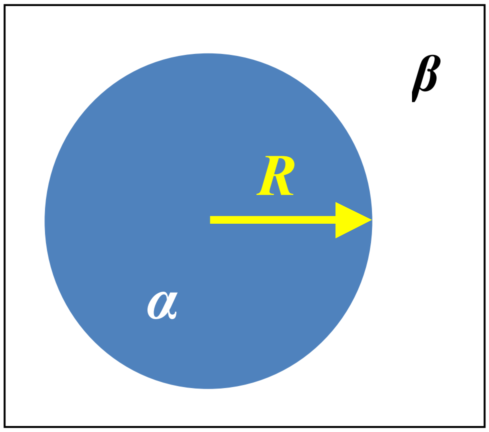

Figure 4.1. Simple schematic illustrating the properties of the variables used in the Young-Laplace relation for surface tension at the interface between two phases, α and β.

4.1.2 Expression for Tolman's Length

It is commonly believed that the effect of curvature on surface tension is negligible for calculations on the macroscale, therefore the surface tension of an infinite plane can be used for calculations on this scale as seen in Eq. (4.1.1). Some have refuted the claim that there is any effect of curvature on the surface tension;[81-83] however, many believe that for very small droplets and bubbles the surface tension is affected by strong curvature.[2,16,20-23,26,27,44,88,89]

In 1949, Tolman[2] considered the effect of droplet size on the calculation of the surface of tension as previously described by Young and Laplace and determined there should be a correction parameter. This parameter, known as 'Tolman's length'

(δ), represents the difference in radius between the equimolar surface (R_e) and surface of tension (R) in a droplet of liquid,[2,16,19,56]

$$\delta = R_\mathrm{e} - R, \tag{4.1.3}$$

and can be applied to the expansion of the planar surface tension as[2]

$$\sigma(R) = \sigma_\infty\left(1 - \frac{2\delta}{R} + \ldots\right). \tag{4.1.4}$$

This is commonly known as the Laplace-Tolman equation. Note that Eq. (4.1.3) establishes the sign of the Tolman length as negative for droplets and positive for bubbles, which has been verified by other studies.[89] An illustration of this concept for a droplet of liquid can be seen in Fig. 4.2. As it can be seen from Eq. (4.1.4), the smaller the radius R, the more significant Tolman's length becomes.

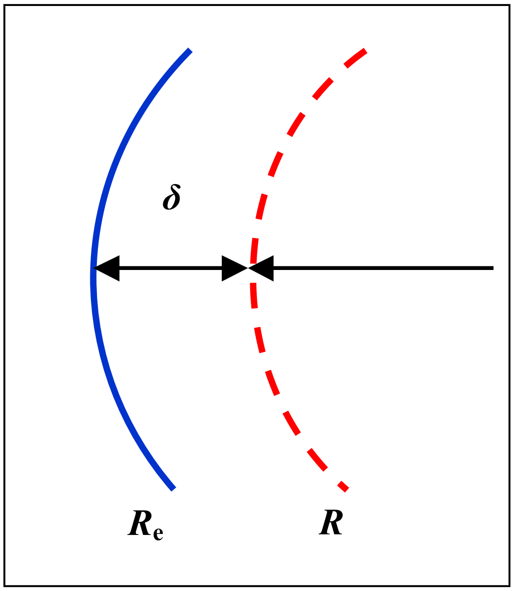

Figure 4.2. Sketch of the concept of the Tolman length (δ) for a droplet of liquid, where R is the radius of the surface of tension and R_e is the radius of the equimolar surface.

A more general equation for the surface tension was developed later by Helfrich,[89] which includes a second-order correction due to curvature in the expansion of surface tension,

$$\sigma(R) = \sigma_\infty \left(1 - \frac{2\delta}{R} + \frac{k}{R^2} \ldots\right), \tag{4.1.5}$$

where k is a constant that accounts for the rigidity of the interface. However, this equation is not widely accepted as studies indicate that higher order terms will not likely provide a more accurate result.[37] Therefore, the focus of this study will be on the Laplace-Tolman expression in Eq. (4.1.4).

4.1.3 Predictions of the Behavior of Tolman's Length

Studies of the Tolman length have yielded various results. For sharp interfaces (as mentioned in Chapter 2), where the vapor-liquid or liquid-liquid interface thickness is on the order of the size of a molecule, Tolman's length is expected to be very small. This is one of the reasons that a significant curvature-correction has only been believed to affect nano-sized droplets.

The sign of Tolman's correction to the surface tension has been a subject of debate as well. Some studies have confirmed that the Tolman's length is negative for droplets,[16,22,26,29,31] while molecular dynamics simulations have indicated that it may be positive.[23,90,91] Other studies have found that the sign of Tolman's length cannot be de determined with much certainty,[20] while Lei *et al.*[40] and Guermer *et al.*[34] cite that the sign is only negative for droplets that are not close to molecular size and, in the case of very small droplets, the surface tension actually vanishes.

There are also varying conclusions regarding the behavior of the Tolman's length for a smooth interface near the critical point. Square gradient theories have provided results consistent with mean-field theory,[43,44] as discussed in Chapter 2. It should also be noted that symmetric systems, such as the lattice-gas and regular solution models, do not exhibit an effect on Tolman's length, partially as a result of the values of the mean-field critical exponents. Gránásy[26] and Moody and Attard[29] predicted that the Tolman length would become increasingly negative when approaching the critical temperature. Moody and Attard[29] also indicate that the Tolman length may even change sign very close to or at the critical temperature. These findings further support the ambiguity of the Tolman length behavior near the critical point due to the effect of critical fluctuations.[43]

Studies that acknowledge the existence of Tolman's length have given many different results: Tolman's length is finite, logarithmically divergent, or algebraically divergent with varying exponents. Phillips and Mohanty[92] suggested that the Tolman length diverges with the same exponent as the correlation length of critical fluctuations $\left(-\nu \cong -0.630\right)$, while others made different predictions. Fisher and Wortis[93] predicted two terms: one weakly diverging term with an exponent of -0.065 and the other, more strongly diverging term with an exponent of -0.130. Using the 'penetrable-sphere model' developed by Widom and Rowlinson,[94] and Rowlinson[19,35] determined that the exponent for the Tolman length showed a weak divergence $\left(-0.065\right)$. These results are commonly accepted, as they are supported by an exact result using scaling obtained by Fisher and Wortis.[93]

There have been more recent developments in scaling that more properly account for fluid asymmetry. Fisher and Orkoulas[49] recognized the correction needed to model this behavior and developed an approach known as "complete" scaling, which was elaborated by Kim *et al.*[50] Anisimov and Wang verified this approach and further developed it for convenient use in practical applications,[68,95] and others have applied these results to binary fluids.[79] Anisimov[45] recently indicated that a complete scaling approach to calculating the near-critical Tolman length yields a much stronger algebraic divergence than shown in previous works, with an exponent of $\beta - \nu \cong -0.304$. This effect is the result of critical fluctuations and its amplitude is a function of fluid asymmetry; therefore this behavior does not exist in the mean-field regime. This result showing a strongly divergent behavior indicates that the magnitude of the Tolman length may result in a significant curvature correction calculation in highly asymmetric fluids and fluid mixtures.

4.2 Tolman's Length Near the Critical Point

As fluid asymmetry, in addition to curvature, impacts the Tolman's length[19,43,93] the method of complete scaling can be used to account for both fluid asymmetry and critical fluctuations as discussed in Chapter 3. For a general derivation of the Tolman length using scaling theory, Anisimov[45] related the pressure difference in the Laplace-Tolman equation to the susceptibility with respect to fluctuations in density.

The pressure difference between the inside of a droplet of liquid and its surrounding vapor is derived from two parts: a symmetric part—which is independent of specific fluid characteristics—and an asymmetric part, which is specific to the fluid,

$$P_\alpha - P_\beta = \left(P_\alpha - P_\beta\right)_{\text{sym}} + \left(P_\alpha - P_\beta\right)_{\text{asym}} . \tag{4.2.1}$$

As the Laplace-Tolman equation (Eq. (4.1.5)) accounts for both curvature and asymmetry in the Tolman length, δ, this expression can be used to estimate the total pressure difference as

$$\left(P_\alpha - P_\beta\right)_{\text{sym}} + \left(P_\alpha - P_\beta\right)_{\text{asym}} \cong \frac{2\sigma_\infty}{R}\left(1 - \frac{2\delta}{R}\right). \tag{4.2.2}$$

Since the Tolman length is attributed to asymmetry,[45] we can assume that symmetric contribution to this pressure difference is related to the planar surface tension described in Eq. (4.1.2)

$$\left(P_\alpha - P_\beta\right)_{\text{sym}} = \frac{2\sigma_\infty}{R} . \tag{4.2.3}$$

Therefore, combining this equation with Eq. (4.2.2), the ratio of Tolman's length with respect to the radius of surface tension becomes[45]

$$\frac{2\delta}{R} \cong -\frac{\left(P_\alpha - P_\beta\right)_{\text{asym}}}{\left(P_\alpha - P_\beta\right)_{\text{sym}}} . \tag{4.2.4}$$

Anisimov[45] suggested that this same pressure difference can be approximated using the 'critical part' of the grand-canonical potential per unit volume ($\Omega / V = -P$) as ΔP_{cr}, multiplied by the correlation length, as ΔP_{cr} is related to the surface tension. Since R is the length scale in Laplace's pressure difference equation, the correlation length, ξ, is the corresponding length scale for the pressure difference ΔP_{cr}. Following the scaling approximation,

$$\left(P_\alpha - P_\beta\right)_{\text{sym}} R \sim \left(\Delta P_{\text{cr}}\right)_{\text{sym}} \xi$$

and

$$\left(P_\alpha - P_\beta\right)_{\text{asym}} R^2 \sim \left(\Delta P_{\text{cr}}\right)_{\text{asym}} \xi^2 .$$

Therefore, Anisimov's[45] result is obtained for Eq. (4.2.4) as

$$\frac{2\delta}{\xi} \cong -c_\delta \frac{\left(\Delta P_{\text{cr}}\right)_{\text{asym}}}{\left(\Delta P_{\text{cr}}\right)_{\text{sym}}} \tag{4.2.5}$$

where c_δ is a universal constant, estimated as □ $0.6-0.7$ from scaling theory.

Close to the critical point, ΔP_{cr} can be approximated as[45]

$$\Delta P_{\text{cr}} \approx \chi \left(\Delta\mu\right)^2 , \tag{4.2.6}$$

where the total susceptibility with respect to density fluctuations is defined as

$$\chi = \left(\frac{\partial\rho}{\partial\mu}\right)_T = \left(\frac{\partial^2 P}{\partial\mu^2}\right)_T . \tag{4.2.7}$$

Just as with the pressure differences, the total susceptibility can be written in terms of a symmetric and asymmetric part, analogous to the pressure in Eq. (4.2.2) and the critical part of the grand-canonical potential in Eq. (4.2.5) so that

$$\chi = \chi_{\text{sym}} + \chi_{\text{asym}} . \tag{4.2.8}$$

Therefore Eq. (4.2.5) for the Tolman length-correlation length ratio can be re-written in terms of the susceptibility in Eq. (4.2.6) as

$$\frac{2\delta}{\xi} \cong -c_\delta \frac{\chi_{\text{asym}}}{\chi_{\text{sym}}} . \tag{4.2.9}$$

In order to use complete scaling as discussed in Chapter 3, Eq. (4.2.9) must be re-written in terms of scaling variables. The total susceptibility in Eq. (4.2.8) is also a combination of the strong, weak and cross scaling susceptibilities in Eqs. (2.2.11)-(2.2.13). Based on the results developed by Kim[96] and Kim *et al.*[50] for complete scaling, keeping only the lower order terms (φ_1, φ_2 and φ_1^2) and eliminating any product terms (e.g. $\varphi_1\varphi_2$), the following result for the dimensionless total susceptibility can be obtained:

$$\hat{\chi} \cong \left[(1+a_3)^2(1+3a_3\varphi_1)-5b_3\varphi_2\right]\chi_1+(b_2+b_3)^2\chi_2+2(1+a_3)(b_2+b_3)\chi_{12}. \quad (4.2.10)$$

To further simplify this equation, the strength of the divergence of each term will be compared, and only the most dominant terms will be kept. In the case of the one-component fluid, in the first ε-approximation where $\gamma = 2\nu \cong 1.26$, the temperature diverges as

$$\begin{aligned} \varphi_1\chi_1 &\sim \Delta T^{\beta-\gamma} \sim \Delta T^{-0.913} \\ \varphi_2\chi_1 &\sim \Delta T^{1-\alpha-\gamma} \sim \Delta T^{-0.348} \\ \chi_2 &\sim \Delta T^{-\alpha} \sim \Delta T^{-0.109} \\ \chi_{12} &\sim \Delta T^{\beta-1} \sim \Delta T^{-0.674}. \end{aligned} \quad (4.2.11)$$

Given these results, the total susceptibility in Eq. (4.2.10) can be simplified to

$$\hat{\chi} \cong (1+a_3)^2(1+3a_3\varphi_1)\chi_1+2(1+a_3)(b_2+b_3)\chi_{12}. \quad (4.2.12)$$

By applying the results of scaling for a one-component fluid in zero ordering field ($h_1 = 0$) where

$$h_2 = \Delta\hat{T}\left(1-b_3\frac{a_2}{a_3}\right) \cong \Delta\hat{T}, \quad (4.2.13)$$

the order parameter and strong and cross scaling susceptibilities given in Chapter 3 in Eqs. (2.2.9), (2.2.11) and (2.2.13) can be approximated as

$$\begin{aligned}\varphi_1 &\approx \hat{B}_0 \left|\Delta T\right|^{\beta} \\ \chi_1 &\approx \hat{\Gamma}_0^{\pm} \left|\Delta T\right|^{-\gamma} \\ \chi_{12} &\approx \beta \hat{B}_0 \left|\Delta T\right|^{\beta-1}.\end{aligned} \tag{4.2.14}$$

Substituting these relations in Eq. (4.2.14) into the expression for the total susceptibility in Eq. (4.2.12) results in

$$\hat{\chi} \cong (1+a_3)^2 (1+3a_3\hat{B}_0 \left|\Delta T\right|^{\beta})\hat{\Gamma}_0^{\pm} \left|\Delta T\right|^{-\gamma} + 2(1+a_3)(b_2+b_3)\beta\hat{B}_0 \left|\Delta T\right|^{\beta-1}. \tag{4.2.15}$$

In terms of the approximation where $b_3 = 0$, Wang and Anisimov[64] determined the amplitudes $\hat{B}_0$ and $\hat{\Gamma}_0^{\pm}$ to be

$$\begin{aligned}\hat{B}_0 &= \frac{B_0}{1+a_3} \\ \hat{\Gamma}_0^{\pm} &= \frac{\Gamma_0^{\pm}}{\left(1+a_3\right)^2}.\end{aligned} \tag{4.2.16}$$

This provides the result for the total susceptibility in terms of variables with dimensions:

$$\hat{\chi} \cong \left[\hat{\Gamma}_0^{\pm} \left|\Delta T\right|^{-\gamma} \left(1 + \frac{3a_3}{1+a_3}\hat{B}_0 \left|\Delta T\right|^{\beta}\right)\right] - 2b_2\beta\hat{B}_0 \left|\Delta T\right|^{\beta-1}. \tag{4.2.17}$$

where the symmetric and asymmetric parts were determined to be[45]

$$\begin{aligned}\hat{\chi}_{\text{sym}} &\cong \hat{\Gamma}_0^{\pm} \left|\Delta T\right|^{-\gamma} \\ \hat{\chi}_{\text{asym}} &\cong \hat{\Gamma}_0^{\pm} \frac{3a_3}{1+a_3}\hat{B}_0 \left|\Delta T\right|^{\beta-\gamma} - 2b_2\beta\hat{B}_0 \left|\Delta T\right|^{\beta-1}.\end{aligned} \tag{4.2.18}$$

Substituting these results into the expression for the Tolman length-correlation length ratio in Eq. (4.2.9) yields the new expression

$$\frac{2\delta}{\xi} \cong -c_{\delta}\left[\frac{3a_3}{1+a_3}\hat{B}_0\left|\Delta T\right|^{\beta} - 2b_2\frac{\beta\hat{B}_0}{\hat{\Gamma}_0^{\pm}}\left|\Delta T\right|^{\beta-1+\gamma}\right]. \tag{4.2.19}$$

Applying the expression for the correlation length in Eq. (2.2.1), the expression for the Tolman length becomes[45]

$$\delta \cong \mp c_{\delta}\xi_0^{-}\left[\frac{3}{2}a_{\text{eff}}\hat{B}_0\left|\Delta T\right|^{\beta-\nu} - b_2\frac{\beta\hat{B}_0}{\hat{\Gamma}_0^{\pm}}\left|\Delta T\right|^{1-\alpha-\beta-\nu}\right], \tag{4.2.20}$$

where the prefactor $\mp$ refers to a bubble of vapor or a drop of liquid, respectively and

$$a_{\text{eff}} \equiv \frac{a_3}{1+a_3}. \tag{4.2.21}$$

This expression indicates that there are two contributions to the Tolman length near the critical point: one that weakly diverges as $\left|\Delta\hat{T}\right|^{1-\alpha-\beta-\nu} = \left|\Delta\hat{T}\right|^{-0.065}$ (as shown by others[19,35,94]) and a new term from complete scaling that diverges more strongly, as $\left|\Delta\hat{T}\right|^{\beta-\nu} = \left|\Delta\hat{T}\right|^{-0.304}$.

4.3 General Thermodynamic Expression for Tolman's Length

Anisimov[45] and Wang *et al.*[51] also suggested a general thermodynamic expression for the behavior of the Tolman length both near and far beyond the critical region. Based on fluid asymmetry, the Tolman length with respect to the thickness of the interface is suggested to be[45,51]

$$\frac{\delta}{2\xi} \cong \mp\frac{\Delta\hat{\rho}_{\text{d}}}{\hat{\rho}'' - \hat{\rho}'}, \tag{4.3.1}$$

where $\hat{\rho}''$ and $\hat{\rho}'$ are the densities in the liquid and vapor phases, respectively. In this expression, the prefactor $\mp$ refers to a droplet of liquid and bubble of vapor, respectively based on the definitions of coexisting phases. The 'diameter' of phase coexistence is represented by

$$\hat{\rho}_{\mathrm{d}} = \frac{\rho'' - \rho'}{2\rho_{\mathrm{c}}} \tag{4.3.2}$$

where ρ'' and ρ' represent the liquid and vapor branches, respectively. A simple schematic of this concept can be seen in Fig 4.3.

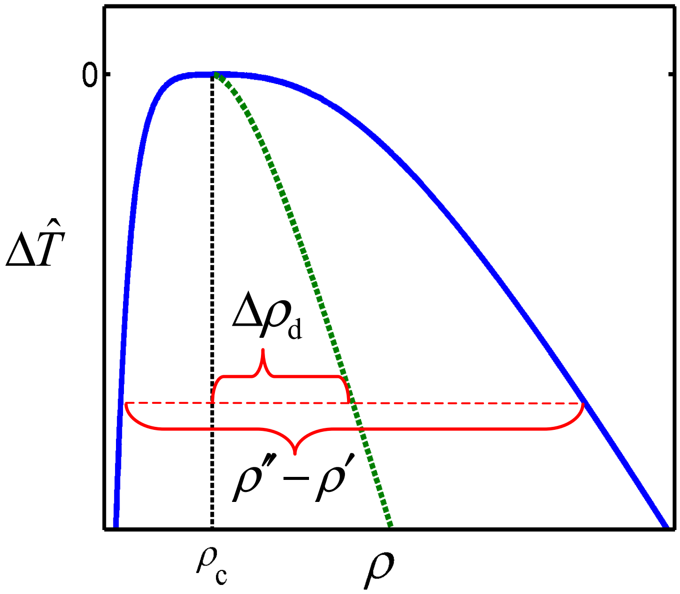

Figure 4.3. Sketch of the concept of using the coexistence diameter to approximate the ratio of the Tolman length to the interface thickness in Eq. (4.3.1). The green line represents the actual diameter, the black dotted line is the critical density and the blue line is the coexistence curve.

Equation (4.3.1) can also be verified in the critical regime using the leading and dominant term from Wang and Anisimov's[68] expression for the coexistence diameter

$$\Delta\hat{\rho}_{\mathrm{d}} = \hat{\rho}_{\mathrm{d}} - 1 \cong a_{\mathrm{eff}} \hat{B}_0^2 \left|\Delta\hat{T}\right|^{2\beta} \tag{4.3.3}$$

and the definition given by Wang and Anisimov[68] for the difference in density along the two sides of the phase boundary

$$\frac{\rho'' - \rho'}{2\rho_c} \cong \hat{B}_0 \left|\Delta\hat{T}\right|^{\beta}. \tag{4.3.4}$$

Substituting Eqs. (4.3.3) and (4.3.4) into Eq. (4.3.1) and approximating $c_\delta \cong 2/3$ yields the leading term in Eq. (4.2.19). Additionally, Eq. (4.3.1) has also been verified for use in the mean-field regime for a van der Waals fluid.[45] Since these relations have shown to be universal, they will be applied to asymmetric solutions in following chapters.

Chapter 5: Tolman's Length for Polymer Solutions and Other Dilute Binary Mixtures

5.1 Polymer Solutions: Theory and Background

Semidilute polymer solutions tend to become highly asymmetric as the degree of polymerization—or number or monomer units interconnected—increases. This is because as the length of a polymer chain increases, the polymer has less preference for the solvent, and therefore solubility decreases.

5.1.1 Phase Coexistence

There are two distinct regimes in polymer solutions: the "critical" regime and the "polymer" regime. The characteristic variable, w, first introduced by Widom,[97] separates these two regimes and is defined as:

$$w \equiv \frac{1}{2} N^{1/2} \left| \Delta \hat{T} \right|, \tag{5.1.1}$$

where N is the degree of polymerization of a polymer chain. Widom's variable provides an indication of where a particular polymer solution lies on a phase diagram. When $w << 1$, it indicates a near-critical polymer solution, when the degree of polymerization is small and the distance to the distance to the critical temperature is also very small; this is termed the "critical" regime. Conversely, when $w >> 1$ (and $N \to \infty$), it is only dependent on the degree of polymerization and is termed the "polymer" regime.

The overall behavior of polymer solutions in general can be visualized by a simple phase diagram. This behavior will be modeled in terms of known limiting behaviors and established relations in both the polymer and critical regimes.

Based on Flory theory, Povodyrev *et al.*[98] indicated that at lower volume fractions of polymer, the relation between temperature and volume fraction becomes linear, and the polymer regime in the limiting phase behavior approaches

$$\frac{T}{\theta} = -\frac{2}{3}\phi + 1, \tag{5.1.2}$$

where ϕ is the volume fraction of polymer in solution and T is the solution temperature. The theta temperature, θ, is the critical temperature of phase separation for an infinitely dilute polymer solution with an infinitely long polymer chain. This temperature is specific to the properties of a specific polymer and solvent combination. In terms of our temperature distance variable, $\Delta\hat{T}$, Eq. (5.1.2) can be re-written for the volume fraction of the solution:

$$\phi = -\frac{3}{2}\left[\Delta\hat{T}\frac{T_{\mathrm{c}}}{\theta} - 1 + \frac{T_{\mathrm{c}}}{\theta}\right]. \tag{5.1.3}$$

This equation can be written in a more general form, since the expression T_{c}/θ can be found in terms of the degree of polymerization from Flory[99] theory as

$$\frac{T_{\mathrm{c}}}{\theta} = \frac{1}{\left(1 + 1/\sqrt{N}\right)^2}. \tag{5.1.4}$$

Here, it can be seen that in the limiting case as the degree of polymerization increases ($N \to \infty$), $T_{\mathrm{c}} \to \theta$.

In the critical regime, analogous to the difference in density along the two sides of the phase boundary, Eq. (4.3.4) can be re-written in terms of volume fraction as

$$\frac{\phi'' - \phi'}{2\phi_\mathrm{c}} \cong \hat{B}_0 \left|\Delta \hat{T}\right|^{\beta} \tag{5.1.5}$$

where ϕ'' is the polymer-rich phase and ϕ' is the solvent-rich phase. This result is similar to that presented by Widom[97] and the experimental results presented by Dobashi *et al.*[100] The amplitude $\hat{B}_0$ can be determined for polymer solutions of moderate to high degrees of polymerization, accounting for the results of Anisimov *et al.*[101] such that:

$$\hat{B}_0 \cong B_{0,N=1} N^{\beta/2}, \tag{5.1.6}$$

where $\hat{B}_{0,N=1} \cong 1$ is determined from the three-dimensional Ising model, which takes into account critical fluctuations.[50] The development and *N*-dependence of the critical amplitude in Eq. (5.1.6) will be discussed in greater detail in Section 5.2. Then, in terms of the Widom variable, w, Eq. (5.1.5) becomes:

$$\frac{\phi'' - \phi'}{2\phi_\mathrm{c}} \cong (2w)^{\beta}. \qquad \text{(critical regime)} \tag{5.1.7}$$

In the polymer regime, based on the results from Anisimov *et al.*,[51] the two sides of the phase boundary can be approximated as:

$$\frac{\phi'' - \phi'}{2\phi_\mathrm{c}} \approx \frac{\phi''}{2\phi_\mathrm{c}} \approx \frac{3}{2} w. \qquad \text{(polymer regime)} \tag{5.1.8}$$

Combining what is known for both the critical and polymer regimes in Eqs. (5.1.7) and (5.1.8), respectively, a simple crossover expression can be developed to model the behavior in both regimes as well as approximate the behavior in between. This simple crossover expression for the phase boundary is then

$$\left(\frac{\phi''-\phi'}{2\phi_{\mathrm{c}}}\right)_{\times} \cong \frac{(2w)^{\beta}\left(1+\frac{3}{2}w\right)}{(1+2w)^{\beta}}. \qquad \text{(crossover)} \qquad (5.1.9)$$

Lastly, based on the works of Widom[97] and Anisimov *et al.*,[101] the solvent-rich branches in the critical and polymer regimes are given by:

$$\phi' \cong \begin{cases} \phi_{\mathrm{c}}-(6w/N)^{1/2} & (w\to 0) \\ \phi_{\mathrm{c}}-1/\sqrt{N} & (w\to\infty) \end{cases}. \qquad (5.1.10)$$

Therefore, a simple crossover expression can be developed to connect the polymer and critical regimes for the solvent-rich phase:

$$\phi'_{\times} \cong \phi_{\mathrm{c}} - \frac{\sqrt{6w}}{\sqrt{N}\left(1+\sqrt{6w}\right)}. \qquad \text{(crossover)} \qquad (5.1.11)$$

The general behavior of a polymer solution with respect to temperature distance to the critical point and the volume fraction of polymer (ϕ) from Eqs. (5.1.3), (5.1.9) and (5.1.11) is presented in Fig. 5.1. In this figure, the phase separation curve is represented by the solid blue line and the arithmetic mean of phase coexistence (or diameter, ϕ_{d}) is represented by the dotted green line. Similar to the coexistence curve for an asymmetric fluid shown in Fig. 4.4 in Chapter 4, asymmetry is evident from the slope of the diameter. The red line represents the phase-limiting behavior at an infinite degree of polymerization ($N\to\infty$), which terminates at the theta temperature, θ, as predicted by Flory theory.[99]

Also, similar to the fluids described previously the same curved diameter is observed near the critical point, seen in the inset in Fig. 5.1. As before, this curvature is a result of fluctuations as the critical point is approached.

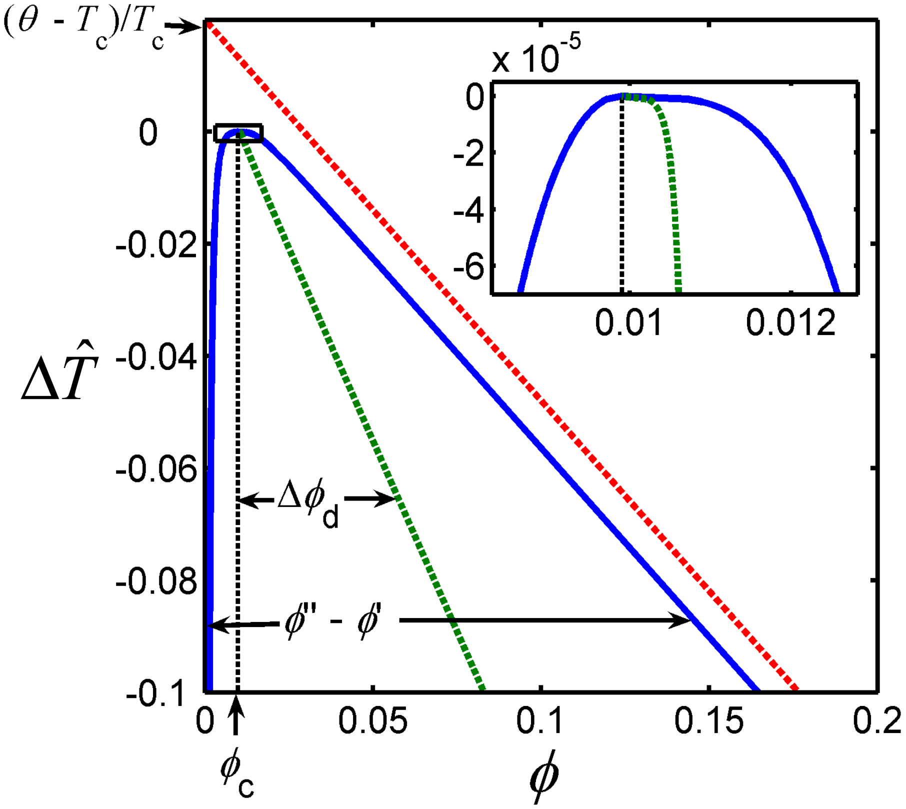

Figure 5.1. Phase diagram for a polymer solution ($N = 10^4$) near the critical point. The solid blue line represents the phase separation curve. The dotted red line represents the phase-limiting behavior at an infinite degree of polymerization, which originates at the theta point (or theta temperature) as predicted by Flory theory.[99] The coexistence diameter (ϕ_d) is illustrated by the green dotted line. ϕ'' and ϕ' represent the volume fractions of polymer-rich and solvent-rich phases, respectively. The inset shows a region very near the critical point.

5.1.2 Fluctuations

Semidilute polymer solutions exhibit fluctuations in two different order parameters that become coupled and contribute equally: one is a scalar parameter associated with the polymer volume fraction, and the other is a vector parameter associated with the behavior of long polymer chains.[102] The former is an observable quantity, while the latter can be modeled by de Gennes' radius of gyration[103] for a polymer chain, R_g,

$$R_\mathrm{g} = a\sqrt{N} \,, \tag{5.1.12}$$

where a is the step size in a random walk. The radius of gyration will be the parameter representing the correlation length of fluctuations for the polymer chain order parameter, which is associated with the concentration of chain ends, or probability that the chain ends will meet one another.[103]

Asymptotically close to the critical point of phase separation, the correlation length of concentration fluctuations will dominate and become larger than the polymer chain's radius of gyration, R_g. In this regime, a polymer solution behaves similarly to an ordinary fluid near its critical point. As the solution approaches the theta point, the radius of gyration will become larger than the critical fluctuations, and the solution will exhibit theta-point tricriticality.[101] This behavior is very close to mean-field behavior, with logarithmic corrections required as a result of fluctuations.[97] These scaling concepts, along with crossover between critical fluid behavior and tricritical theta-point behavior, will be applied to calculate the interfacial thickness and Tolman's length in polymer solutions in this chapter.

The limiting behaviors that bound this analysis are low and very high degrees of polymerization as well as temperatures very near and far away from the critical point. For the infinite polymer chain, the polymer volume fraction tends to zero as the correlation length, or radius of gyration, diverges. This condition, when present with a temperature above the theta temperature (θ)—where the second virial coefficient is zero[99] —is analogous to a critical state. By appropriate tuning of the second virial coefficient, this critical state can be modified to a first-order phase transition where the polymer chain collapses onto itself and phase separation occurs. This separation would result in the introduction of a new concentration-based order parameter.

5.2 Tolman's Length in Near-Critical Polymer Solutions

Complete scaling is a universal approach to modeling fluid behavior, and individual characteristics are taken into account by the scaling coefficients. Therefore, this method will be used to model the behavior of a polymer solution and determine the Tolman length near the critical point of separation. In the critical regime, where $w << 1$, the Tolman length for a polymer solution will be determined from Anisimov's[41] result given in Chapter 4 (Eq. (4.2.20)):

$$\delta \cong \mp c_{\delta} \xi_0^- \left[\frac{3}{2} a_{\text{eff}} \hat{B}_0 |\Delta T|^{\beta-\nu} - b_2 \frac{\beta \hat{B}_0}{\hat{\Gamma}_0^{\pm}} |\Delta T|^{1-\alpha-\beta-\nu} \right]. \qquad (5.2.1)$$

5.2.1 Approximation of Scaling Coefficients

As the degree of polymerization and volume fraction affects the asymmetry in a semidilute polymer solution, these are the parameters that will be considered in determining the scaling coefficients in complete scaling. To approximate these values, Flory theory[99] of polymer solutions will be used, where the Gibbs energy of mixing, G^{mix}, is

$$\frac{G^{\text{mix}}}{k_{\text{B}}T} = (1-\phi)\ln(1-\phi) + \frac{\phi}{N}\ln\phi + \chi\phi(1-\phi). \qquad (5.2.2)$$

and the polymer-solvent interaction parameter, χ, as presented in this chapter, is

$$\chi = \frac{\omega}{RT}. \tag{5.2.3}$$

The variable ω represents the molecular interactions between solvent molecules, polymer molecules and each with themselves, T is the solution temperature and R is the universal gas constant. Assuming a high degree of polymerization where $N \to \infty$, the theta temperature can be expressed as[99] $\theta = 2\omega / R$, therefore the polymer-solvent interaction parameter can be expressed as

$$\chi = \frac{\theta}{2T}. \tag{5.2.4}$$

Since the dimensionless chemical potential of a fluid mixture is an indicator of its asymmetry, Wang and Anisimov[70] found the scaling coefficients a_{eff} (from Eq. (4.2.21)) and b_2 to be

$$a_{\text{eff}} = \frac{a_3}{1+a_3} = \frac{2}{3}\frac{\hat{\mu}_{21}}{\hat{\mu}_{11}} - \frac{1}{5}\frac{\hat{\mu}_{40}}{\hat{\mu}_{30}} \tag{5.2.5}$$

and

$$b_2 \cong \frac{1}{\hat{\mu}_{11}}\left[\frac{\hat{\mu}_{21}}{\hat{\mu}_{11}} - \frac{1}{5}\frac{\hat{\mu}_{40}}{\hat{\mu}_{30}}\right]. \tag{5.2.6}$$

The notation $\hat{\mu}_{ij} = \partial^{i+j}\hat{\mu} / \Delta\hat{\phi}^i \partial\Delta\hat{T}^j$ in Eqs. (5.2.5) and (5.2.6) represent the derivatives of the chemical potential taken at the critical point, where the volume fraction is analogous to density.

The Flory theory expression in Eq. (5.2.2) can also be written in terms of the chemical potential by taking the first derivative of the Gibbs energy of mixing with respect to solvent volume fraction:

$$\hat{\mu} = \frac{\mu}{k_\mathrm{B}T_\mathrm{c}} = \frac{\partial(G^\mathrm{mix}/k_\mathrm{B}T)}{\partial\phi}\left(\frac{T}{T_\mathrm{c}}\right)$$

$$\hat{\mu} = \frac{T}{T_\mathrm{c}}\left[\frac{1}{N}\ln\phi - \ln(1-\phi) + \left(\frac{1-N}{N}\right) + \frac{\theta}{2T}(1-2\phi)\right]. \qquad (5.2.7)$$

Noting that the dimensionless volume fraction is

$$\hat{\phi} \equiv \frac{\phi}{\phi_\mathrm{c}}, \qquad (5.2.8)$$

the derivatives needed to solve for the scaling coefficients in Eqs. (5.2.5) and (5.2.6), evaluated at the critical point become

$$\hat{\mu}_{10} = \left(\frac{\partial\hat{\mu}}{\partial(\phi/\phi_\mathrm{c})}\right)_T = \phi_\mathrm{c}\left(\frac{\partial\hat{\mu}}{\partial\phi}\right)_T = \frac{T}{T_\mathrm{c}}\left[\frac{\phi_\mathrm{c}}{1-\phi_\mathrm{c}} + \frac{\phi_\mathrm{c}}{N}\right] - \frac{\theta\phi_\mathrm{c}}{T_\mathrm{c}}$$

$$\hat{\mu}_{20} = \left(\frac{\partial^2\hat{\mu}}{\partial(\phi/\phi_\mathrm{c})^2}\right)_T = \phi_\mathrm{c}^2\left(\frac{\partial^2\hat{\mu}}{\partial\phi^2}\right)_T = \frac{T}{T_\mathrm{c}}\left[\frac{\phi_\mathrm{c}^2}{(1-\phi_\mathrm{c})^2} - \frac{1}{N}\right]$$

$$\hat{\mu}_{30} = \left(\frac{\partial^3\hat{\mu}}{\partial(\phi/\phi_\mathrm{c})^3}\right)_T = \phi_\mathrm{c}^3\left(\frac{\partial^3\hat{\mu}}{\partial\phi^3}\right)_T = 2\frac{T}{T_\mathrm{c}}\left[\frac{\phi_\mathrm{c}^3}{(1-\phi_\mathrm{c})^3} + \frac{1}{N}\right]$$

$$\hat{\mu}_{40} = \left(\frac{\partial^4\hat{\mu}}{\partial(\phi/\phi_\mathrm{c})^4}\right)_T = \phi_\mathrm{c}^4\left(\frac{\partial^4\hat{\mu}}{\partial\phi^4}\right)_T = 6\frac{T}{T_\mathrm{c}}\left[\frac{\phi_\mathrm{c}^4}{(1-\phi_\mathrm{c})^4} - \frac{1}{N}\right]$$

$$\hat{\mu}_{11} = \frac{\partial^2\hat{\mu}}{\partial(\phi/\phi_\mathrm{c})\partial(T/T_\mathrm{c})} = \phi_\mathrm{c}T_\mathrm{c}\frac{\partial^2\hat{\mu}}{\partial\phi\partial T} = \frac{\phi_\mathrm{c}}{(1-\phi_\mathrm{c})} + \frac{1}{N}$$

$$\hat{\mu}_{21} = \frac{\partial^3\hat{\mu}}{\partial(\phi/\phi_\mathrm{c})^2\partial(T/T_\mathrm{c})} = \phi_\mathrm{c}^2T_\mathrm{c}\frac{\partial^3\hat{\mu}}{\partial\phi^2\partial T} = \frac{\phi_\mathrm{c}^2}{(1-\phi_\mathrm{c})^2} - \frac{1}{N}. \qquad (5.2.9)$$

The derivatives in Eq. (5.2.9) can also be written in terms of known quantities for polymer solutions, such as the degree of polymerization, N. According to Flory theory,[99] the critical temperature and critical volume fraction of a polymer solution are

$$T_{\mathrm{c}}=\frac{\theta}{\left(1+1/\sqrt{N}\right)^{2}} \tag{5.2.10}$$

and

$$\phi_{\mathrm{c}}=\frac{1}{1+\sqrt{N}}, \tag{5.2.11}$$

respectively. Applying these relations to the derivatives in Eq. (5.2.9) yields the following:

$$\begin{gathered}
\hat{\mu}_{30}=2\frac{T(1+1\sqrt{N})^{2}}{\theta}\left(\frac{\sqrt{N}+1}{N\sqrt{N}}\right) \\
\hat{\mu}_{40}=6\frac{T(1+1\sqrt{N})^{2}}{\theta}\left(\frac{1-N}{N^{2}}\right) \\
\hat{\mu}_{11}=\frac{\sqrt{N}+N}{N\sqrt{N}} \\
\hat{\mu}_{21}=0.
\end{gathered} \tag{5.2.12}$$

Finally, substituting these relations into Eqs. (5.2.5) and (5.2.6) gives the result for the scaling coefficients a_{eff} and b_2 in terms of the degree of polymerization:

$$a_{\mathrm{eff}}=\frac{3}{5}\left(\frac{N-1}{N+\sqrt{N}}\right) \tag{5.2.13}$$

$$b_{2}\cong a_{\mathrm{eff}}\frac{N\sqrt{N}}{N+\sqrt{N}}, \tag{5.2.14}$$

which is the result of Anisimov and St. Pierre.[104]

Plots of Eqs. (5.2.13) and (5.2.14) can be seen in Fig. 5.2. As shown in Fig. 5.2, the scaling coefficient a_{eff} approaches 3/5 as the degree of polymerization increases. Also, the coefficient b_2 follows a power law function as it approaches an infinite degree of polymerization.

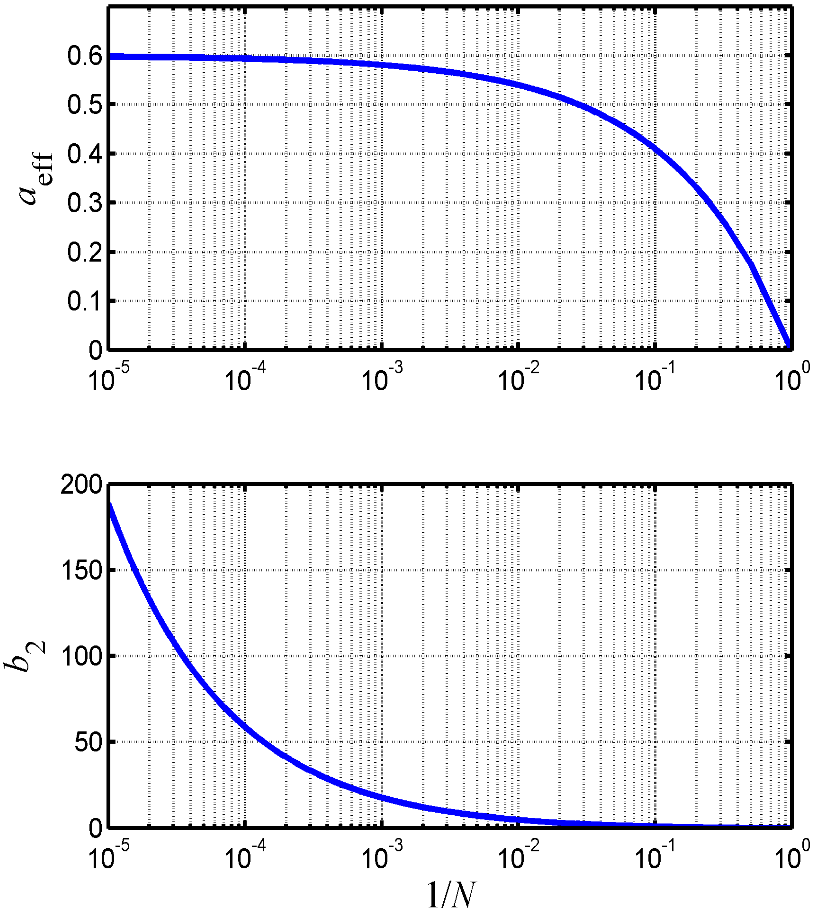

Figure 5.2. Plots of a_{eff} and b_2 against inverse degree of polymerization ($1/N$) for the range $N = 1$ to 10^5. Plots for a_{eff} and b_2 are based on Eqs. (5.2.13) and (5.2.14), respectively.

5.2.2 Approximation of Critical Amplitudes

The necessary critical amplitudes to calculate the Tolman length can also be determined for polymer solutions. The amplitudes, not surprisingly, are also dependent on the degree of polymerization. Anisimov *et al.*[101] and Anisimov and Sengers[105] determined that the critical amplitudes (as the average molecular volume becomes infinitely large) become

$$\Gamma_0 = a_0^{-1} g_0 \left(\frac{N}{c^2}\right)^{\frac{1}{2}(1-\gamma)}$$

$$B_0 = \frac{b\lambda_0^{1/2}}{\sqrt{6}(6v_0{}^3)^{1/4}c^{1/2}}\left(\frac{N}{c^2}\right)^{(\beta-1)/2} \tag{5.2.15}$$

$$\xi_0 \cong r_0 c^{1/2}\left(\frac{N}{c^2}\right)^{(1-\nu)/2}$$

where a_0 and u_0 are system-dependent constants from Landau expansion discussed in Chapter 2, λ_0 is a constant related to the second virial coefficient, v_0 is the molecular volume, c is a system-dependent constant related to the Ginsburg number, r_0 is the "bare" interaction range for $N = 1$, and g_0 is a universal numerical prefactor. The critical exponent γ follows the Ising relation $\alpha + 2\beta + \gamma = 2$; therefore, $\gamma \cong 1.239$. Taking into account the definition of dimensionless susceptibility for polymer solutions,

$$\hat{\chi} \equiv \left(\frac{\partial(\phi/\phi_{\mathrm{c}})}{\partial\hat{\mu}}\right)_{\hat{T}}, \tag{5.2.16}$$

the expressions for the critical amplitudes can be made dimensionless and simplified to focus only on the dependence on the degree of polymerization, such that

$$\hat{\Gamma}_0^- = \frac{\Gamma_0^-}{\phi_c} k_B T_c = \Gamma_{0,N=1} \frac{\left(1+\sqrt{N}\right) N^{(1-\gamma)/2}}{\left(1+1/\sqrt{N}\right)^2}$$

$$\hat{B}_0 = \frac{B_0}{\phi_c} = B_{0,N=1} \left(1+\sqrt{N}\right) N^{(\beta-1)/2} \tag{5.2.17}$$

$$\xi_0 \cong \xi_{0,N=1} N^{(1-\nu)/2} \cong r_0 N^{(1-\nu)/2}.$$

Based on the approximation of $c \cong 2$ for Flory theory,[101] we can assume that the coefficient is of the order of monomer or fragment size where $\xi_{0,N=1} \cong r_0$.

The coefficients in Eq. (5.2.17) can also be approximated from different theories. Based on the Ising model for the mean-field approximation ($N=1$), the amplitudes are $\Gamma_{0,N=1} \cong 1$ and $B_{0,N=1} \cong \sqrt{3}$.[50,98] However, as discussed previously, the value of $B_{0,N=1}$ decreases to unity ($B_{0,N=1} \cong 1$) due to critical fluctuations in the three-dimensional Ising model for short-range interactions,[50] therefore this value will be used.

5.2.3 Tolman's Length near the Critical Point

Since the critical amplitudes and scaling coefficients can all be approximated in terms of the degree of polymerization as shown in Eqs. (5.2.13), (5.2.14) and (5.2.17), we can determine the Tolman length for a polymer solution based on the degree of polymerization, temperature distance to the critical point using Eq. (5.2.1). This equation can be made dimensionless and universal for polymer solutions by dividing the Tolman length by the molecular size, r_0, such that

$$\frac{\delta}{r_0} \cong \mp c_\delta N^{(1-\nu)/2} \left[\frac{3}{2} a_{\mathrm{eff}} B_0 \left|\Delta T\right|^{\beta-\nu} - b_2 \frac{\beta B_0}{\Gamma_0^-} \left|\Delta T\right|^{1-\alpha-\beta-\nu} \right]. \tag{5.2.18}$$

A three-dimensional graphical representation of the dimensionless Tolman length for a droplet of polymer in solution, based on these approximations and the assumption that $c_\delta \cong 2/3$, is given in Fig. 5.3. Notice that in this figure there is a dramatic increase in Tolman's length close to the critical point and at a relatively high degree of polymerization ($N = 10^4$). The magnitude of the Tolman length also appears to be more strongly dependent on the degree of polymerization, and thus asymmetry, relative to temperature distance.

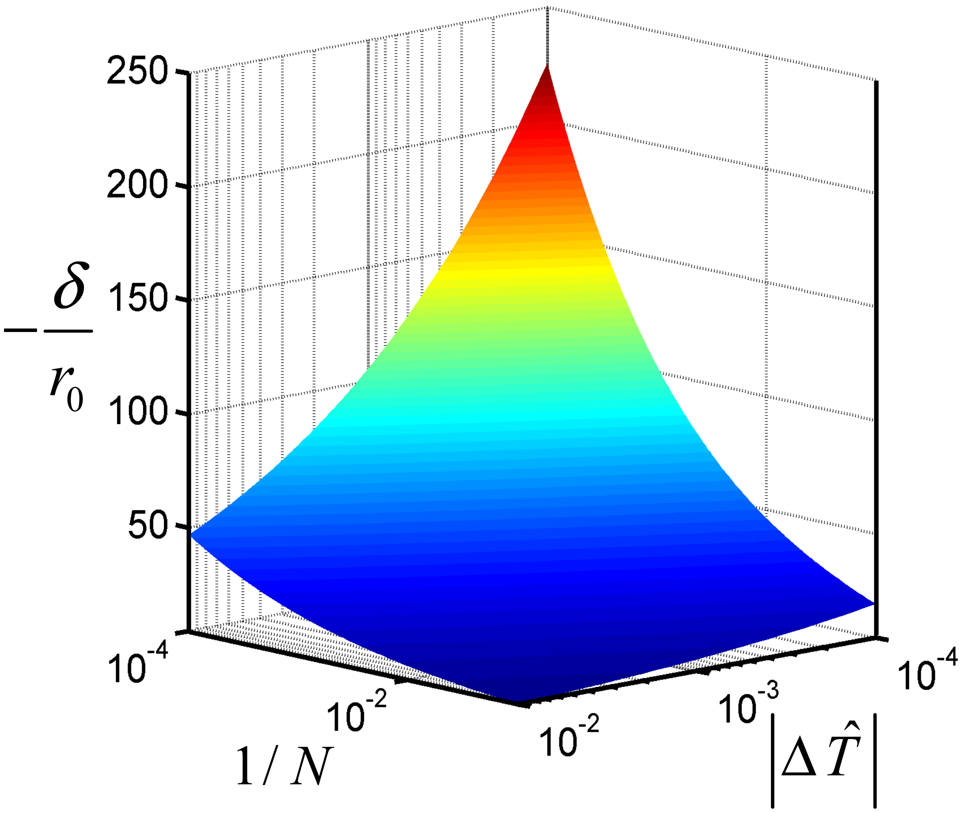

Figure 5.3. Three-dimensional plot of the dimensionless near-critical Tolman length for a droplet of polymer in solution (from Eq. (5.2.18)). It is assumed $c_\delta \cong 2/3$ and $\xi_{0,N=1} \cong r_0$.

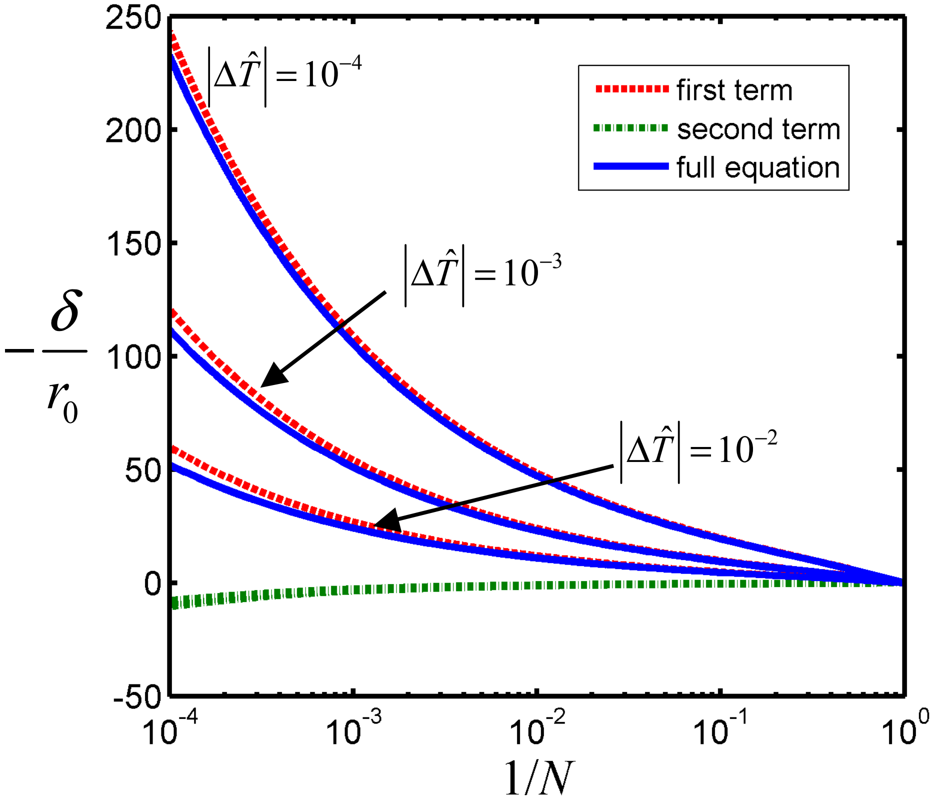

Figure 5.4. Plots of the two terms from the dimensionless Tolman length for a droplet of polymer in solution at three temperatures. Shown here are Eqs. (5.2.18) and (5.2.19) for the full and partial expressions, respectively.

5.2.4 Comparison of Terms

Anisimov's[45] expression for the Tolman length given in Eq. (5.2.18) can also be further simplified for a more simple approximation. By comparing the contribution of each term in this equation where

$$\text{first term: } \mp\frac{3}{2}c_{\delta}N^{(1-\nu)/2}a_{\text{eff}}\hat{B}_0\left|\Delta\hat{T}\right|^{\beta-\nu}$$

$$\text{second term: } \pm c_{\delta}N^{(1-\nu)/2}b_2\frac{\beta\hat{B}_0}{\hat{\Gamma}_0^-}\left|\Delta\hat{T}\right|^{1-\alpha-\beta-\nu}, \tag{5.2.19}$$

we can determine a way to simplify the complete expression for Tolman's length. In the first term, temperature depends as $\left|\Delta\hat{T}\right|^{-0.304}$, showing a much stronger divergence as compared to the weak divergence in the second term, $\left|\Delta\hat{T}\right|^{-0.065}$. A visual comparison of the two terms is in Eq. (5.2.19) is made in Fig. 5.4. In this figure, we can see that the contribution of the first term dominates by far, due to the magnitude of the critical exponents. The first term diverges strongly while the second term is nearly independent of temperature and only indicates a slight difference at high degrees of polymerization. As a result of this comparison, a simplification can be made for engineering approximations which takes only the first term into consideration.

The equation for the near-critical Tolman length (Eq. (5.2.18)) can also be expressed in terms of Widom's variable w in Eq. (5.1.1). Considering Eqs. (5.2.13), (5.2.14) and (5.2.17) at a moderate to high degree of polymerization ($N \geq 100$), these values become:

$$a_{\text{eff}}(N \geq 100) \rightarrow \frac{3}{5} \tag{5.2.20}$$

$$b_2(N \geq 100) \rightarrow \frac{3}{5}\sqrt{N} \tag{5.2.21}$$

$$\hat{\Gamma}_0^-(N \geq 100) \rightarrow \Gamma_{0,N=1}N^{(2-\gamma)/2} \tag{5.2.22}$$

$$\hat{B}_0(N \geq 100) \to B_{0,N=1} N^{\beta/2}. \tag{5.2.23}$$

The comparison of the results in Eqs. (5.2.20)-(5.2.23) for a moderate to high degree of polymerization, and the results for the full *N*-dependence equation in Eq. (5.2.17) for the amplitudes $\hat{\Gamma}_0^-$ and $\hat{B}_0$ can be seen in Fig. 5.5. Note that there is little difference in the plots for $\hat{\Gamma}_0^-$ and $\hat{B}_0$, which indicate little difference for values of $N \geq 100$.

By applying the values in Eqs. (5.2.21)-(5.2.23), as well as the definitions of w and radius of gyration, the expression for Tolman's length in polymer solutions near the critical point becomes

$$\delta \cong \mp c_\delta R_\text{g} a_\text{eff} \left[\frac{3}{2} w^{\beta - \nu} - \beta w^{1-\alpha-\beta-\nu} \right] \tag{5.2.24}$$

when $\Gamma_{0,N=1} \cong 1$ and $B_{0,N=1} \cong 1$ using the three-dimensional Ising model, and $2^{\beta-\nu} \cong 2^{1-\alpha-\beta-\nu} \cong 1$. The second of the two temperature-dependent terms in this equation diverges weakly, as $w^{1-\alpha-\beta-\nu} \cong w^{-0.065}$, and the leading term diverges more strongly as $w^{\beta-\nu} \cong w^{-0.304}$. A comparison of the contribution of these two terms indicates that the only term of significance is the leading term, especially when approaching the critical point as shown in Fig. 5.4. Therefore, the expression for the Tolman length in the critical regime simply becomes

$$\delta \cong \mp a_\text{eff} R_\text{g} x^{\beta-\nu}. \qquad \text{(critical regime)} \tag{5.2.25}$$

which assumes $c_\delta \cong 2/3$.

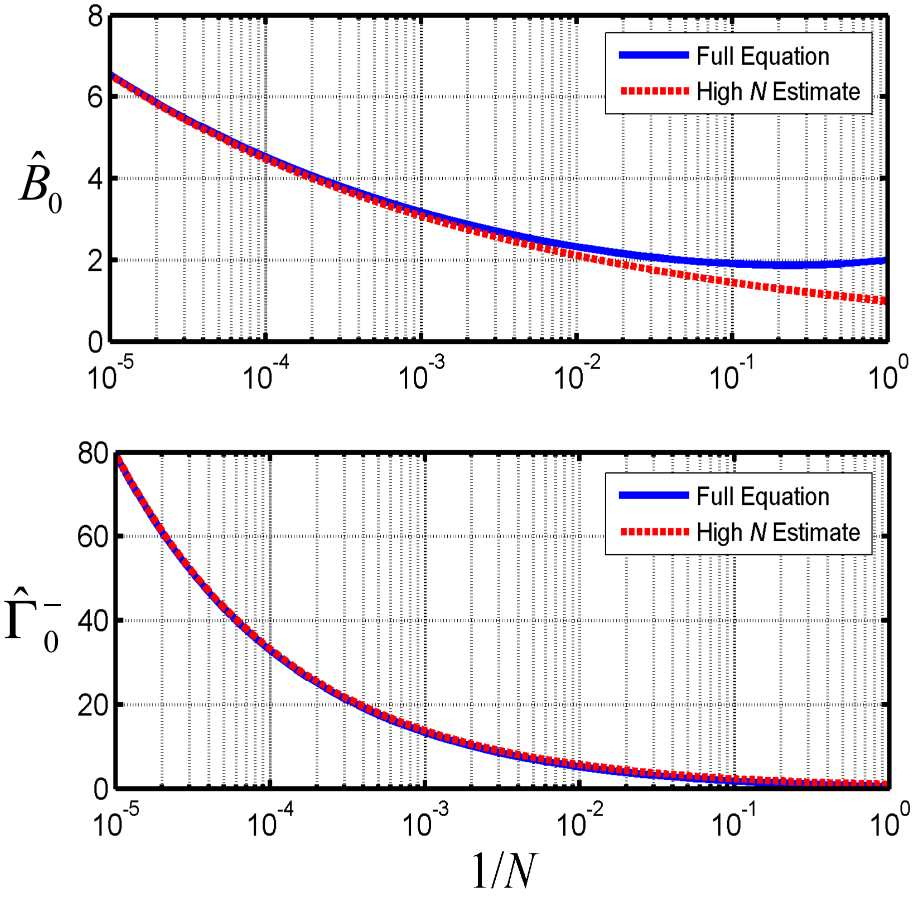

Figure 5.5. Comparison of *N*-dependent amplitudes $\hat{B}_0$ and $\hat{\Gamma}_0^-$ for a moderate to high degree of polymerization. Eqs. (5.2.22) and (5.2.23) represent the high *N* estimate and Eq. (5.2.17) represents the equation for all values of *N*.

5.3 Tolman's Length at High Degrees of Polymerization

As the correlation and Tolman's lengths at high degrees of polymerization (when $w >> 1$) are expected to behave differently than in the critical regime, a new set of equations will be developed. In the mean-field approximation, where $\beta = \nu = 1/2$, Eq. (5.2.25) for the critical regime would be independent of temperature ($\delta \cong \mp a_{\text{eff}} R_{\text{g}}$), a significant departure from the results of complete scaling. Some studies indicate similar mean-field-like results are expected for the polymer regime.[103,105,106]

As discussed in Section 5.1, for an infinite degree of polymerization, the limit of phase separation approaches an asymptotic line that extends from the theta temperature, shown in Fig. 5.1. At this limit of the infinite degree of polymerization, the radius of gyration of a polymer chain becomes significantly greater than the correlation length of critical fluctuations. The correlation length at a high degree of polymerization, $\xi_{N\to\infty}$, then becomes dependent on the radius of gyration and is given by deGennes'[103] scaling theory for the semi-dilute phase of a polymer solution:

$$\xi_{N\to\infty} \sim r_0\left(\chi-\frac{1}{2}\right)^{-1} \sim r_0\left(\frac{\omega}{RT}-\frac{1}{2}\right)^{-1}. \tag{5.3.1}$$

At a high degree of polymerization, the theta temperature becomes $\theta = 2\omega / R$, and Eq. (5.3.1) becomes

$$\xi_{N\to\infty} \sim 2r_0\left(\frac{\theta-T}{T}\right)^{-1}. \tag{5.3.2}$$

At a high degree of polymerization when $w\to\infty$, since $N\to\infty$ at any given temperature, we can approximate the theta point temperature distance as

$$\frac{\theta-T}{T} \cong \Delta\hat{T}. \tag{5.3.3}$$

Therefore, Eq. (5.3.2) for the polymer correlation length can be expressed as

$$\xi_{N\to\infty} \cong 2r_0\left|\Delta\hat{T}\right|^{-1}, \tag{5.3.4}$$

or in terms of the Widom variable (Eq. (5.1.1)) and radius of gyration (Eq. (5.1.12)), the equation becomes[104]

$$\xi_{N\to\infty} \cong R_{\mathrm{g}} w^{-1} . \tag{5.3.5}$$

Here, it can be assumed that the size of the monomer, r_0, is on the same order as the random walk step size in a polymer chain ($r_0 \cong a$). This expression in Eq. (5.3.5) supports a similar result obtained by Szleifer and Widom[102] for the mean-field (Flory) approximation for semi-dilute polymer solutions.

It should be mentioned that there is some disagreement over the proper temperature variable in the polymer regime. De Gennes[103] and Broseta[107] stated that the temperature variable away from the critical regime ($w >> 1$) should be defined as $(T_{\mathrm{c}} - T)/(\theta - T_{\mathrm{c}})$ instead of $\Delta\hat{T} \equiv (T - T_{\mathrm{c}})/T_{\mathrm{c}}$ as shown in this work and others[97,104] because it accounts for the temperature at which monomer-monomer interactions vanish. However, as discussed further by Widom,[97] the temperature variable $\Delta\hat{T}$ and related variable w provide comparable results to this suggested temperature variable when compared to experimental results.

As presented in Chapter 4, the asymmetry of a solution as indicated by the coexistence curve can assist in determining the Tolman length within droplets of solution. Moving away from the critical regime toward the polymer regime, the coexistence diameter becomes linear and its slope represents the asymmetry of the solution. As previously indicated in Eq. (4.3.1), this diameter can generally be used to determine the Tolman-correlation length ratio; in terms of volume fraction, this equation becomes[104]

$$\frac{\delta}{2\xi} \cong \mp \frac{\Delta\phi_{\mathrm{d}}}{\phi'' - \phi'} \tag{5.3.6}$$

where ϕ'' is the volume fraction in the polymer-rich phase and ϕ' is the volume fraction in the solvent-rich phase. By this definition, the prefactor "$-$" refers to the correction for a polymer-rich droplet in solution and the "$+$" refers to the correction for a droplet of solvent. Away from the critical point as the solution diameter ($\Delta\phi_{\mathrm{d}} = \phi_{\mathrm{d}} - \phi_{\mathrm{c}}$) for a highly asymmetric solution approaches one half of the distance between the coexisting phases ($\phi'' - \phi'$), the Tolman-correlation length ratio for polymer solutions in the polymer regime becomes[104]

$$\left(\frac{\delta}{\xi}\right)_{N\to\infty} = \mp 1. \tag{5.3.7}$$

This expression for $w >> 1$ is quite dramatic, as it indicates that the Tolman length is expected to be as large as half of the interface thickness, if the interface is defined as 2ξ. This result is consistent with Rowlinson's[31] and Anisimov and St. Pierre's[104] predictions that the Tolman length is expected to be on the same order as the interface thickness for small droplets.

5.4 Crossover Expression for Tolman's Length in Polymer Solutions

Now that the behavior of Tolman's length has been determined for the limiting behavior in both the critical and polymer regimes, the behavior between these two limits can be modeled. In order to achieve an understanding of the Tolman length in this 'unknown' region, simple crossover expressions will be developed based on the Widom variable, w, at the known behavior at the limit $N \to \infty$ and approaching the critical point. As before, the defining parameters for the two regimes are w and the size of fluctuations in the polymer chain relative to the radius of gyration:

$$\text{Critical regime: } w << 1 \text{ and } R_{\text{g}} << \xi$$

$$\text{Polymer regime: } w << 1 \text{ and } R_{\text{g}} \to \infty.$$

5.4.1 Crossover Correlation Length

Since the basis of the approximation of Tolman's length is relative to the thickness of the interface, which is based on the size of the fluctuations in a polymer solution, the first expression developed is the crossover correlation length. As the expression for the correlation length of critical fluctuations in the critical regime given in Chapter 3 (Eq. (2.2.1)),

$$\xi = \xi_0 \left| \Delta \hat{T} \right|^{-\nu}, \quad \text{(critical regime)} \tag{5.4.1}$$

is universal for any fluid, we can apply this same expression to polymer solutions in the critical regime, taking in the system-dependent amplitude ξ_0 in Eq. (5.2.17). In writing this expression in terms of Widom's w, it becomes[104]

$$\xi = R_{\text{g}} w^{-\nu}, \qquad \text{(critical regime)} \tag{5.4.2}$$

since $2^{-\nu} \cong 1$.

As discussed in the previous section, the limiting behavior in the polymer regime is given by Eq. (5.3.5). Combining what is known of this behavior in the polymer regime with that is known for the critical regime in Eq. (5.4.2), we propose as a simple crossover expression:[104]

$$\xi_{\times} \cong \frac{R_{\text{g}} w^{-\nu}}{\left(1+w\right)^{1-\nu}}. \qquad \text{(crossover)} \tag{5.4.3}$$

A simple check of this crossover expression yields the limiting expressions: for large values of w, $\xi_\times$ is the result for the polymer regime (Eq. (5.3.5)) and for small values of w, $\xi_\times$ is the result for the critical regime (Eq. (5.4.2)).

5.4.2 Crossover Tolman-Correlation Length Ratio

The crossover concept can be taken a step further and applied to the ratio of the Tolman length to the correlation length to obtain a good approximation of the size of the curvature correction relative to the interface thickness of a droplet of polymer in solution. As before, this correction for a droplet of polymer-rich phase would be negative, whereas the correction to a solvent droplet would be positive. Referencing Eq. (4.2.19) in Chapter 4, one of the universal equations for the Tolman-correlation length ratio,

$$\frac{2\delta}{\xi} \cong \mp c_\delta \left[\frac{3a_3}{1+a_3} \hat{B}_0 |\Delta T|^\beta - 2b_2 \frac{\beta \hat{B}_0}{\hat{\Gamma}_0^\pm} |\Delta T|^{\beta-1+\gamma} \right], \tag{5.4.4}$$

we can determine the ratio specifically for polymer solutions. As before, the characteristic variable, w and the system-dependent amplitudes and coefficients for polymer solutions for moderate degrees of polymerization (Eqs. (5.2.21)-(5.2.23)) can be applied to this equation, therefore:

$$\frac{\delta}{\xi} \cong \mp c_\delta a_{\text{eff}} \left[\frac{3}{2} w^\beta - 2\beta w^{1-\alpha-\beta} \right]. \tag{5.4.5}$$

Given that the first term diverges more strongly and the results of the term analysis in Section 5.2 show that the first term dominates by far, we can simplify the equation to:

$$\frac{\delta}{\xi} \cong \mp a_{\text{eff}} w^\beta, \qquad \text{(critical regime)} \tag{5.4.6}$$

where, as before, we can assume[41] $c_\delta \cong 2/3$. Since the coefficient $a_{\text{eff}} \to 3/5$ at moderate degrees of polymerization ($N \geq 100$), the scaling coefficient can be approximated as $a_{\text{eff}} \cong 1$, as given by Anisimov and St. Pierre.[104] Therefore, the ratio of Tolman length relative to interfacial thickness in Eq. (5.4.6) simply becomes

$$\frac{\delta}{\xi} \cong \mp w^{\beta}. \qquad \text{(critical regime)} \qquad (5.4.7)$$

As the Tolman-correlation length ratio for the polymer regime has been established to be $(\delta/\xi)_{N\to\infty} = \mp 1$ in Section 5.3, the following crossover expression between the polymer and critical regimes can be developed:

$$\left(\frac{\delta}{\xi}\right)_{\times} \cong \mp \frac{a_{\text{eff}} w^{\beta}}{(1+a_{\text{eff}}^{1/\beta} w)^{\beta}}. \qquad (5.4.8)$$

As presented by Anisimov and St. Pierre[104] for a simple approximation at moderate degrees of polymerization, Eq. (5.4.8) can be simplified to

$$\left(\frac{\delta}{\xi}\right)_{\times} \cong \mp \frac{w^{\beta}}{(1+w)^{\beta}}. \qquad (5.4.9)$$

This equation can provide a good approximation of the Tolman's length correction to the surface tension relative to the correlation length of fluctuations.

5.4.3 Crossover Tolman's Length

Lastly, an expression that bridges the gap between the polymer regime limit and the critical regime limit can be developed for the Tolman's length. Combining the relationships developed in Eqs. (5.4.3) and (5.4.8), the crossover Tolman's length expression becomes:

$$\delta_{\times} \cong \mp \frac{a_{\mathrm{eff}} R_{\mathrm{g}} w^{\beta-\nu}}{(1+a_{\mathrm{eff}}^{1/\beta} w)^{\beta} \left(1+w\right)^{1-\nu}} . \tag{5.4.10}$$

For the sake of simplicity, Eq. (5.4.10) can be written as

$$\delta_{\times} \cong \mp \frac{R_{\mathrm{g}} w^{\beta-\nu}}{(1+w)^{1+\beta-\nu}} , \tag{5.4.11}$$

as presented by Anisimov and St. Pierre.[104] Again, these simple crossover equations can be tested by considering the critical and polymer regime limits. When w is very small, Eq. (5.4.10) reduces to the expression for the Tolman length in the critical regime in Eq. (5.2.25) . Equation (5.4.11) reduces to the simplified expression

$$\delta \cong \mp R_{\mathrm{g}} w^{\beta-\nu}, \qquad \text{(critical regime)} \tag{5.4.12}$$

where $a_{\mathrm{eff}} \to 3/5 \cong 1$. When w is very large, Eqs. (5.4.10) and (5.4.11) reduce to the expression for the polymer regime (Eq. (5.3.5)).

Figure 5.6 illustrates the universal Tolman's length behavior for a drop of polymer-rich phase in solution as predicted by Eq. (5.4.11). As expected, these results show a divergence of the Tolman's length with increasing degree of polymerization and decreasing proximity to the critical point of phase separation.

Further analysis of this methodology revealed that this crossover expression is in agreement with the selected characteristic variable, w. Fig. 5.7 illustrates the crossover temperature dependence of the Tolman's length between the critical and polymer regimes for a given degree of polymerization. For the case of $N = 10^4$, careful examination of the intersection of the lines tangent to the critical and polymer regime behaviors ($\beta - \nu \cong -\ 0.304$ and $-\ 1$, respectively) showed the crossover temperature to be $|\Delta\hat{T}| \cong 10^{-1.67}$, yielding a value of unity ($w \cong 1$), which is in very close agreement with the definition used in Widom's[97] characteristic variable.

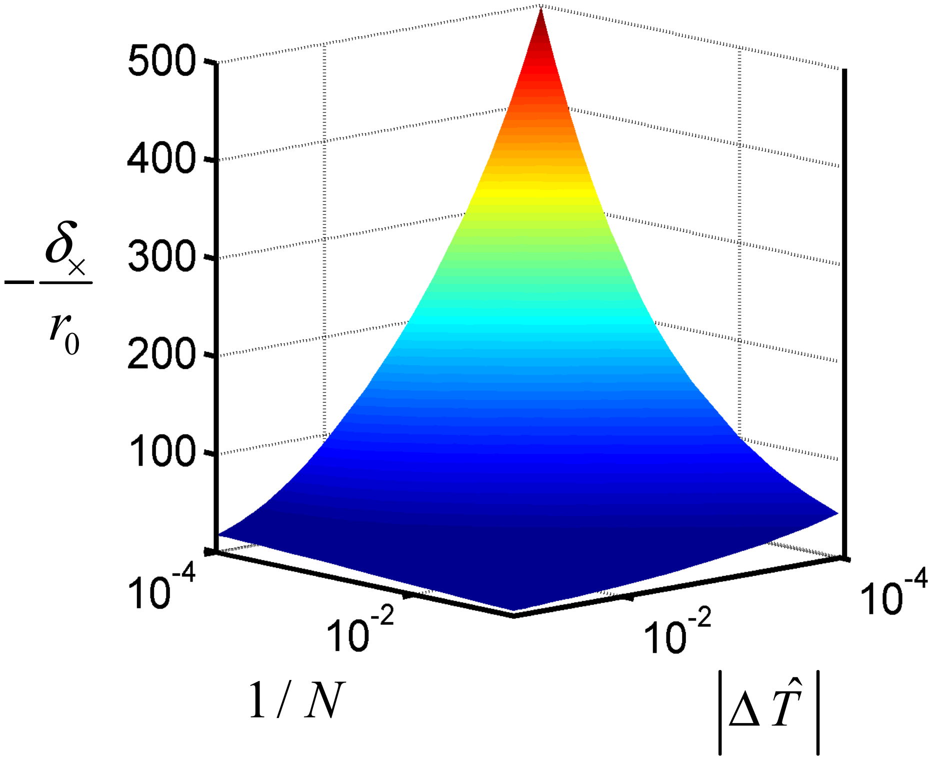

Figure 5.6. Universal behavior of the dimensionless Tolman length with respect to degree of polymerization and temperature distance to phase separation for a polymer-rich droplet as predicted by Eq. (5.4.11)

Two simple examples further illustrate the effects of Tolman's length as shown in Fig. 5.6. Consider a polymer solution with a degree of polymerization $N = 10^4$ and a monomer size (or random walk step size) of $r_0 \cong 0.2$ nm and a temperature distance from the critical point of separation, $|\Delta\hat{T}| \cong 10^{-4}$. When the random walk step size is approximated as the monomer size ($a \cong r_0$), a droplet of this polymer in solution would exhibit a radius of gyration of approximately 20 nm and a Tolman's length of $\delta \cong -100\ \text{nm}$, given Eqs. (5.1.12) and (5.4.11), respectively.

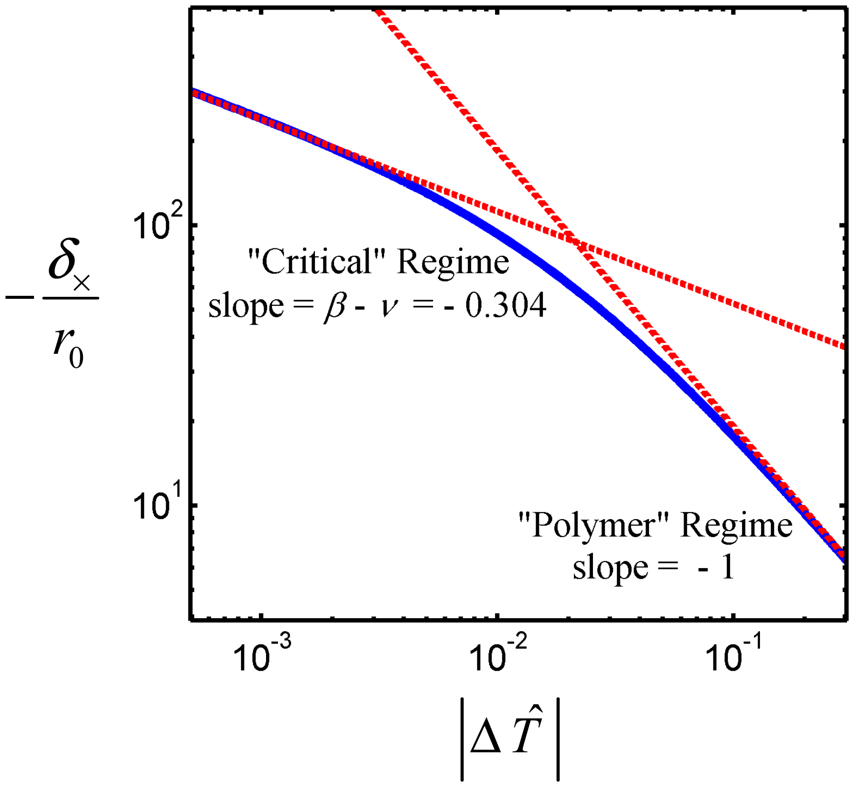

Figure 5.7. Dimensionless Tolman length for a polymer-rich droplet with $N = 10^4$ exhibiting crossover between the critical and polymer regimes from Eq. (5.4.11). The intersection of the two tangent lines occurs at $|\Delta \hat{T}| \cong 10^{-1.67}$, therefore $w \cong 1$.

Another example is that of a polystyrene-cyclohexane solution 3 K from the critical temperature,[101] where $|\Delta \hat{T}| \cong 10^{-2}$. From Eq. (5.4.11), the Tolman length correction would be - 20 nm with an interface thickness (2ξ) of approximately 40 nm. Therefore, for a droplet of polymer with a radius of $0.4\mu\text{m}$, there would be a 10% increase to the surface tension, based on the Laplace-Tolman equation (Eq. (4.1.4)) in Chapter 4:

$$\sigma(R) = \sigma_\infty \left(1 - \frac{2\delta}{R} + \ldots \right). \tag{5.4.13}$$

5.5 Tolman's Length in Other Polymer Applications

As expected by the information and models presented thus far in this work, Tolman's length is expected to be present in curved surfaces of asymmetric fluids, including polymer solutions. Another application of this correction to asymmetric solutions is polymer blends. As published by Leermakes *et al.*[108,109] and van Male and Blokhuis,[110] a three-component system—such as a polymer blend consisting of a solvent and two different polymers—can be reduced to a two-component system of two polymer-rich phases. Should these polymers not exhibit symmetry with respect to the Flory model and have differing degrees of polymerization, the solution will be asymmetric and thus require a correction to the surface tension for small droplets of polymer.

5.6 Near-Critical Tolman's Length in Dilute Binary Mixtures

Similar to the information presented in this chapter for polymer solutions, the Tolman length near the critical point can also be determined for a particular dilute binary mixture exhibiting fluid asymmetry. Considering the full expression for the near-critical Tolman's length given in Chapter 4 (Eq. (4.2.20)),

$$\delta \cong \mp c_\delta \xi_0^- \left[\frac{3}{2} a_{\text{eff}} \hat{B}_0 \left| \Delta T \right|^{\beta-\nu} - b_2 \frac{\beta \hat{B}_0}{\hat{\Gamma}_0^\pm} \left| \Delta T \right|^{1-\alpha-\beta-\nu} \right], \tag{5.6.1}$$

we can approximate the curvature correction to the surface tension for small droplets or bubbles of dilute binary mixtures given the scaling coefficients and critical amplitudes that are specific to the solution of interest. In Eq. (5.6.1), it should be noted that the coefficient[45] $c_\delta \cong 2/3$, the prefactor $\mp$ refers to a bubble of vapor or a drop of liquid, respectively and

$$a_{\text{eff}} \equiv \frac{a_3}{1+a_3}, \tag{5.6.2}$$

as previously defined in Section 4.2. Considering only the first and strongly diverging term in Eq. (5.6.1), the simplified expression for Tolman' s length becomes:

$$\delta \cong \mp \xi_0^- a_{\text{eff}} \hat{B}_0 \left|\Delta T\right|^{\beta-\nu} . \tag{5.6.3}$$

This simplified expression can easily be used to approximate the curvature correction to the surface tension with very few inputs.

As discussed in Section 3.2, the scaling coefficient a_3 for a one-component fluid can be affected by a change in concentration if a small amount of solute with a vastly different molecular volume is added. The general expression for the concentration-dependence of the scaling coefficient is directly related to the change in critical volume relative to a the amount of solute added, such that

$$a_3(x_{\text{c}}) \cong a_3^0 + \frac{x_{\text{c}}}{V_{\text{c}}} \frac{dV_{\text{c}}}{dx}, \tag{5.6.4}$$

from Eq. (2.2.53) .

This concept was also shown for polymer solutions, where an increasing degree of polymerization—which is directly related to the molecular volume of the polymer—initially increased the size of the scaling coefficient a_{eff} (Eq. (5.2.13)) at lower degrees of polymerization. This behavior is analogous to adding a small amount of solute, with a large molecular volume, to a pure fluid with a small molecular volume. Equation (5.6.3) indicates that as the scaling coefficient a_{eff} increases, so does the Tolman length. If an application involves the creation, interaction with or use of small droplets or bubbles composed of an asymmetric mixture, Tolman's length can potentially be a significant correction to surface tension calculations.

It should also be noted that the expression shown in Eq. (5.6.4) must only be used for dilute binary mixtures as it is a linear approximation of the solution behavior. Therefore, the behavior of each individual dilute mixture should be analyzed to determine the location of the linear region and its associated concentrations that can be used in this approximation. This analysis and example dilute solutions of aqueous *n*-hexane and *n*-heptane-ethane will be discussed more in-depth in Chapter 6.

Chapter 6: Concentration and Density Profiles for Asymmetric Fluids and Binary Fluid Mixtures

6.1 Background and Introduction

Fluid asymmetry—which is primarily indicated by the shape of a one or multi-component fluid—has been linked to many properties including heat capacity[94] and the curvature correction to the surface tension, known as Tolman's length.[45,104] Asymmetry, either inherent in a one-component fluid or caused by the addition of a dissimilar component, can also affect the shape of density and concentration profiles of a pure fluid or mixture. A simple asymmetric vapor-liquid coexistence curve is illustrated in Fig. 6.1.

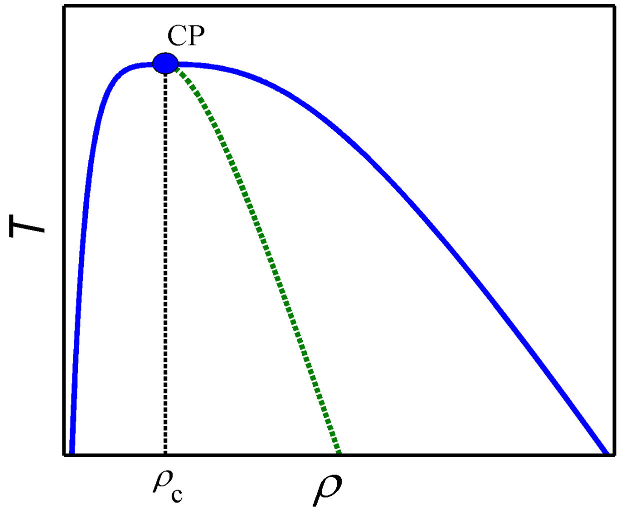

Figure 6.1. Schematic of an asymmetric vapor-liquid coexistence curve. The rectilinear (actual) diameter is given by the dashed green line.

Monte Carlo, molecular dynamics and Renormalization Group simulations can provide accurate modeling of this asymmetry, as can traditional methods of statistical mechanics, but they are not always expressed in simple terms or easily solved. Instead, we will once again look to the universal method of complete scaling as developed in Chapter 3 to model the behavior of a dilute fluid mixture by applying its system-dependent amplitudes and coefficients. Specifically, the focus will be on modeling the increased asymmetry due to the addition of a small amount of solute to a one-component fluid that has a greater preference for one phase of the fluid over the other.

6.2 Determination of Scaling Densities for Use in Complete Scaling

In order to determine the density and concentration profiles using complete scaling, two parameters must be determined: the order parameter and thermal scaling density. To choose these parameters, we must look closely at the physical fields they represent.

A first step is to look at the complete scaling expressions for density and entropy density for one-component fluids and binary mixtures as presented in Section 3.2.:

$$\hat{\rho} = \frac{1+\varphi_1 + b_2\varphi_2}{1 - a_3\varphi_1 - b_3\varphi_2} \tag{5.2.1}$$

$$\hat{\rho}\hat{S} = \frac{\hat{S}_c + a_2\varphi_1 + \varphi_2}{1 - a_3\varphi_1 - b_3\varphi_2}. \tag{5.2.2}$$

If we expand these two equations and neglect all terms of higher order than $\Delta\hat{T}$, the density and entropy density can be expressed as

$$\Delta\hat{\rho} = \hat{\rho} - 1 \cong (1+a_3)\varphi_1 + a_3(1+a_3)\varphi_1^2 + (b_2+b_3)\varphi_2 \tag{5.2.3}$$

and

$$\Delta\left(\hat{\rho}\hat{S}\right) \cong \varphi_2 , \tag{5.2.4}$$

which is identical to the result of Wang[62] and Wang and Anisimov,[68] with the exception that b_3 is considered nonzero in this portion of the analysis. As a result of these expansions, we can see that the order parameter, φ_1, is closely related to the density of the fluid or fluid mixture, and the thermal scaling density, φ_2 is directly related to the entropy density. Therefore, we must select an order parameter and a thermal scaling density that incorporates these real physical densities.

6.2.1 Symmetric Order Parameter

In Chapter 2, the mean-field order parameter was simply defined as the density difference itself, $\varphi_1 = \hat{\rho}$. This definition, however, does not take into account the effect of critical fluctuations.

One method of addressing fluid asymmetry is to apply its affects, by way of the coefficients from complete scaling, to a symmetric interfacial profile that accounts for critical fluctuations as discussed in Chapter 3. As shown in Chapter 3 and in Fig. 6.2, critical fluctuations cause a more gradual and smooth transition from one phase to another, flattening the interfacial density profile. One such example of a profile that accounts for critical fluctuations is the normalized symmetric density profile from Renormalization Group theory obtained by Ohta and Kawasaki[80] presented in Section 3.3 of this work:

$$\Psi(z/2\xi) = \tanh(-z/2\xi)\left[1+\frac{2a}{3+a}\operatorname{sech}^2(-z/2\xi)\right]^{-1/2} \tag{5.2.5}$$

where

$$a = \frac{\sqrt{3}}{6}\pi\varepsilon \qquad \text{and} \qquad \varepsilon = 4 - d\,,$$

and d represents the number of dimensions of the system. As in Chapters 2 and 3, this expression is a function of height, z, and correlation length, ξ, as presented in Section 3.2:

$$\xi = \xi_0 \left|\Delta\hat{T}\right|^{-\nu}. \tag{5.2.6}$$

As before, only the height-dependent coordinate, z, will be considered when addressing the behavior and location of the interface.

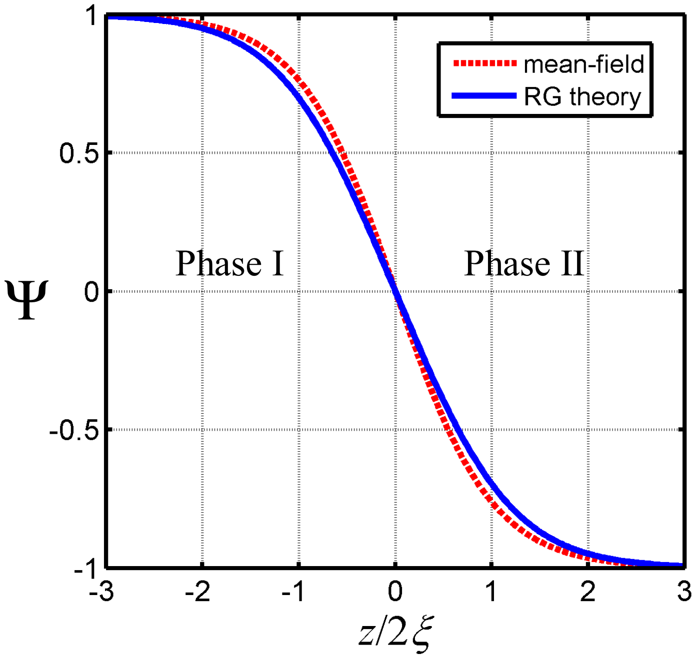

Figure 6.2. Normalized symmetric mean field and Renormalization Group[76] theory profiles

In our case, this normalized symmetric profile in Eq. (2.3.2) can be used to represent the behavior of an interface both near to and far away from the phase boundary. In terms of complete scaling, we can chose this profile to represent the order parameter at the interface of separation, φ_1, normalized to its behavior far from that interface, $\varphi_{1,\pm\infty}$, as $z \to \pm\infty$. Therefore, our equation for the normalized order parameter can be re-written as:

$$\frac{\varphi_1}{\varphi_{1,\pm\infty}} = \tanh(-z/2\xi)\left[1+\frac{2a}{3+a}\operatorname{sec\,h}^2(-z/2\xi)\right]^{-1/2} \tag{5.2.7}$$

where

$$a = \frac{\sqrt{3}}{6}\pi$$

when $d = 3$. Far away from the interface of separation, the profile behaves as the phase boundary for a symmetric fluid below the critical temperature where[64]

$$\varphi_{1,\pm\infty} \cong \pm\hat{B}_0\left|\Delta\hat{T}\right|^{\beta} \qquad (\text{for } z \to \pm\infty) \tag{5.2.8}$$

and the positive and negative values of the expression are accounted for by $\pm z$. As before, the amplitude $\hat{B}_0$ is specific to the fluid being examined. Also in this equation, the $\pm$ prefactor accounts for the two different phases and corresponds to the sign of z. Close to the interface, the model is more dependent on the shape of the interface as it transitions between phases, provided in the RG theory profile. The expression for the symmetric order parameter, φ_1, becomes:

$$\varphi_1 = \varphi_{1,\pm\infty}\tanh(-z/2\xi)\left[1+\frac{2a}{3+a}\operatorname{sec\,h}^2(-z/2\xi)\right]^{-1/2} \tag{5.2.9}$$

where $\varphi_{1,\pm\infty}$ is given in Eq. (5.2.8).

6.2.2 Thermal Scaling Density

To apply complete scaling and model the behavior of dilute mixtures, another important property must be determined: the thermal, or weakly fluctuating, scaling density, φ_2. It has been shown by Wang and Anisimov[68] that the thermal scaling density is the entropy per unit volume; therefore the isochoric heat capacity can be used to evaluate this field. Applying Wang and Anisimov's[68] expression for the isochoric heat capacity and neglecting higher order terms, as done by Wang,[62] the isochoric heat capacity affected by fluctuations can be written as:

$$\left(C_V\right)_{\mathrm{cr}} \cong A_0^- \left|\Delta\hat{T}\right|^{-\alpha} - B_{\mathrm{cr}}. \tag{5.2.10}$$

In this expression, $\hat{B}_{\mathrm{cr}}$ represents the dimensionless critical background part of the heat capacity, where $\hat{B}_{\mathrm{cr}} \equiv B_{\mathrm{cr}} / k_{\mathrm{B}}$. The critical amplitude, A_0^-, is the amplitude of the isochoric heat capacity below the critical point, specific to the fluid of interest. Since the thermal scaling density is the entropy per unit volume, along the two-phase region, it can be expressed as:

$$\varphi_2 \cong \Delta\hat{S} = \int \frac{\left(C_V\right)_{\mathrm{cr}}}{T} dT \cong \frac{A_0^-}{1-\alpha} \Delta\hat{T} \left|\Delta\hat{T}\right|^{-\alpha} - \hat{B}_{\mathrm{cr}} \left|\Delta\hat{T}\right|. \qquad (\text{for } \hat{B}_{\mathrm{cr}} > 0) \tag{5.2.11}$$

Note that this form of Eq. (5.2.11) is of a similar structure as the general expression for the thermal ordering field in Eq. (2.2.10) as presented in Section 3.2. As we are focusing on dilute solutions, we can make the approximation that φ_2 is unaffected by a very small addition of solute and maintains the bulk characteristics of the one-component fluid. The weakly fluctuating field, h_2, can be approximated simply as $h_2 \cong \Delta\hat{T}$ in the first approximation of the incompressible lattice-gas model, where chemical potential and pressure are constant.[62,78]

It should be noted that the expression in Eq. (5.2.11) as written only accounts for the effect of temperature on the profile. Therefore, the thermal scaling density must be modified by one additional term to take into account the effect of height, or *z*-coordinate. This adjustment can be approximated by taking into account the form of the mean-field approximation where the mean-field thermal scaling density is the entropy, or df_0 / dT:

$$\varphi_2 = \frac{1}{2} a_0 \varphi_1^2 \tag{5.2.12}$$

(from Eq. (2.1.10) in Chapter 2) and the coefficient a_0 is a system-dependent coefficient from mean-field theory. As a good model should reduce to the mean-field results in the $\varepsilon = 0$ approximation (where $\varepsilon = 4 - d$; d being the number of dimensions), we expect the thermal scaling density to be of an equivalent form of Eq. (5.2.12). Therefore, for the best approximation, we should multiply the thermal scaling density expression in Eq. (5.2.11) by the square of the normalized order parameter in Eq. (5.2.7) to account for the height dependence of the entropy as well as fluctuations. The resultant expression for the thermal scaling density becomes:

$$\varphi_2 \cong \left(\frac{A_0^-}{1-\alpha} \Delta\hat{T} \left|\Delta\hat{T}\right|^{-\alpha} - \hat{B}_{\mathrm{cr}} \left|\Delta\hat{T}\right| \right) \left(\frac{\varphi_1}{\varphi_{1,\pm\infty}} \right)^2 . \tag{5.2.13}$$

6.3 Modeling Density Profiles for One-Component Fluids

Since complete scaling can be used to model real fluids, accounting for critical fluctuations, but without requiring the development of complicated equations of state, this method will again be used to model the density profiles of real fluids. In Sections 3.2 and 6.2, the density of a fluid or fluid mixture was described in terms of scaling coefficients specific to the mixture and scaling densities such that

$$\hat{\rho} = \frac{1 + \varphi_1 + b_2\varphi_2}{1 - a_3\varphi_1 - b_3\varphi_2}, \tag{5.2.1}$$

where $\hat{\rho} = \rho / \rho_c$. In order to calculate the density profile of a fluid, the scaling densities in Eqs. (5.2.9) and (5.2.13) developed earlier in Section 6.2 (and related equations) can also be applied.

6.3.1 Application to Water

Pure water is an example of a fairly symmetric one-component fluid. It does display some asymmetry, evidenced by the size of the scaling coefficients in Table 6.1; however, these coefficients are still relatively small and have only a small effect. By applying the data in Table 6.1 to the density expression (Eq.(5.2.1)), along with the scaling densities in Eqs. (5.2.9) and (5.2.13) to model the behavior of water, we obtain the density profile for $\Delta\hat{T} = -10^{-2}$, shown in Fig. 6.3. In this figure, we can see that the profile is nearly symmetric, as the profile for water (solid blue line) overlaps the symmetric profile (dashed red line).

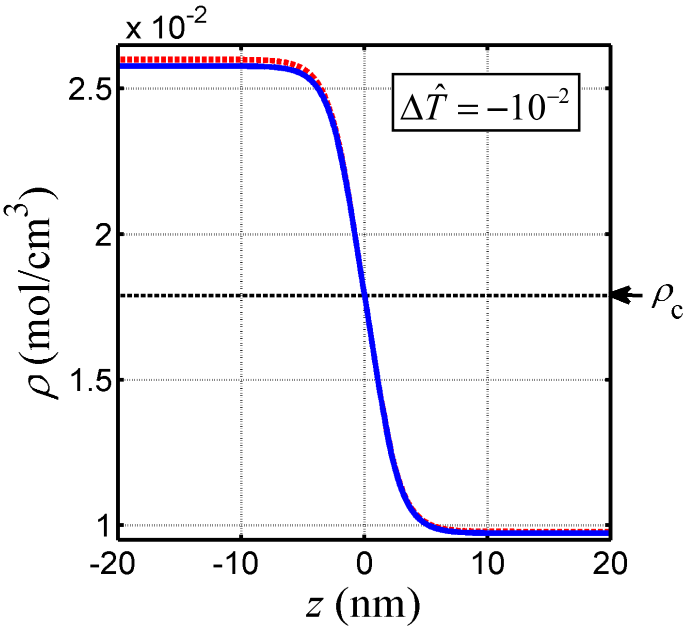

Figure 6.3. Density profile for pure water at a temperature distance of $\Delta\hat{T} = -10^{-2}$, plotted with respect to height (z-coordinate). Eqs. (5.2.1), (5.2.9), and (5.2.13), and experimental data from Table 6.1 were used to model the behavior of the density profile. The symmetric profile is indicated by the red dashed line.

Table 6.1. Experimental data for pure water

Variable	Value	Author
a_3	0.0618	Wang and Anisimov[a]
b_2	-0.0482	Wang and Anisimov[a]
A_0^-	13.95	Wang and Anisimov[a]
B_0	2.035	Wang and Anisimov[a]
$\hat{B}_0 \equiv B_0/(1+a_3)$	1.9165	(this work)
$\hat{B}_{\mathrm{cr}} \equiv B_{\mathrm{cr}}/k_{\mathrm{B}}$	5.653	Wang and Anisimov[a]
ρ_{c} (mol/cm^3)	1.79×10^{-2}	Levelt Sengers *et al.*[b]
T_{c} (K)	647	Levelt Sengers *et al.*[b]
ξ_0^- (Å)	0.694	Bonetti and Calmettes[c]

[a] Reference 68
[b] Reference 111
[c] Reference 112

Table 6.2. Experimental data for ethane

Variable	Value	Author
a_3	0.0014	Wang and Anisimov[a]
b_2	-0.0603	Wang and Anisimov[a]
A_0^-	11.79	Wang and Anisimov[a]
B_0	1.649	Wang and Anisimov[a]
$\hat{B}_{\mathrm{cr}} \equiv B_{\mathrm{cr}}/k_{\mathrm{B}}$	6.856	Wang and Anisimov[a]
ρ_{c} (mol/cm^3)	6.75×10^{-3}	Harmin and Thodos[b]
T_{c} (K)	305.3	Ambrose and Tsonopoulos[c]
ξ_0^- (Å)	0.787	Bruice[d]*

[a] Reference 68
[b] Reference 113
[c] Reference 114
[d] Reference 115

*Correlation length ($\xi_0^+ \cong 1.54$) was approximated using CH_3-CH_3 bond length.

6.3.2 Application to Ethane

Another example of a profile that displays little asymmetry is that of pure ethane. For this particular fluid, the scaling coefficients a_3 and b_2, given in Table 6.2, are very small, which indicate there is a small amount fluid asymmetry. The density profile for ethane from Eqs. (5.2.1), (5.2.9) and (5.2.13) for a temperature distance $\Delta\hat{T} = -10^{-2}$ is illustrated in Fig. 6.4. As expected, the profile of pure ethane (solid blue line) mostly overlaps the symmetric profile, given by the red dashed line.

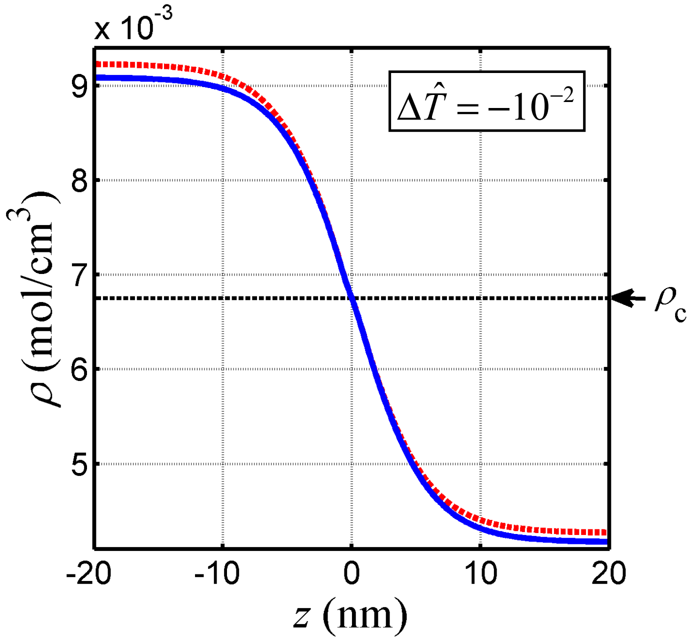

Figure 6.4. Density profile for ethane at a temperature distance of $\Delta\hat{T} = -10^{-2}$, plotted with respect to height (z-coordinate). Eqs. (5.2.1), (5.2.9) and (5.2.13), and experimental data from Table 6.6 were used to model the behavior of the density profile. The symmetric profile is given by the dashed red line

6.3.3 Application to *n*-Heptane

The final example of the density profile for a one-component fluid is that of *n*-heptane. The scaling coefficients a_3 and b_2 for *n*-heptane (given in Table 6.7) are much larger than the coefficients in pure water and ethane, so the expectation is that this density profile would exhibit greater asymmetry. As before, Eqs. (5.2.1), (5.2.9) and (5.2.13) were used to model the density profile for *n*-heptane, given the data in Table 6.3; this profile can be seen in Fig. 6.5.

Table 6.3. Experimental data for *n*-heptane

Variable	Value	Author
a_3	0.369	Wang and Anisimov[a]
b_2	0.0941	Wang and Anisimov[a]
A_0^-	22.61	Wang and Anisimov[a]
B_0	1.843	Wang and Anisimov[a]
$\hat{B}_{\mathrm{cr}} \equiv B_{\mathrm{cr}} / k_{\mathrm{B}}$	18.04	Wang and Anisimov[a]
ρ_{c} (mol/cm^3)	2.35×10^{-3}	Bradford and Thodos[b]
T_{c} (K)	540.6	Bradford and Thodos[b]
ξ_0^- (Å)	0.787	Bruice[c]*

[a] Reference 68
[b] Reference 116
[c] Reference 115
* Correlation length ($\xi_0^+ \cong 1.54$) for *n*-heptane was approximated using the bond length for CH$_3$-CH$_3$.

As illustrated in this figure, the large scaling coefficients for *n*-hexane—with the largest contribution from a_3—lead to a highly asymmetric density profile. Here we can see that at the temperature distance $\Delta\hat{T} = -10^{-2}$, the fluid prefers the liquid phase ($-z$) over the vapor phase ($+z$), as the density difference between the bulk liquid ($z << 1$) and critical densities is much greater than the density difference between the bulk vapor ($z >> 1$) and critical densities. This can also be seen by comparing the n-heptane density profile (blue line) to the symmetric profile (red dashed line) in Fig. 6.5.

Understanding the nature of the asymmetry and effect of the scaling coefficients in these one-component fluids will provide insight into the behavior of binary mixtures as well. These fluids, and the approximation of their scaling coefficients, will be discussed in later sections.

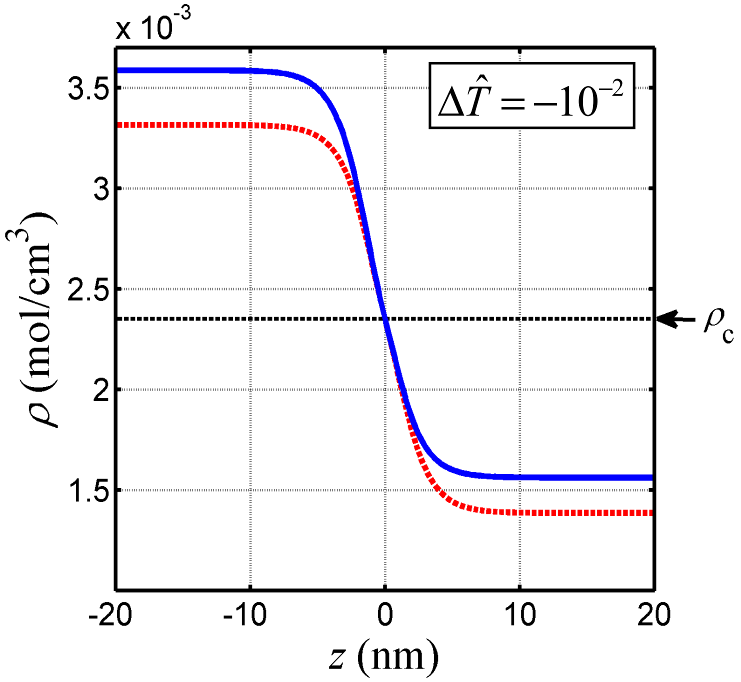

Figure 6.5. Density profile for n-heptane at a temperature distance of $\Delta\hat{T} = -10^{-2}$, plotted with respect to height (z-coordinate). Eqs. (5.2.1), (5.2.9) and (5.2.13), and experimental data from Table 6.7 were used to model the behavior of the density profile. The red dashed line indicates the symmetric profile.

6.4 Fisher Renormalization: Temperature Correction for Concentration

We have approximated key expressions for the scaling densities for one-component fluids and fluid mixtures as well as density profiles for one-component fluids, but it is also important to maintain accuracy by applying the appropriate temperature scale, as temperature can be affected by concentration. It is well-known that the critical temperature of a mixture is dependent on the concentration of each of its components. This difference in temperature also depends on the similarity or dissimilarity between the properties of each component in the mixture. Even the addition of a small amount of a disparate component to a one-component fluid can cause a dramatic difference in its critical temperature.

One of the points of focus within this work is to determine the concentration and density profiles for dilute binary solutions and to determine the profiles' dependence on concentration. As theoretical scales maintain chemical potential at a constant value, a correction, known as Fisher Renormalization[117] must be applied to account for this difference of concentration (as opposed to chemical potential) at certain temperature distances. Similar to earlier notation and definitions, the experimental and theoretical temperature differences are defined as

$$\Delta\hat{T}(x) \equiv \frac{T - T_{\mathrm{c}}(x = x_{\mathrm{c}})}{T_{\mathrm{c}}(x = x_{\mathrm{c}})} \qquad \text{and} \qquad \Delta\hat{T}(\mu) \equiv \frac{T - T_{\mathrm{c}}(\mu = \mu_{\mathrm{c}})}{T_{\mathrm{c}}(\mu = \mu_{\mathrm{c}})}, \tag{5.4.1}$$

respectively.

The actual—or experimental—temperature difference can be applied to complete scaling by converting it to scaling space, which observes a constant chemical potential (μ). Anisimov *et al.*[118] determined the actual temperature difference, $\Delta\hat{T}(x)$, can be converted to the theoretical temperature difference, $\Delta\hat{T}(\mu)$, by the relation:

$$\Delta\hat{T}(x) = \left[\Delta\hat{T}(\mu)\right]^{1-\alpha} \tau_2^{\alpha} + \Delta\hat{T}(\mu), \tag{5.4.2}$$

where the characteristic temperature,

$$\tau_2 = \left[A_0^- x_c (1 - x_c) T_c^{-2} \left(\frac{dT_c}{dx} \right)^2 \right]^{1/\alpha} . \tag{5.4.3}$$

Based on the relation in Eq. (5.4.2), it can be seen that there is a significant difference between the experimental and theoretical temperature distances to the critical point where $\Delta T(x) \sim \tau_2$. It is possible to approximate this expression by comparing the relative magnitude of the terms by means of the characteristic temperature τ_2 (e.g. if $\Delta \hat{T}(x) >> \tau_2$ or $\Delta \hat{T}(x) << \tau_2$). However, at temperatures very close to the critical point, there may not be a large difference between these terms, and the full expression should be used for the best accuracy. This solution to this nonlinear equation was approximated using the 'fsolve' function within the MATLAB optimization toolbox.

An example of this difference between experimental and theoretical temperatures is presented by applying the experimental data for a dilute aqueous mixture of *n*-hexane given in Table 6.4 for an *n*-hexane concentration of $x = 0.015$. The value of A_0^- for pure water is used to approximate the behavior of this solution, given in Table 6.4, as we are considering a dilute solution of water and *n*-hexane.

Table 6.4. Selected experimental data for a dilute aqueous *n*-hexane solution

Variable	Value	Author
A_0^- (pure water)	13.95	Wang and Anisimov[a]
T_c ($x_{n\text{-hexane}} = 0.015$)	641.600 K	De Loos *et al.*[b]
$dT_c(x)/dx$ (dilute aq. *n*-hexane solution)	-352.69 K	Abdulagatov[c]

[a] Reference 68
[b] Reference 119
[c] Reference 120

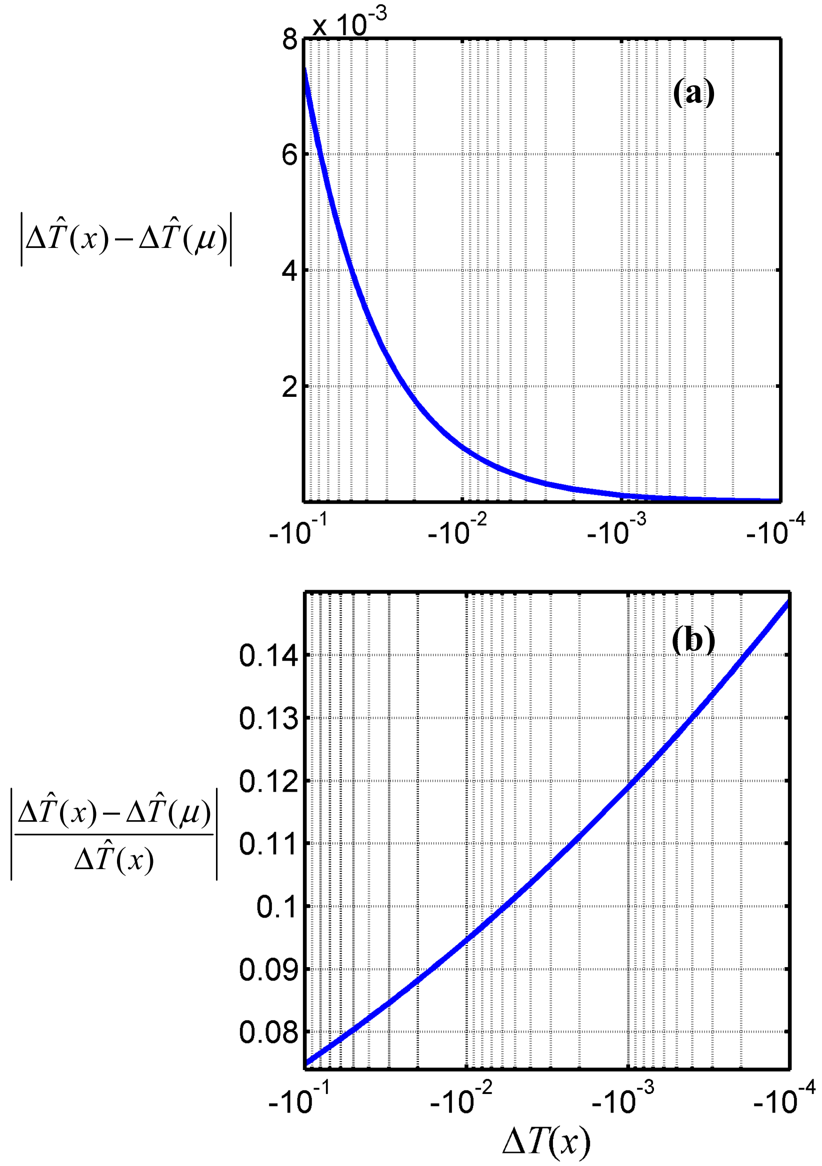

Figure 6.6. Plots of the difference (a) and normalized difference (b) between experimental ($\Delta T(x)$) and theoretical ($\Delta T(\mu)$) temperature distances as predicted by Eq. (5.4.2) and data in Table 6.4 for a dilute aqueous *n*-hexane solution where $x_c = 0.015$.

For the example of a dilute aqueous *n*-hexane solution, where for most temperature distances at dilute concentrations $\tau_2 / \Delta T(x) << 1$, the second term in Eq. (5.4.2) is the main contributing factor and $\Delta T(x) \cong \Delta T(\mu)$. However, both terms in this equation must be taken into consideration very close to the critical point, where $\tau_2 / \Delta T(x) \geq 1$. At first glance, it appears that the error decreases as the critical point is approached for this dilute aqueous *n*-hexane solution, shown in Fig. 6.6 (a). However, further analysis shown in Fig. 6.6 (b) shows otherwise; this error relative to the experimental temperature distance to the critical point becomes larger near the critical point. This error is nearly 15% when $\Delta T(x) = -10^{-4}$. Since the characteristic temperature, τ_2, (Eq. (5.4.3)) is dependent on the concentration of the solution and its temperature derivative, the error could be larger or smaller for other solutions. For example, a solution with a steep critical temperature derivative with respect to concentration would exhibit a larger correction factor. As a result, when complete scaling is used for calculations very close to the critical point, it is crucial to determine the contribution of both terms in Eq. (5.4.2) for each solution of interest for the highest accuracy. For the analyses contained in this work, both terms in the temperature correction will be used for the best accuracy at temperatures very close to the critical point.

6.5 Modeling Concentration Profiles for Dilute Binary Solutions

As complete scaling has been successfully utilized to determine density profiles for one-component fluids, this method will also be used to model concentration profiles for dilute binary mixtures. In addition, since the order parameter and thermal density (φ_1 and φ_2, respectively) for a dilute mixture have been established in terms of complete scaling in Section 6.2, we can apply the affects of asymmetry—either inherent in the one-component fluid or due to the mixture—to model real mixtures. In Section 3.2, the concentration of solute in terms of scaling fields and densities can be expressed as[47]

$$x = \frac{x_\mathrm{c} + a_4\varphi_1 + b_4\varphi_2}{1 + \varphi_1 + b_2\varphi_2} \tag{5.5.1}$$

where x_c is the critical composition of the mixture. The remaining unknowns are the scaling coefficients, a_4, b_2 and b_4, which are specific to the mixture of interest.

As discussed in Section 3.2, the expressions for the ordering and thermal fields of a mixture are

$$h_1 = \Delta\hat{\mu}_1 + a_2\Delta\hat{T} + a_3\Delta\hat{P} + a_4\Delta\hat{\mu}_{21} \tag{5.5.2}$$

and

$$h_2 = \Delta\hat{T} + b_2\Delta\hat{\mu}_1 + b_3\Delta\hat{P} + b_4\Delta\hat{\mu}_{21} \tag{5.5.3}$$

respectively. Since the scaling coefficients a_4 and b_4 are coupled with the exchange chemical potential, $\Delta\hat{\mu}_{21}$, they represent the majority of the effect of asymmetry as a result of the mixture. These scaling coefficients, as derived in Section 3.2, can be written in terms of the other scaling coefficients and physical fields as:

$$a_4 \cong -x_\mathrm{c}\left[\left(1 + a_3\right)\hat{K} - 1\right] \tag{5.5.4}$$

and

$$b_4 \cong -x_\mathrm{c}\left[\frac{d\hat{T}_\mathrm{c}}{dx} + b_2\left(\hat{K} - 1 + \frac{d\hat{P}_\mathrm{c}}{dx}\right)\right]. \quad (\text{for } b_2 = b_3) \tag{5.5.5}$$

In these equations, the dimensionless Krichevskii parameter, $\hat{K}$, is defined as

$$\hat{K} \equiv \frac{K}{\rho_\mathrm{c} k_\mathrm{B} T_\mathrm{c}} = \frac{1}{\rho_\mathrm{c} k_\mathrm{B} T_\mathrm{c}}\left[\frac{dP_\mathrm{c}}{dx} - \left(\frac{\partial P}{\partial T}\right)_{h_1 = 0,\mathrm{c}} \frac{dT_\mathrm{c}}{dx}\right]. \tag{5.5.6}$$

In Eqs. (5.5.4) and (5.5.5), the Krichevskii parameter applies the physical characteristics of the mixture and its associated asymmetry to adjust the one-component fluid (solvent) coefficients, a_3 and b_2, to values that more accurately represent the asymmetry of the mixture.

The remaining scaling coefficient, b_2, is coupled with the chemical potential of the one-component substance ($\hat{\mu}_1$), or solvent, as shown in Eq. (5.5.3). It can be safely assumed that there is little, if any, influence on the coefficient b_2 by the addition of a small amount of solute. If it is believed that there is a very large effect of asymmetry on the coefficient b_2, Eq. (2.2.54) in Section 3.2 can be used to approximate this difference; however, this difference is expected to be very minor. Therefore, we will assume that b_2 for the dilute mixture is equivalent to the value of b_2 for the pure solvent.

6.5.1 Application to Dilute Aqueous *n*-Hexane Solutions

By applying experimental data related to the fluid mixture, these expressions for the scaling coefficients of the mixture can be used to approximate the behavior of real dilute solutions. Mixtures of particular interest are those that exhibit a high degree of asymmetry with only the smallest addition of solute: where the solute has a strong affinity for either the liquid or vapor phase of the solvent. For the analysis in this section, we will focus on a dilute aqueous *n*-hexane solution using the experimental data provided in Tables 6.1, 6.5 and 6.6.

Table 6.5. Experimental data for dilute aqueous *n*-hexane solutions

Variable	Value	Author
$\frac{dT_c}{dx}$	-352.69 K	Abdulagatov[a]
$\frac{dP_c}{dx}$	83.573 MPa	Abdulagatov[a]
K	178.2 MPa	Abdulagatov[a]

[a] Reference 120

Table 6.6. Critical temperatures of dilute aqueous *n*-hexane solutions at various concentrations

Concentration of *n*-hexane (mole fraction)	T_c (K)	Author
0.000	647.096	De Loos *et al.*[a]
0.004	645	Yiling and Michelberger[b]
0.015	641.600	De Loos *et al.*[a]
0.025	636.500	De Loos *et al.*[a]

[a] Reference 119
[b] Reference 121

Before proceeding further, it is important to study the critical behavior of a fluid mixture of interest at varying concentrations. Since we are applying a linear approximation of physical fields to this model, we should only consider those concentrations with critical temperatures near where the critical locus exhibits a linear trend. A graphical representation of this concept can be seen in the plot of the critical locus in Fig. 6.7. In the case of dilute aqueous *n*-hexane, we should only consider critical concentrations with critical temperatures that are linear in trend (indicated by the red dashed line in the figure inset), and therefore close to the critical point of pure water. For this dilute mixture, the critical behavior of the mixture is approximately linear within the critical temperature range of 635 - 646.7 K, and will be our area of focus.

It should be noted that a linear approximation may not be appropriate for all fluid mixtures. A linear approximation cannot be used for such mixtures exhibiting closed solubility loops,[122] as they posses both an upper and lower critical solution temperature, with some even exhibiting double critical points.

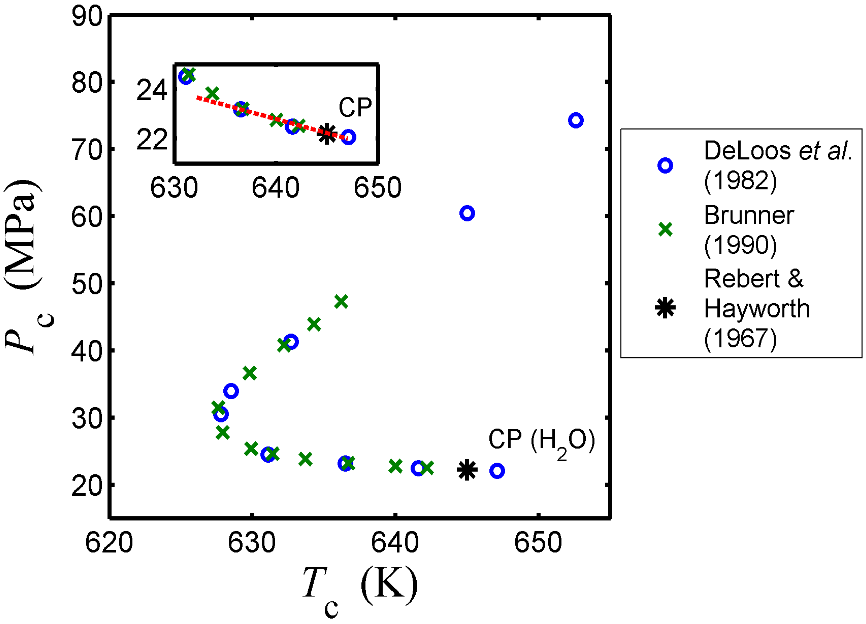

Figure 6.7. Critical locus for aqueous *n*-hexane solutions. CP indicates the critical point of pure water. Data plotted here is from De Loos *et al.*,[119] Brunner,[123] and Rebert and Hayworth.[124]

6.5.2 Application to Dilute *n*-Heptane-Ethane Solutions

An example of a mixture of two components with differing molecular volumes is an ethane-*n*-heptane solution. The critical locus for a binary mixture of ethane with a low concentration of *n*-heptane can be seen in Fig. 6.8. As before, we are applying a linear approximation of physical fields in this model, so only those concentrations with critical temperatures within the range where the critical locus exhibits a linear trend should be used. This linear area of the data is indicated by the dashed red line in Fig. 6.8, which originates at the critical point of ethane and includes the experimental data found by Singh *et al.*[125]

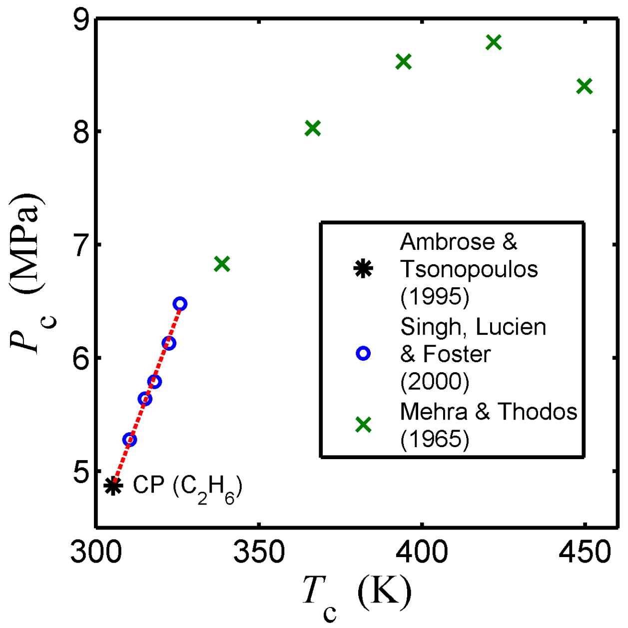

Figure 6.8. Critical locus for a mixture of ethane and *n*-heptane. CP indicates the critical point of ethane. Data plotted here is from Ambrose and Tsonopoulos,[114] Singh, Lucien and Foster,[125] and Mehra and Thodos.[126]

Table 6.7. Critical temperatures of dilute *n*-hepane-ethane solutions at various concentrations

Concentration of *n*-heptane in ethane (mole fraction)	T_c (K)	P_c (MPa)	Author(s)
0.000	305.3	4.87	Ambrose and Tsonopoulos[a]
0.0087	310.4	5.28	Singh *et al.*[b]
0.0151	315.0	5.64	Singh *et al.*[b]
0.0202	318.0	5.79	Singh *et al.*[b]
0.0287	322.4	6.13	Singh *et al.*[b]
0.0350	325.8	6.48	Singh *et al.*[b]

[a] Reference 114

[b] Reference 125

Table 6.8. Experimental data for dilute *n*-heptane-ethane solutions

Variable	Value	Author(s)
$\frac{dT_c}{dx}$	588.9 K	Ambrose and Tsonopoulos, Singh *et al.*[a]*
$\frac{dP_c}{dx}$	44.8 MPa	Ambrose and Tsonopoulos, Singh *et al.*[a]*
K	-15.0 MPa	Abdulagatov[b]

[a] Reference 114

[b] Reference 120

* Initial slopes determined by linear approximation for dilute concentrations from data in these references

Experimental data from dilute *n*-heptane-ethane solutions with concentrations corresponding to critical temperatures within this linear region are provided in Table

6.7. Approximations of initial slopes based on this data along with the Krichevskii parameter for dilute solutions are in Table 6.8.

6.5.3 Effect of Temperature on Profile Asymmetry

Now that the physical parameters of this model have been set for a dilute two dilute solutions, we can develop concentration profiles and examine the properties that affect asymmetry. First, an average concentration is chosen to illustrate the effect of temperature on the asymmetry of a mixture, or how greatly the solute favors one phase over another.

The concentration profiles for a dilute aqueous *n*-hexane solution with a critical (and average) concentration of $x_\mathrm{c} = \langle x \rangle = 0.015$ and $T_\mathrm{c} = 641.6\ \mathrm{K}$ (from Table 6.6) for solution temperatures near the critical point of separation can be seen in Fig. 6.9. For this model and analysis, the expression for concentration in Eq. (5.5.1) was used. Equations (5.2.9) and (5.2.13) were used for the order parameter and thermal scaling density, respectively. The scaling coefficients were either taken directly from Table 6.1 for pure water or determined from Eqs. (5.5.4) and (5.5.5) by applying data in Tables 6.5 and 6.6 for the mixture. Lastly, as the effect of concentration is being considered, Fisher Renormalization—or theoretical temperature correction—in Eq. (5.4.2) was also applied to this model for increased accuracy.

Identical to the process for modeling the effect of temperature on concentration profiles for a dilute aqueous solution of *n*-hexane, profiles for a dilute solution of *n*-heptane in ethane were developed. The concentration profiles with a critical (and average) concentration of $x_c = \langle x \rangle = 0.0202$ and $T_c = 318$ K (from Table 6.7) for solution temperatures near the critical point of separation can be seen in Fig. 6.10. The same expressions (Eqs. (5.5.1), (5.2.9), (5.2.13), (5.5.4) and (5.5.5)) were used in conjunction with the data in Tables 6.7 and 6.8 for the dilute *n*-heptane-ethane mixture. The value of the scaling coefficients for pure ethane were taken from Table 6.2. As before, Fisher renormalization in Eq. (5.4.2) was applied for increased accuracy.

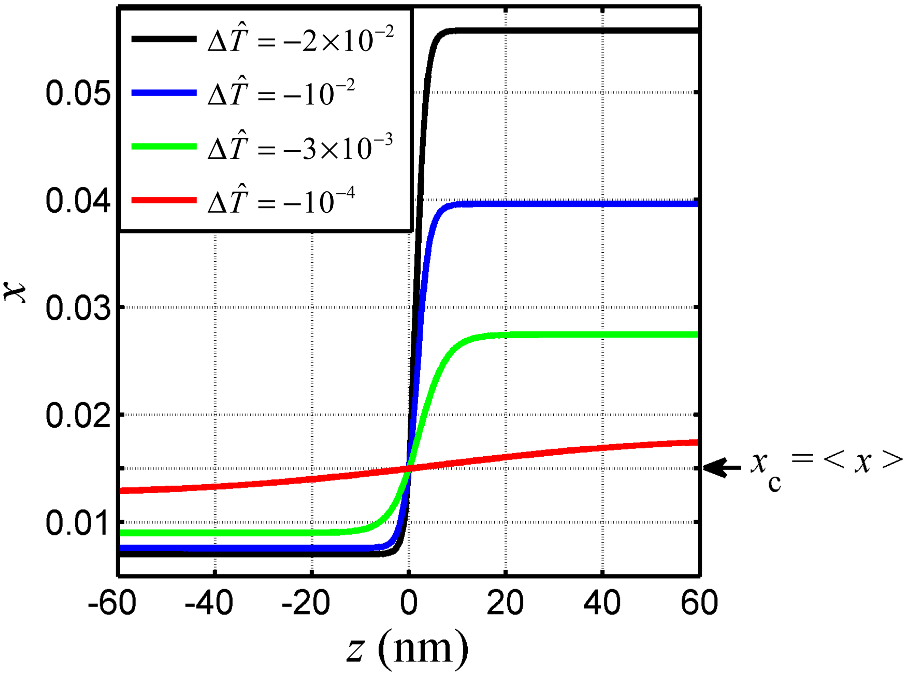

Figure 6.9. Concentration profiles for *n*-hexane in water at the vapor-liquid interface, at a critical and average concentration of $x_c = \langle x \rangle = 0.015$, and at various temperatures, plotted with respect to height (*z*-coordinate). Eqs. (5.5.1), (5.2.9), (5.2.13), (5.5.4), (5.5.5) and (5.4.2), and experimental data from Tables 6.1, 6.5 and 6.6 were used to model the behavior of the mixture.

As expected, the closer the mixture is to the critical point, the phase coexistence becomes more symmetric and the mixture exhibits less asymmetry. At a temperature distance of $\Delta\hat{T} = -10^{-4}$, near the critical point of the mixture, the concentration profile is symmetric, as shown by the red line in Figures 6.9 and 6.10. This indicates that near the critical point, the *n*-hexane distributes itself more equally between liquid (- z) and vapor (+ z) phases of water (Fig. 6.9). A similar result for the distribution of *n*-heptane in the two phases of ethane is seen in the red line in Fig. 6.10.

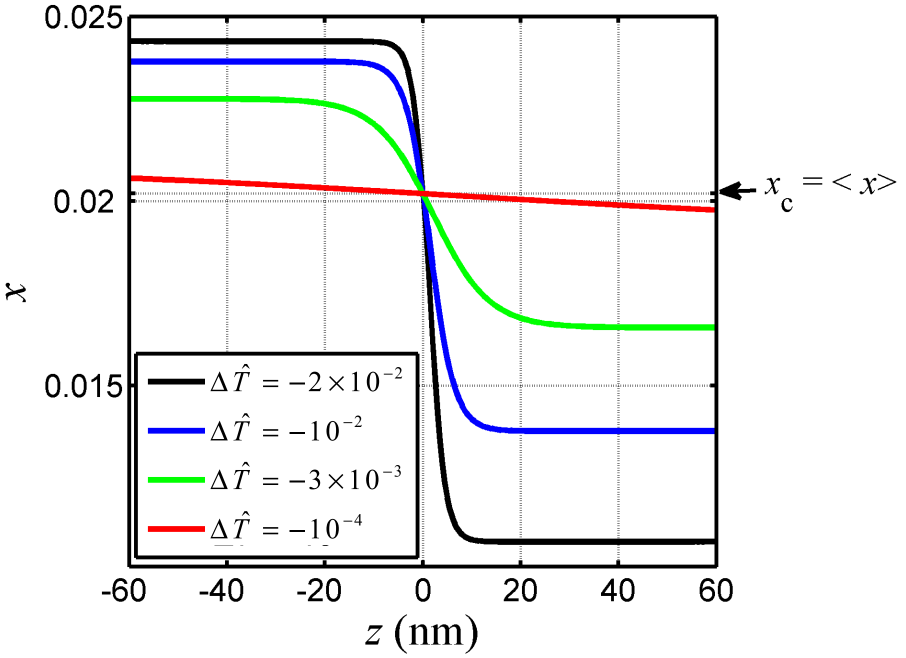

Figure 6.10. Concentration profiles for *n*-hepane in ethane at the vapor-liquid interface, at a critical and average concentration of $x_c = \langle x \rangle = 0.0202$, and at various temperature distances, plotted with respect to height (*z*-coordinate). Eqs. (5.5.1), (5.2.9), (5.2.13), (5.5.4), (5.5.5) and (5.4.2), and experimental data from Tables 6.2, 6.7 and 6.8 were used to model the behavior of the mixture.

Conversely, the further from the critical point the mixture is, the more asymmetric the profile becomes. At a temperature distance of $\Delta\hat{T} = -2\times10^{-2}$ (shown by the black line in Fig. 6.9), the aqueous *n*-hexane solution separates into an *n*-hexane-rich vapor (+ z) phase and an *n*-hexane-poor liquid (- z) phase. Since $z = 0$

establishes the center of the symmetric profile, it can be seen that *n*-hexane clearly has a preference for the vapor phase as the higher concentrations lie in the positive *z*-direction.

An increase in asymmetry farther from the critical point is also observed in the dilute *n*-heptane-ethane mixture. At a temperature distance of $\Delta\hat{T} = -2\times10^{-2}$, shown by the black line in Fig. 6.10, *n*-heptane has a greater preference for the liquid ($-z$) phase, which is expected given the larger molecular size of *n*-heptane relative to ethane.

Lastly, the profiles in Figures 6.9 and 6.10—even even at varying temperatures—all intersect at the critical (and average) concentration of the mixture and at $z = 0$, the center of the symmetric concentration profile. This validates the form of the thermal scaling density used, which includes the correction of the height dependence of the entropy, discussed in Section 6.2.

6.5.4 Effect of Concentration on Profile Asymmetry

Second, to illustrate the effect of concentration on asymmetry in a dilute mixture, a temperature distance to the critical point, $\Delta\hat{T}$, will be held constant and the average/critical concentration will be varied. The equations used for this model and analysis are identical to those listed in the previous subsection.

The concentration profiles for dilute aqueous *n*-hexane solutions of $x_\mathrm{c} = \langle x \rangle = 0.004$, 0.015 and 0.025 at a constant temperature distance $\Delta\hat{T} = -10^{-2}$ can be seen in Fig. 6.11. The critical temperatures used and correlated to these concentrations of *n*-hexane in water are found in Table 6.6. The concentration profiles for dilute *n*-heptane-ethane solutions of $x_c = \langle x \rangle = 0.0087$, 0.0151 and 0.0287 at the same constant temperature distance $\Delta\hat{T} = -10^{-2}$ are illustrated in Fig. 6.12. The critical temperatures used and correlated to these concentrations of *n*-hexane in water are found in Table 6.7. The dashed colored lines in both Figures 6.11 and 6.12 correspond to the value of the average concentration for each profile specific to a given x_c and are provided to assist in highlighting any asymmetry. The methodologies, equations and experimental values used to model this solution's behavior are the same as those used and described in Section 6.5.2.

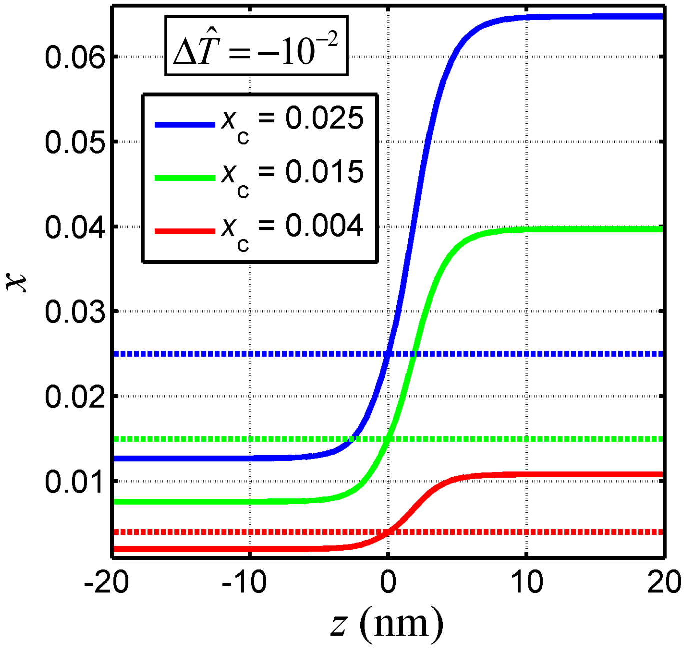

Figure 6.11. Concentration profiles for *n*-hexane in water at the vapor-liquid interface, at a constant temperature distance $\Delta\hat{T} = -10^{-2}$, and at various critical or average concentrations, plotted with respect to height (*z*-coordinate). The dashed lines indicate the average concentration with the color corresponding to each of the critical concentrations shown. Eqs. (5.5.1), (5.2.9), (5.2.13), (5.5.4), (5.5.5) and (5.4.2), and experimental data from Tables 6.1, 6.5 and 6.6 were used to model the behavior of the mixture.

Based on these figures, it appears that there is increased fluid asymmetry with an increase in concentration for both the dilute aqueous *n*-hexane and *n*-hepthane-ethane solutions. Further analysis of both solutions showed that asymmetry did increase slightly with an increase in concentration in both solutions. In the aqueous *n*-hexane solution, ratios of the bulk liquid ($z \ll 1$) phase relative to the average concentration (x_c) yielded relatively constant values for each concentration at a constant temperature, shown in Table 6.9. However, in the bulk vapor phase ($z \gg 1$), the increased concentration of *n*-hexane resulted in relatively larger differences in fluid asymmetry.

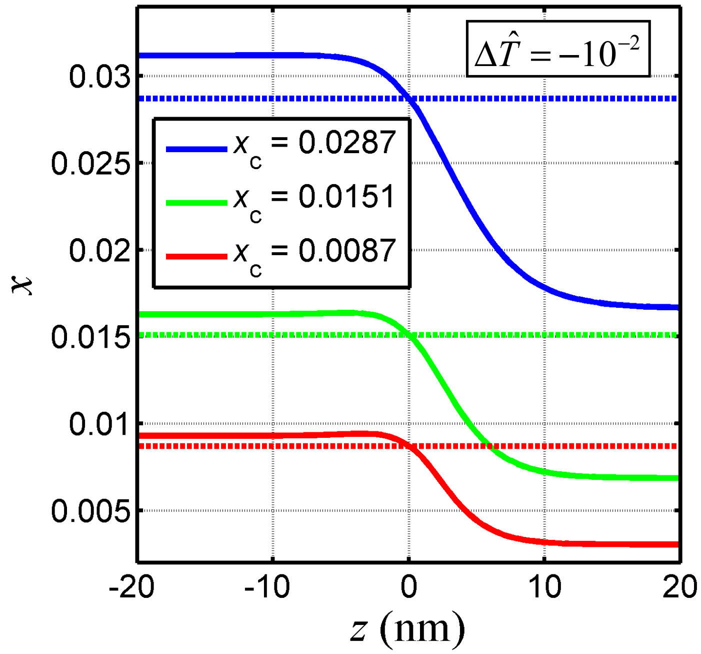

Figure 6.12. Concentration profiles for *n*-hepane in ethane at the vapor-liquid interface, at a constant temperature distance $\Delta\hat{T} = -10^{-2}$, and at various critical or average concentrations, plotted with respect to height (*z*-coordinate). The dashed lines indicate the average concentration with the color corresponding to each of the critical concentrations shown. Eqs. (5.5.1), (5.2.9), (5.2.13), (5.5.4), (5.5.5) and (5.4.2), and experimental data from Tables 6.2, 6.7 and 6.8 were used to model the behavior of the mixture.

Similar results were observed in the dilute *n*-heptane-ethane solutions, given in Table 6.10. Higher asymmetry was observed with increased concentration and temperature distance from the critical point in the bulk vapor phase ($z \gg 1$) relative to the average concentration. Concentration ratios in the bulk liquid phase relative to the average concentration were somewhat constant, with the exception of the temperature distance $\Delta\hat{T} = -10^{-2}$, where greater asymmetry was present with a change in concentration.

Table 6.9. Comparison of bulk phase concentration data from dilute aqueous *n*-hexane solutions at various temperatures.

$\Delta\hat{T}$	x_c	x_{liq}	x_{vap}	x_c / x_{liq}	x_{vap} / x_c
-10^{-2}	4.00×10^{-3}	2.02×10^{-3}	1.08×10^{-2}	1.98	2.70
	1.50×10^{-2}	7.60×10^{-3}	3.97×10^{-2}	1.97	2.64
	2.50×10^{-2}	1.27×10^{-2}	6.47×10^{-2}	1.97	2.59
-10^{-3}	4.00×10^{-3}	2.75×10^{-3}	6.06×10^{-3}	1.45	1.52
	1.50×10^{-2}	1.04×10^{-2}	2.25×10^{-2}	1.44	1.50
	2.50×10^{-2}	1.74×10^{-2}	3.71×10^{-2}	1.44	1.48
-10^{-4}	4.00×10^{-3}	3.33×10^{-3}	4.83×10^{-3}	1.20	1.21
	1.50×10^{-2}	1.26×10^{-2}	1.80×10^{-2}	1.19	1.20
	2.50×10^{-2}	2.10×10^{-2}	2.98×10^{-2}	1.19	1.19

Based on the results presented here, a change in concentration has a larger impact on the asymmetry in the vapor phase. However, the greatest impact on the asymmetry of concentration profiles of dilute mixtures is a temperature distance farther from the critical point coupled with the addition of a solute. Since the analyses in this work only address dilute solutions, it is possible that higher concentrations of a dissimilar component—perhaps at concentrations closer to saturation—could yield results that indicate a change in concentration alone has a greater effect on the fluid asymmetry of a mixture.

Table 6.10. Comparison of bulk phase concentration data from dilute *n*-heptane-ethane solutions at various temperatures.

$\Delta\hat{T}$	x_c	x_{liq}	x_{vap}	x_c / x_{liq}	x_{vap} / x_c
-10^{-2}	8.70×10^{-3}	9.29×10^{-3}	3.04×10^{-3}	0.936	0.349
	1.51×10^{-2}	1.63×10^{-2}	6.86×10^{-3}	0.926	0.454
	2.87×10^{-2}	3.12×10^{-2}	1.66×10^{-2}	0.920	0.578
-10^{-3}	8.70×10^{-3}	9.51×10^{-3}	6.86×10^{-3}	0.915	0.789
	1.51×10^{-2}	1.65×10^{-2}	1.20×10^{-2}	0.915	0.795
	2.87×10^{-2}	3.13×10^{-2}	2.29×10^{-2}	0.917	0.798
-10^{-4}	8.70×10^{-3}	9.20×10^{-3}	8.03×10^{-3}	0.946	0.923
	1.51×10^{-2}	1.59×10^{-2}	1.40×10^{-2}	0.950	0.927
	2.87×10^{-2}	3.03×10^{-2}	2.66×10^{-2}	0.947	0.927

6.6 Modeling Asymmetric Density Profiles for Dilute Binary Solutions

Another behavior of interest is the change in the density profile of a one-component fluid due to the addition of a small amount of solute. It is well-known that if solute with a vastly different molecular volume is added to a solvent, the density of the mixture is significantly altered. Since complete scaling has successfully been applied to model the behavior of density in one-component fluids and concentration in dilute mixtures, this method will also be used to model the density profiles of dilute binary mixtures, taking into account the effect of the concentration of solute or impurity added.

6.6.1 Application to Dilute Polystyrene-Cyclohexane Solutions

An example of a binary solution with components with vastly different molecular volumes is a dilute polymer solution. In particular, we can focus on a solution of polystyrene in cyclohexane. Given the expression for density in Eq. (5.2.1), we can provide an analogous expression for the density profile in terms of volume fraction of polymer, ϕ:

$$\hat{\phi} = \frac{1 + \varphi_1 + b_2\varphi_2}{1 - a_3\varphi_1 - b_3\varphi_2}, \tag{5.6.1}$$

where $\hat{\phi} \equiv \phi / \phi_c$. Since the expressions for the order parameter (φ_1) and thermal scaling density (φ_2) in Eqs. (5.2.9) and (5.2.13) can be used for one-component fluids or fluid mixtures, these same expressions can also be used in this example. It should be noted that since incompressible polymer solutions are modeled as a one-component fluid where the monomers of that one-component fluid assemble to form a polymer chain, Fisher Renormalization is not required for this analysis.

Recalling from Section 5.2, the scaling coefficients a_3 and b_2 in terms of degree of polymerization, N, were determined to be

$$a_{\mathrm{eff}} = \frac{3}{5}\left(\frac{N-1}{N+\sqrt{N}}\right), \tag{5.6.2}$$

and

$$b_2 \cong a_{\mathrm{eff}} \frac{N\sqrt{N}}{N+\sqrt{N}}. \tag{5.6.3}$$

Since $a_{\mathrm{eff}} \equiv a_3 / (1 + a_3)$, the expression for a_3 can be written in terms of degree of polymerization as

$$a_3 = \frac{\frac{3}{5}\left(\frac{N-1}{N+\sqrt{N}}\right)}{1-\frac{3}{5}\left(\frac{N-1}{N+\sqrt{N}}\right)}. \tag{5.6.4}$$

However, it has also been shown in Section 5.2 that at moderate and higher degrees of polymerization ($N \geq 100$), these expressions can be simplified to

$$a_3(N \geq 100) \rightarrow \frac{3}{2} \tag{5.6.5}$$

and

$$b_2(N \geq 100) \rightarrow a_{\text{eff}}\sqrt{N}. \tag{5.6.6}$$

The expressions for the critical amplitudes developed by Anisimov *et al.*[103] and simplified in this work are:

$$\hat{B}_0(N \geq 100) \rightarrow B_{0,N=1}N^{\beta/2}, \tag{5.6.7}$$

$$A_0 \cong A_{0,N=1}N^{-(1+\alpha)/2}, \tag{5.6.8}$$

$$\xi_0 \cong r_0 N^{(1-\nu)/2}, \tag{5.6.9}$$

where $B_{0,N=1}$ and $A_{0,N=1}$ are both constants approximated as $B_{0,N=1} \cong A_{0,N=1} \cong 1$ for the three dimensional Ising model and r_0 is the size of the monomer. For polystyrene, the value[103] r_0 □ 0.15 nm.

For this concentration profile, the intent is to be somewhat close to the 'critical' region, where the Widom variable[93] $w \equiv \frac{1}{2}\sqrt{N}\left|\Delta\hat{T}\right| << 1$ (discussed in Section 5.1). A high degree of polymerization would lead to model behavior in the 'polymer' regime, where $w \equiv \frac{1}{2}\sqrt{N}\left|\Delta\hat{T}\right| >> 1$. Therefore, in this example, for the temperature distance of $\Delta\hat{T} = -10^{-2}$, the degree of polymerization chosen is only moderate, where $N = 100$ and $N = 150$. The value of the critical background ($\hat{B}_{\mathrm{cr}}$) in Eq. (5.2.13) was estimated to be zero for this specific case because this term decreases as fluctuations decrease with an increasing degree of polymerization. The concentration profile for a polystyrene-cyclohexane solution at a moderate degree of polymerization can be seen in Fig. 6.13.

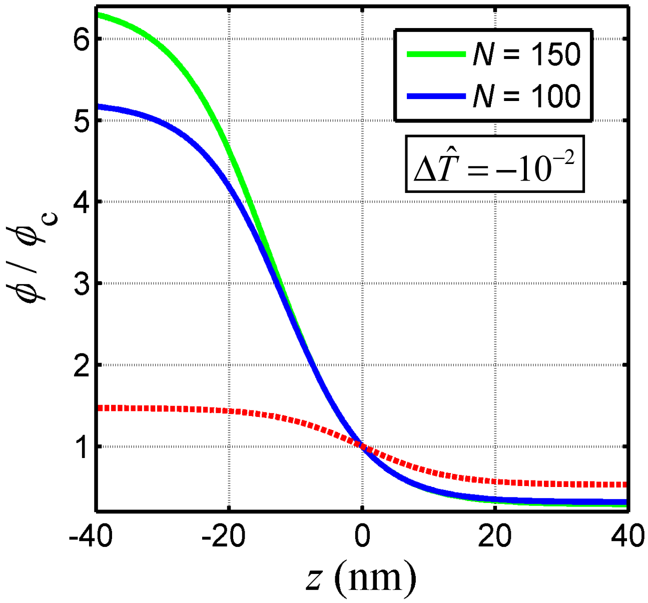

Figure 6.13. Normalized density profile for a polystyrene-cyclohexane solution with degrees of polymerization $N = 100$, $N = 150$ and at a temperature distance of $\Delta\hat{T} = -10^{2}$. Eqs. (5.6.1), (5.2.9), (5.2.13) and (5.6.5) -(5.6.9) were used to model the behavior of the mixture. The red dashed line is the normalized symmetric profile.

We can see in this figure that even near the 'critical' region at a moderate degree of polymerization, the length of the polymer chains impacts the fluid asymmetry of the density or volume fraction profile. The largest volume fraction lies in the polymer-rich phase ($-z$) and the smallest volume lies in the solvent-rich phase ($+z$).

6.6.2 Application to Dilute Ethane-*n*-Heptane Solutions

Another example of a mixture of two components with differing molecular volumes is an *n*-heptane-ethane solution. The expression in Eq. (5.2.1) can still be used to model the density profile. However, this is not a polymer solution and the scaling coefficients a_3 and b_2 must be approximated in a different manner than in Section 6.6.1.

Since the expression for the density of a mixture (Eq. (5.2.1)) does not include the scaling coefficients a_4 and b_4, which are coupled with the exchange chemical potential of the mixture in Eqs. (5.5.2) and (5.5.3), the majority of the concentration-dependent asymmetry is introduced via the coefficients a_3 and b_2. As indicated by Wang and Anisimov[64] and discussed in Section 3.2, the coefficient a_3 has shown a dependence on molecular volume. The coefficient b_2 may also be dependent on molecular volume as well, but not as significantly as a_3 (see Section 3.2). Therefore, in mixtures with components of differing molecular volumes, we will approximate the scaling coefficients a_3 and b_2 for the mixture as

$$a_3(x_\mathrm{c}) \cong a_3^0 + \frac{x_\mathrm{c}}{V_\mathrm{c}}\frac{dV_\mathrm{c}}{dx} \tag{5.6.10}$$

and

$$b_2(x_\mathrm{c}) \cong b_2^0 + k\frac{x_\mathrm{c}}{V_\mathrm{c}}\frac{dV_\mathrm{c}}{dx}, \tag{5.6.11}$$

respectively, where $k \sim 1/3$ as presented in Section 3.2.

With this approximation, the temperature correction in Eqs. (5.4.2) and (5.4.3) can be applied to this solution. It should also be noted that the normalized amplitude $\hat{B}_0$ is dependent on the scaling coefficient a_3 as presented in Section 4.2:

$$\hat{B}_0 = \frac{B_0}{1 + a_3}. \tag{5.6.12}$$

Therefore, $\hat{B}_0$ must be determined for each change in concentration, as the scaling coefficient a_3 is dependent on concentration, given in Eq. (5.6.12).

6.6.2 Effect of Temperature on Asymmetry in Density Profiles

The first property to be analyzed is the effect of temperature on the asymmetry of the density profile of a dilute *n*-heptane-ethane mixture and its behavior can be seen in Fig. 6.14. This figure represents the density profiles at a constant concentration of *n*-heptane of $x = 0.0202$ at various temperatures with the temperature correction in Eq. (5.4.2) applied. This concentration was chosen as it was near the middle of the linear region of the *n*-heptane-ethane critical locus. Experimental concentration data used for this model can be found in Table 6.7. The density profile was modeled using the expression for density in Eq. (5.2.1) and scaling densities in Eqs. (5.2.9) and (5.2.13). The correction factor used in Eqs. (5.6.10) and (5.6.11) for this *n*-heptane-ethane mixture was

$$\frac{1}{V_\mathrm{c}} \frac{dV_\mathrm{c}}{dx} \cong 6 \tag{5.6.13}$$

which was approximated by Anisimov, Gorodetskii and Shmakov[123] by a fit to experimental data. Note that this constant in Eq. (5.6.13) should have been reported as positive, as an increase in critical volume with respect to concentration of *n*-heptane leads to an increase in fluid asymmetry. This is because the critical density decreases when the concentration of solute, *n*-heptane, is increased, making dV_c / dx positive. This constant in Eq. (5.6.13) is approximated within a small range of values; therefore the maximum value was selected to model the density profiles. Lastly, the critical concentration of the mixture was given by linear approximation, which is valid for these small concentrations:

$$\rho_c \cong (1-x)\rho_{c,\,C2} + x\rho_{c,\,C7}\,, \tag{5.6.14}$$

where $\rho_{c,\,C2}$ and $\rho_{c,\,C7}$ are the critical densities of ethane and *n*-heptane, respectively given in Tables 6.2 and 6.3.

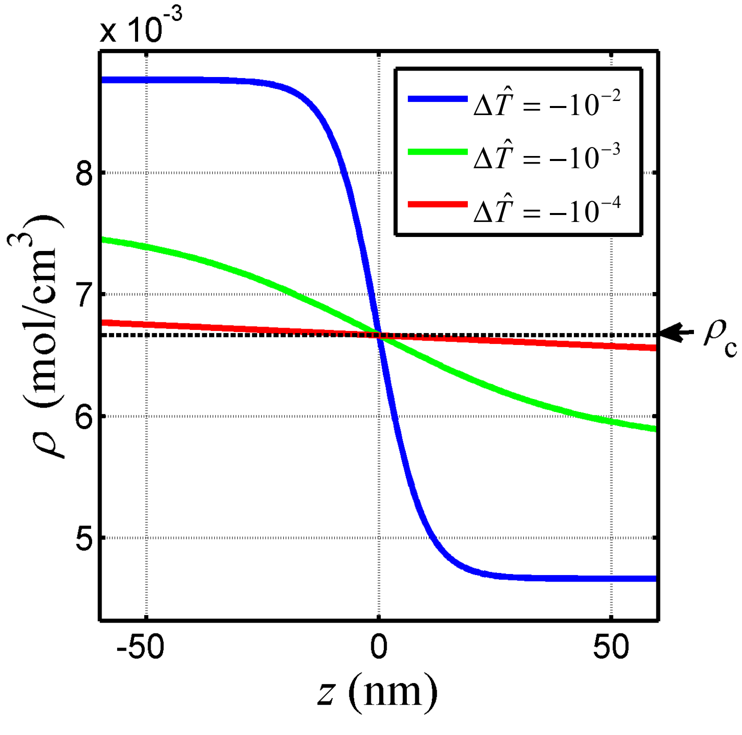

Figure 6.14. Density profiles for *n*-heptane in ethane at the vapor-liquid interface, at a critical and average concentration of $x_c = 0.0202$, and at various temperatures, plotted with respect to height (*z*-coordinate). Eqs., (5.2.1), (5.5.2), (5.5.3), (5.6.10), (5.6.11), (5.6.13) and (5.4.2) and experimental data from Tables 6.2 and 6.7 were used to model the behavior of the mixture. The critical density of an *n*-heptane-ethane mixture of $x_c = 0.0202$ is indicated by ρ_c.

As we can see in Fig. 6.14, temperature distance from the critical point does not appear to impact the asymmetry of the density profile for a mixture of ethane with a small concentration of *n*-heptane. The profile closest to the critical point (represented by the red line in the figure) shows a very smooth transition from one phase to another and is nearly symmetric. Farther from the critical point (represented by the black line in Fig 6.14), the very slight increase asymmetry in the direction of the high density or liquid phase (- *z*) is hardly noticeable increases in the high density or liquid.

6.6.3 Effect of Concentration on Asymmetry in Density Profiles

The second property to be analyzed is the effect of concentration on the asymmetry of the density profile. Mixtures of ethane at low concentrations of *n*-heptane (x_c = 0.0350, 0.0202 and 0.0087) at a constant temperature distance $\Delta\hat{T} = -10^{-2}$ were used in this model, shown in Fig. 6.15. The methodology and equations used here is the same as that described in Section 6.6.2. The density profile of pure ethane (shown by the dashed red line) was also included for comparison to see if any asymmetry appeared due to the addition of *n*-heptane. The method used to create this plot is the same as described earlier in this section.

Based on the results in Fig. 6.15, it can be seen that concentration has a large effect on the behavior of the density profile. In general, as the concentration of *n*-heptane increases, the density in the bulk liquid phase ($z \ll 1$) decreases and the concentration in the bulk vapor phase ($z \gg 1$) decreases relative to the density profile of pure ethane (broken curved red line).

The temperature correction due to concentration in Eq. (5.4.2) is a significant factor in this result. Due to the steep slope of dT_c / dx in dilute *n*-heptane-ethane solutions (Table 6.8), Fisher Renormalization imposes a significant correction factor, causing a large relative reduction in the values of the temperature distance. This is because the renormalization occurs along a specific path when both the total volume and concentration are kept constant. Since the renormalization causes a decrease in temperature distance, the profiles to become smoother as these new and corrected temperatures are smaller and closer to the critical point. However, if the critical temperature is approached at a constant chemical potential or pressure, this effect is absent.

Despite the effect of Fisher Renormalization, some asymmetry can still be observed in Fig. 6.15. Given the difference in behavior between the density profiles of pure ethane (broken curved red line) and the *n*-heptane-ethane mixture with a concentration of $x_{C7} = 0.0350$ (curved blue line), there is increased asymmetry with higher concentrations of *n*-heptane. This effect is highlighted when considering the shift in the density profiles relative to the shift in critical density. In Fig. 6.15, the horizontal dashed red line represents the critical density of pure ethane and the dashed blue line indicates the critical density of the *n*-heptane-ethane mixture with a concentration of $x_{C7} = 0.0350$. By close examination, we can see in Fig. 6.15 that the difference in density between the critical and bulk vapor phase, relative to the difference between the critical and bulk liquid phase, increases with higher concentrations of *n*-heptane.

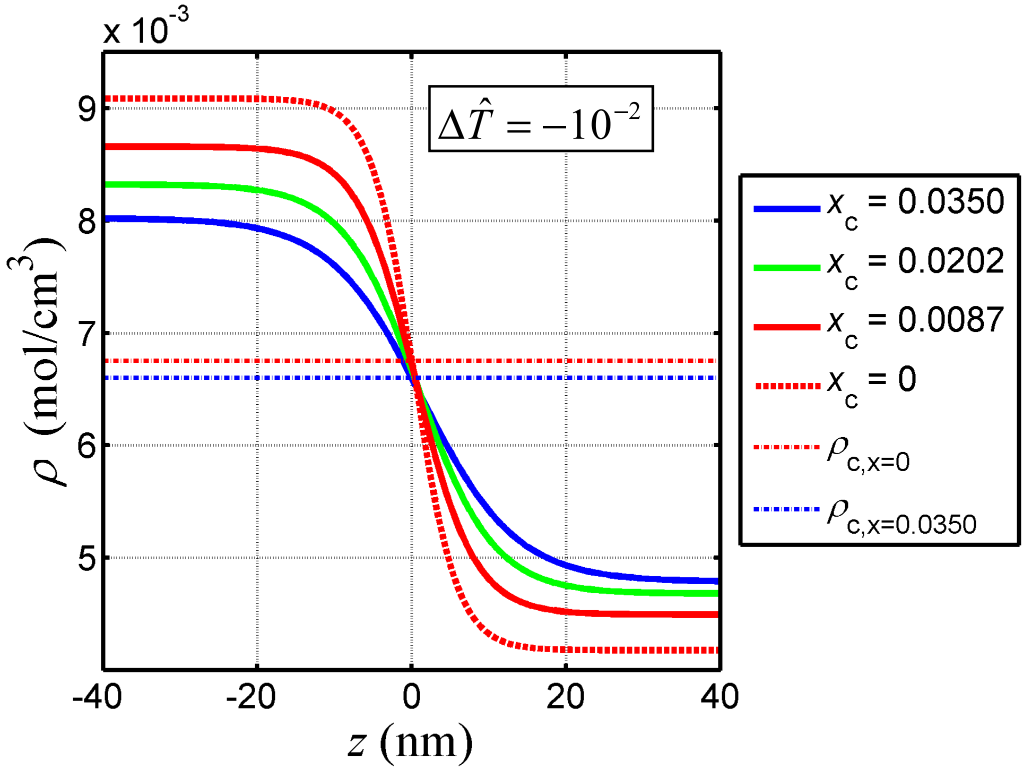

Figure 6.15. Density profiles for ethane and *n*-hepane in ethane at the vapor-liquid interface, at a constant temperature distance $\Delta\hat{T} = -10^{-2}$, and at various critical concentrations, plotted with respect to height (*z*-coordinate). Eqs. (5.2.1), (5.5.2), (5.5.3), (5.6.10), (5.6.11), (5.6.13) and (5.4.2) and experimental data from Tables 6.2 and 6.7 were used to model the behavior of the mixture. The critical density of ethane is indicated by the horizontal dotted red line and critical density for a solution with $x_{c,C7} = 0.0350$ is indicated by the horizontal dotted blue line.

However, since Fisher Renormalization significantly affects mixtures of *n*-heptane-ethane, this correction factor will be removed in the following analysis. In this specific case, the temperature distance will be held constant for all concentrations, at $\Delta\hat{T}(x) = \Delta\hat{T}(\mu) = -10^{-2}$, in order to better examine the effect of concentration on the density profiles. This result can be seen in Fig. 6.16. The same methodology was used to model these profiles as used in the previous two sections, only Fisher Renormalization in Eq. (5.4.2) was not applied in this case.

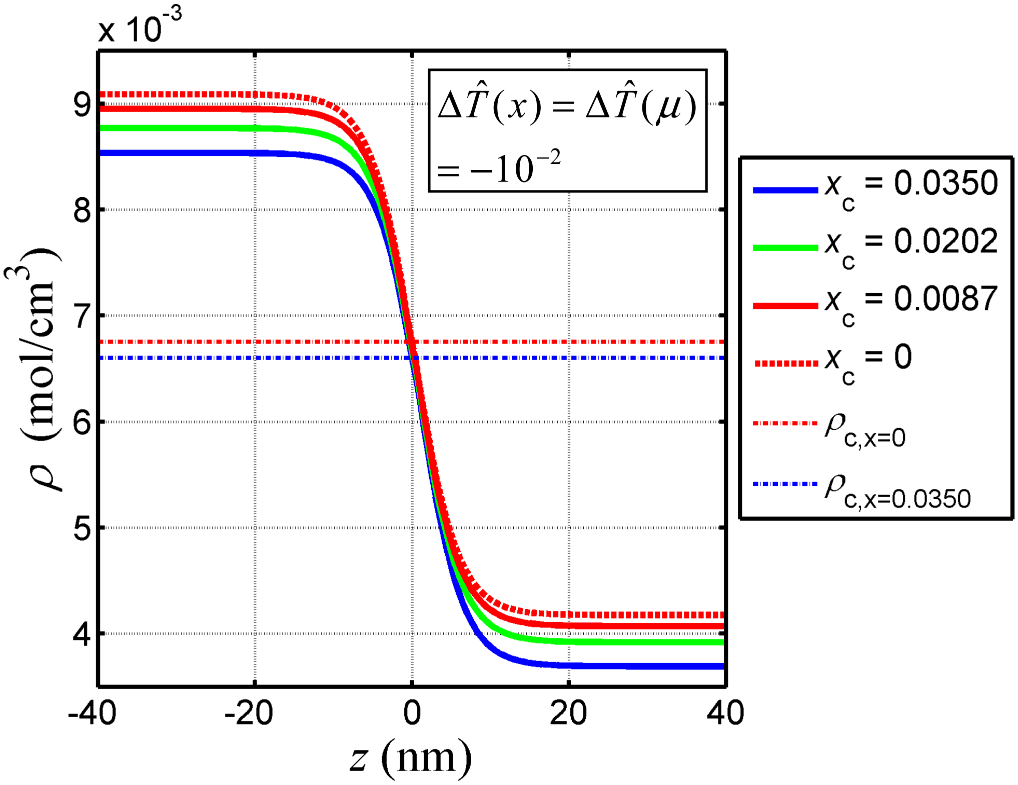

Figure 6.16. Density profiles for ethane and *n*-hepane in ethane at the vapor-liquid interface, at a constant temperature distance $\Delta\hat{T}(x) = \Delta\hat{T}(\mu) - 10^{-2}$ (without Fisher Renormalization), and at various critical concentrations, plotted with respect to height (*z*-coordinate). Eqs. (5.2.1), (5.5.2), (5.5.3), (5.6.10), (5.6.11), and (5.6.13), and experimental data from Tables 6.2 and 6.7 were used to model the behavior of the mixture. The critical density of ethane is indicated by the horizontal dotted red line and critical density for a solution with $x_{c,C7} = 0.0350$ is indicated by the horizontal dotted blue line.

When the temperature distance is held constant and considered independent of concentration, the density profiles shift to lower densities as greater amounts of *n*-heptane is added to ethane, as expected, which is shown in Fig. 6.16. Both bulk liquid and vapor phases exhibit a reduction in density with the addition of solute, as *n*-heptane has a larger molecular volume relative to ethane. From Fig. 6.16 we can see that as concentration is increased, there is a much larger deviation from the critical density in both bulk liquid and vapor phases as concentration of *n*-heptane is increased.

6.7 Conclusions

Compete scaling has been successfully employed to describe the physical behaviors of real one-component and dilute solutions by using experimental data to apply the effects of fluid asymmetry through scaling coefficients. Both dilute binary mixtures of aqueous *n*-hexane and *n*-heptane in ethane showed a change in concentration and density profile behavior, respectively, with increased concentration. The addition of a small amount of solute coupled with an increased temperature distance from the critical point resulted in the greatest increase in asymmetry in concentration profiles, as the solute favored one phase over the other. The addition of a small amount of *n*-heptane to ethane resulted in a shift in the density profiles to lower densities, as expected. An increase in *n*-heptane concentration also increased the asymmetry of the density profiles. However, an increase in temperature distance appeared to have little to no effect on density profiles.

Chapter 7: Summary and Outlook

In this work, complete scaling has been successfully applied to model the interfacial behavior of real asymmetric fluids and fluid mixtures. Selection of the order parameter and thermal scaling density to model asymmetric interfaces was based on a good knowledge of symmetric profiles, both mean-field and those that account for fluctuations near the critical point. By applying mean-field critical exponents, it was possible to determine the proper form of the thermal scaling density, as the mean-field behavior is well-known. Use of the symmetric renormalization group theory profile accounted for fluctuations near the critical point of separation.

In complete scaling, fluid asymmetry can be applied to symmetric profiles through the scaling coefficients of real one-component fluids. This method was used since it is impossible to directly minimize the free energy of an inhomogeneous asymmetric fluid and take into account critical fluctuations using another method. This is because scaling equations of state are not continuous through the unstable region, and therefore the corresponding free energy cannot be minimized in a simple manner.

When considering the behavior of the density profile of a one-component fluid or fluid mixture, the scaling coefficients a_3 and b_2 for dilute mixtures should be adjusted if there is a large difference in molecular volume between the solvent and solute. For polymer solutions, this difference in molecular volume is expressed by degree of polymerization, N. This study showed that a larger difference in molecular volume led to a higher degree of fluid asymmetry in polymer solutions, where the addition of larger molecules showed a preference for one phase over the other. The concentration of an added solute, specifically in dilute *n*-heptane-ethane solutions, caused shift in the profiles toward the density of the solute. This increased concentration of solute also contributed to asymmetry in density profiles.

When considering dilute mixtures, the scaling coefficients a_4 and b_4 can be approximated using experimental data in the linear portion of the critical locus of the mixture, which in most cases is only at dilute concentrations. Asymmetric concentration profiles for dilute mixtures of aqueous *n*-hexane and *n*-heptane-ethane were modeled in this work based on the approximation of a_4 and b_4 from experimental critical data of these dilute mixtures. This study showed that a very slight increase in concentration, coupled with an increasing temperature distance from the critical point of separation, yielded the greatest increase in fluid asymmetry in concentration profiles.

Directly related to the behavior of the interfacial profile is the curvature correction to the surface tension, or Tolman's length. This correction becomes very significant when the interface thickness is very large near the critical point as well as when there is a very high degree of fluid asymmetry. By utilizing complete scaling, this study showed that the Tolman's length becomes mesoscopic and diverges when approaching the critical point of separation ($\left|\Delta\hat{T}\right| \to 0$) and with increasing degree of polymerization ($N \to \infty$). The near-critical Tolman length will strongly diverge as $\sim N^{0.348}\left|\Delta\hat{T}\right|^{0.875}$. Farther from the critical point of separation in polymer solutions, when the phase diagram becomes more asymmetric, the Tolman length becomes a significant correction as it approaches the same magnitude as the width of the interface and diverges more strongly as $\sim \left|\Delta\hat{T}\right|^{-1}$, but is independent of N. Given these expressions for the general thermodynamic expression for near-critical Tolman length, crossover expressions to approximate the curvature correction based on Widom's characteristic variable, $w \equiv \frac{1}{2}\sqrt{N}\left|\Delta\hat{T}\right|$, and radius of gyration, $R_{\mathrm{g}} = r_0\sqrt{N}$.

In addition to the effects shown in polymer solutions, it is expected that Tolman's length will be a significant curvature correction to the surface tension of small droplets in highly asymmetric systems. There are many engineering applications that utilize asymmetric fluids and dilute fluid mixtures where this impact can be significant, such as the creation of nanodroplets, adsorption of small droplets on surfaces and microemulsions.

Two-dimensional phase-separated systems, such as Langmuir-Blodgett films, and separation on the surfaces of vesicles or small droplets, have many chemical and bioengineering applications. Since the results in this work for three-dimensional asymmetric systems have yielded a divergence of the Tolman length near the critical point for small curved surfaces, it is expected that an even greater effect will occur in two dimensions. Considering the expression for Tolman's length near the critical point in Eq. (4.2.20), it is apparent that the values of the critical exponents have a significant effect on the curvature correction to the line tension. Applying the critical exponents from the two dimensional Ising model,[56] the exponent for the first term is $\beta - \nu = -7/8$ and the exponent for the second term is $1 - \alpha - \beta - \nu = -1/8$. This result highlights that as the number of dimensions decreases, fluctuations near the critical point increase. These exponents suggest that the divergence of the Tolman length when approaching the critical point will be even greater than what has been presented in this research for three-dimensional systems, where $\beta - \nu \cong -0.304$ and $1 - \alpha - \beta - \nu \cong -0.065$.

Appendix A: Comparison of Mean-Field Surface Tension Calculations

As discussed in Chapter 2, the mean-field approximation for the surface tension was compared with both the work of Landau and Lifshitz[63] as well as the work of Rowlinson and Widom.[56] This section will describe the direct comparison between these results and those shown in this work.

A.1 Comparison with Landau and Lifshitz

Landau and Lifshitz[63] have provided a similar result for the local Helmholtz-energy density as shown in this work. We can make a comparison, beginning with their results[63] for the gradient of the order parameter in terms of specific volume, v (vice density, in our case),

$$\frac{dv}{dx} = \sqrt{\frac{\lambda}{\beta}}\left(v_0^2 - v^2\right) \qquad \text{(A.1.1)}$$

where x is the coordinate on which the order parameter is evaluated, β and λ are system-dependent constants analogous to our constants u_0 and c_0, and v_0 is the reference order parameter with respect to volume. This is Landau and Lifshitz's equation for the gradient of the order parameter that satisfies the stability requirements, similar to Eq. (2.2.2) in this work:

$$\frac{1}{4}u_0[\varphi^2 - \varphi_0^2]^2 = \frac{1}{2}c_0\left(\frac{d\varphi}{dz}\right)^2 \qquad \text{(2.2.2)}$$

which can be re-written as

$$\frac{d\varphi}{dz}=\left(\frac{u_0}{2c_0}\right)^{1/2}\left(\varphi^2-\varphi_0^2\right). \tag{A.1.2}$$

By evaluating the derivative expression in Eq. (A.1.1) , we obtain the profile for Landau and Lifshitz's order parameter,

$$v=v_0\tanh\left(v_0\sqrt{\frac{\lambda}{\beta}}x\right). \tag{A.1.3}$$

This result is similar to Eq. (2.2.3) in this work:

$$\frac{\varphi}{\varphi_0}=-\tanh\left[z\varphi_0\left(\frac{u_0}{2c_0}\right)^{1/2}\right]. \tag{2.2.3}$$

Note that the density-based order parameter profile in Eq. (2.2.3) is affected by height, where lower height, is in the $-z$ direction where the more dense of the two phases exists. In the case of Landau and Lifshitz[63] as shown above in Eq. (A.1.3), their profile does not assign the direction of the coordinate x.

Comparing Landau and Lifshitz's results in Eq. (A.1.3) and the result in Eq. (2.2.3), we can make a term-by-term comparison and obtain

$$\sqrt{\frac{\lambda}{\beta}}=\left(\frac{u_0}{2c_0}\right)^{1/2}. \tag{A.1.4}$$

Similar to the estimation of surface tension given in this work in Eq. (2.5.9) , Landau and Lifshitz's expression for the surface tension at the interface, a, is given as[63]

$$a=\frac{4}{3}\frac{\sqrt{\lambda\beta}}{V_{\mathrm{k}}}v_0^3, \tag{A.1.5}$$

where V_{k} is the critical volume. Given the relation provided in Eq. (A.1.4), assuming $\lambda=u_0/2$ and $\beta=c_0$, and assuming our density-based order parameter is similar to that of Landau and Lifshitz's specific volume-based order parameter, we can substitute our variables into Landau and Lifshitz's expression for surface tension Eq. (A.1.5) and make a comparison to Eq. (2.5.9) in this work, where

$$\frac{\sigma}{\rho_{\mathrm{c}} k_{\mathrm{B}} T_{\mathrm{c}}} = \frac{8}{3} \bar{\xi}_0^- \bar{C}_v \left(-\Delta\hat{T}\right)^{3/2}. \tag{2.5.9}$$

Noting also that

$$\varphi_0 = \left(\frac{a_0(-\Delta\hat{T})}{u_0} \right)^{1/2}, \tag{2.1.11}$$

$$\bar{\xi}_0^- = \left(\frac{c_0}{2a_0} \right)^{1/2}, \tag{2.2.6}$$

and

$$\bar{C}_V = \frac{a_0^2}{2u_0}, \tag{2.5.8}$$

we can substitute these values into Eq. (A.1.5) to compare to our expression for the dimensionless surface tension in Eq. (2.5.9). Therefore the expression for Landau and Lifshitz's surface tension for the mean-field approximation becomes

$$\frac{aV_{\mathrm{k}}}{k_{\mathrm{B}} T_{\mathrm{c}}} = \frac{8}{3} \bar{\xi}_0^- \bar{C}_V \left(-\Delta\hat{T}\right)^{3/2}, \tag{A.1.6}$$

when made dimensionless, which compares directly to the expression in Eq. (2.5.9).

A.2 Comparison with Rowlinson and Widom

Rowlinson and Widom[56] also discuss the behavior of interfaces near the critical point, defining the density near the critical point as:

$$\rho^{l,g} \sim \rho_c \pm \left[A(T-T_c)/B \right]^{1/2}. \tag{A.2.1}$$

Noting the definitions given in Eqs. (2.1.7) and (2.1.9)

$$\Delta\hat{T} \equiv \frac{T - T_{\mathrm{c}}}{T_{\mathrm{c}}} \qquad (2.1.7)$$

$$\varphi(z) \equiv \frac{\rho(z) - \rho_{\mathrm{c}}}{\rho_{\mathrm{c}}}, \qquad (2.1.9)$$

and the density difference along the liquid-gas coexistence curve can be defined as

$$\rho^{l} - \rho^{g} = 2\varphi_0 \rho_{\mathrm{c}}, \qquad (A.2.2)$$

we can determine the relationship between Rowlinson and Widom's[56] variables A and B in Eq. (A.2.1) and the variables in this work. Given these equations, this relation becomes:

$$\rho - \rho_{\mathrm{c}} = \rho_{\mathrm{c}} \left(\frac{a_0}{u_0} \frac{(T_{\mathrm{c}} - T)}{T_{\mathrm{c}}} \right)^{1/2} = \left(\frac{A}{B} (T_{\mathrm{c}} - T) \right)^{1/2}$$

$$\rho_c \left(\frac{a_0}{u_0 T_c} \right)^{1/2} = \left(\frac{A}{B} \right)^{1/2}$$

$$\frac{A}{B} = \frac{\rho_{\mathrm{c}}^2 a_0}{u_0 T_{\mathrm{c}}}. \qquad (A.2.3)$$

If we use the expansion of the chemical potential near the critical point developed by Rowlinson and Widom,[56]

$$\mu(\rho, T) - \mu = A(T - T_{\mathrm{c}})(\rho - \rho_{\mathrm{c}}) + B(\rho - \rho_{\mathrm{c}})^3 + \ldots, \qquad (A.2.4)$$

we can separate the coefficients A and B and determine their values. In terms of the dimensionless variables in this work, we can duplicate this expansion of the chemical potential as

$$\frac{\mu(\rho, T) - \mu}{k_{\mathrm{B}} T_{\mathrm{c}}} = a_0 \Delta\hat{T} \varphi + u_0 \varphi^3, \qquad (A.2.5)$$

which can also be written with dimensions

$$\mu(\rho,T)-\mu=\frac{k_{\mathrm{B}}a_0}{\rho_{\mathrm{c}}}\left(T-T_{\mathrm{c}}\right)\left(\rho-\rho_{\mathrm{c}}\right)+\frac{k_{\mathrm{B}}T_{\mathrm{c}}u_0}{\rho_{\mathrm{c}}^3}\left(\rho-\rho_{\mathrm{c}}\right)^3. \tag{A.2.6}$$

A comparison of each term in Rowlinson and Widom's expansion of the chemical potential[56] in Eq. (A.2.4) to the substitution of the variables in this work, shown in Eq. (A.2.6), gives the solution

$$\begin{aligned} A&=\frac{a_0k_{\mathrm{B}}}{\rho_{\mathrm{c}}} \\ B&=\frac{u_0k_{\mathrm{B}}T_{\mathrm{c}}}{\rho_{\mathrm{c}}^3}. \end{aligned} \tag{A.2.7}$$

This result can be verified with Eq. (A.2.3).

Following this same method of comparing terms, we can also look to Rowlinson and Widom's expression for the chemical potential difference at the interface of two fluids, related to the density gradient,[56]

$$m\frac{d^2\rho}{dz^2}=\mu(\rho,T)-\mu\,, \tag{A.2.8}$$

where $\mu(\rho,T)$ is the chemical potential in the homogeneous fluid of density ρ from the mean-field approximation and μ is the chemical potential in the two-phase region. We can compare this equation the expression for the chemical potential in Eq. (2.2.1) of this work,

$$\frac{\mu(z)}{k_{\mathrm{B}}T_{\mathrm{c}}}=u_0\varphi\left(\varphi^2-\varphi_0^2\right)+c_0\frac{d^2\varphi}{dz^2}\,, \tag{2.2.1}$$

re-writing Eq. (2.2.1) in the same form as Eq. (A.2.8) to yield the expression

$$c_0k_{\mathrm{B}}T_{\mathrm{c}}\frac{d^2\varphi}{dz^2}=\mu(z)-u_0k_{\mathrm{B}}T_{\mathrm{c}}\varphi\left(\varphi^2-\varphi_0^2\right). \tag{A.2.9}$$

Noting that

$$\frac{d^2\varphi}{dz^2} = \frac{1}{\rho_c}\frac{d^2\rho}{dz^2},$$

Eq. (A.2.9) becomes

$$\frac{c_0 k_\mathrm{B} T_\mathrm{c}}{\rho_\mathrm{c}}\frac{d^2\rho}{dz^2} = \mu(z) - u_0 k_\mathrm{B} T_\mathrm{c}\varphi\left(\varphi^2 - \varphi_0^2\right). \tag{A.2.10}$$

By a term-by-term comparison, we find

$$m = \frac{c_0 k_\mathrm{B} T_\mathrm{c}}{\rho_\mathrm{c}}. \tag{A.2.11}$$

Since we have determined the values of the unknown constants in Eqs. (A.2.7) and (A.2.11), and the difference in density along the coexistence curve in Eq. (A.2.2), we can substitute these constants and relation into Rowlinson and Widom's expression for the surface tension near the critical point,[56]

$$\sigma = \frac{1}{6}\left(\frac{mB}{2}\right)^{1/2}\left(\rho^l - \rho^g\right)^3. \tag{A.2.12}$$

Eq. (A.2.12) can be re-written in terms of mean-field variables in this work, which provides the same result as Eq. (2.5.9):

$$\frac{\sigma}{\rho_\mathrm{c} k_\mathrm{B} T_\mathrm{c}} = \frac{8}{3}\bar{\xi}_0^- \bar{C}_v (-\Delta\hat{T})^{3/2}. \tag{2.5.9}$$

References

1. J.W. Gibbs, *Collected Works* (Dover, New York, 1961).

2. R.C. Tolman, *J. Chem. Phys*. **17**, 333 (1949).

3. E.M. Blokhuis,. "Liquid drops at surfaces," in *Surface and Interfacial Tension* (Marcel Dekker, New York, 2003), pp. 149-193.

4. J. Israelachvili, *Intermolecular and Surface Forces*, 2nd ed. (Academic Press, London, 1992).

5. M. Daud, and C.E. Williams, editors, *Soft Matter Physics* (Springer, Berlin, 1999).

6. I.W. Hamley, *Introduction to Soft Matter,* 2nd ed. (J. Willey, Chichester, 2000).

7. R.A.L. Jones, *Soft Condensed Matter* (Oxford University Press, Oxford-New York, 2002).

8. M.A. Anisimov, "Thermodynamics at the Meso- and Nanoscale," in *Dekker Encyclopedia of Nanoscience and Nanotechnology*, edited by J.A. Schwarz, C. Contescu, and K. Putyera (Marcel Dekker, New York, 2004), pp. 3893-3904.

9. R.A.L. Jones and R.W. Richards, *Polymers at Surfaces and Interfaces* (Cambridge University Press, Cambridge-New York, 2006).

10. R.A. Adomaitis, *Computers and Chemical Engineering* **26,** 981 (2002).

11. J. Chen and R.A. Adomaitis, *Computers and Chemical Engineering* **30,** 1354 (2006).

12. W.R. Gombotz and D.K. Pettit, *Bioconjugate Chem.* **6**, 332 (1995).

13. A.V. Reis, M.R. Guilherme, A.T. Paulino, E.C. Muniz, L.H.C. Mattoso and E.B Tambourgi, *Langmuir* **25**, 2473 (2009).

14. P.B. O'Donnell and J.W. McGinty, *Adv. Drug Deliv. Rev.* **28**, 25 (1997).

15. W. Balachandran, P. Miao and P. Xiao, *J. Electrostatics* **50**, 249 (2001).

16. J.G. Kirkwood and F.P. Buff, *J. Chem. Phys*. **17**, 338 (1949).

17. F.O. Koenig, *J. Chem. Phys.* **18**, 449 (1950).

18. D.S. Choi, M.S. Jhon and H. Eyring, *J. Chem. Phys.* **53**, 2608 (1970).

19. J.S. Rowlinson, *J. Phys. A* **17**, L357 (1984).

20. M.J.P. Nijmeijer, C. Bruin, A.B. Woerkom, A.F. Bakker, and J.M.J. van Leeuwen, *J. Chem. Phys.* **96**, 565 (1992Π>

21. E.M. Blokhuis and D. Bedeaux, *HCR Advanced-Education Review*, (Wiley, New York, 1994).

22. I. Hadjiagapiou, *J. Phys. Condens. Matter* **6**, 5303 (1994).

23. M.J. Haye and C. Bruin, *J. Chem. Phys*. **100**, 556 (1994Π>

24. V. Talanquer and D.W. Oxtoby, *J. Phys. Chem.* **99**, 2865 (1995).

25. R. McGraw and A. Laaksonen, *J. Chem. Phys.* **106**, 5284 (1997).

26. L.J. Gránásy, *J. Chem. Phys*. **109**, 9660 (1998).

27. K. Koga, X.C. Zeng and A.X. Shchekin, *J. Chem. Phys*. **109**, 4063 (1998).

28. P.R. ten Wolde and D. Frenkel, *J. Chem. Phys*. **109**, 9901 (1998).

29. M.P. Moody and P. Attard, *J. Chem. Phys.* **115**, 8967 (2001).

30. I. Napari and A. Laaksonen, *J. Chem. Phys.* **114**, 5796 (2001).

31. E. Santiso and A. Firoozabadi, *AIChE J.* **52**, 311 (2006).

32. A.H. Falls, L.E. Scriven and H.T. Davis, *J. Chem. Phys.* **75**, 3986 (1981).

33. S.M. Thompson, K.E. Gubbins, J.P.R.B. Walton, R.A.R. Chantry, and J. S. Rowlinson, *J. Chem. Phys*. **81**, 530 (1984).

34. R. Guermeur, F. Biguard and C. Jacolin, *J. Chem. Phys.* **82**, 2040 (1985).

35. J.S. Rowlinson, *Pure & Appl. Chem*. **59**, 15 (1987).

36. E.M. Blokhuis and D. Bedeaux, *J. Chem. Phys*. **97**, 3576 (1992).

37. J.S. Rowlinson, *J. Phys.: Condens. Matter* **6**, A1 (1994).

38. L.S. Bartell, *J. Phys. Chem. B*. **105**, 11615 (2001).

39. T.V. Bykov and X.C. Zeng, *J. Phys. Chem. B* **105**, 11586 (2001).

40. Y.A. Lei, T. Bykov, S. Yoo and X.C. Zeng, *J. Am. Chem. Soc.* **127**, 15346 (2005).

41. H.M. Lu and Q. Jiang, *Langmuir* **21**, 778 (2005).

42. J.C. Barrett, *J. Chem Phys*. **124**, 144705 (2006).

43. E.M. Blokhuis, and J. Kuipers, *J. Chem. Phys.* **124**, 074701 (2006).

44. A.E. van Giessen, E.M. Blokhuis and D.J. Bukman, *J. Chem. Phys.* **108**, 1148 (1998).

45. M.A. Anisimov, *Phys. Rev. Lett*. **98**, 035702 (2007).

46. T.D. Lee and C.N. Yang, *Phys. Rev*. **87**, 410 (1952).

47. M.E. Fisher, *Rep. Prog. Phys* **30**, 615 (1967).

48. J. V. Sengers and J. M. H. Levelt Sengers, in *Progress in Liquid Physics*, edited by C. A. Croxton, (Wiley, Chichester, UK, 1978), p. 103.

49. M.E. Fisher and G. Orkoulas, *Phys. Rev. Lett.* **85**, 696 (2000).

50. Y.C. Kim, M.E. Fisher and G. Orkoulas, *Phys. Rev. E* **67**, 061506 (2003).

51. J.T. Wang, C.A. Cerdeiriña, M.A. Anisimov and J.V. Sengers, *Phys. Rev. E* **77**, 031127 (2008).

52. S. Safran, Statistical *Thermodynamics of Surfaces, Interfaces, and Membranes* (Perseus Books, Cambridge, MA, 1994).

53. M.M. Kleman and O.D. Lavrentovich, *Soft Matter Physics: An Introduction* (Springer, New York, 2003).

54. J.D. van der Waals, *J. Stat. Phys.* **20**, 197 (1979). (English transl.)

55. L.D. Landau and. E.M. Lifshitz, *Statistical Physics* 3rd ed. Part 1, translated from Russian by J.R. Sykes and M.J. Kearsley (Butterworth-Heinemann, Oxford, 1980).

56. J.S. Rowlinson and B. Widom, *Molecular Theory of Capillarity* (Clarendon, Oxford, 1982).

57. A. Kostrowicka Wyczalkowska, J.V. Sengers and M.A. Anisimov, *Physica A* **334**, 482 (2004).

58. V. A. Agayan, Ph.D. Thesis, Univeristy of Maryland (2000).

59. A. Z. Patashinskii and V. L. Pokrovskii, *Fluctuation Theory of Phase Transitions* (Pergamon, Oxford, 1979Π>

60. M.A. Anisimov and J.V. Sengers, “Critical Region,” *in Equations of State for Fluids and Fluid Mixtures* edited by J.V. Sengers, R.F. Kayser, C.J. Peters and H.J. White (Elsivier, Amsterdam, 2000), pp. 381-434.

61. J.V. Sengers and J.M.J. van Leeuwen, *Phys. Rev. A.* **39**, 6346 (1989).

62. J.T. Wang, Ph.D. Thesis, University of Maryland (2006).

63. L.D. Landau and E.M. Lifshitz, *Statisticheskaya fizika (Statistical Physics)*, (Nauka, Moscow, 1944) . [In Russian]

64. M.A. Anisimov, *Critical Phenomena in Liquids and Liquid Crystals* (Gordon and Breech Science Publishers, Philadelphia, 1991).

65. R. Lovett, P.W. DeHaven, J.J. Vieceli and F.P. Buff, *J. Chem. Phys*. **58**, 1880 (1973).

66. R. Lovett, C.Y. Mou and F.P. Buff, *J. Chem. Phys.* **65**, 570 (1976).

67. R. Lovett and M Baus, *J. Chem. Phys.* **111**, 5544 (1999).

68. J.T. Wang and M.A. Anisimov, *Phys. Rev. E* **75**, 051107 (2007).

69. M.E. Fisher, “Scaling, universality, and renormalization group theory,” in Lecture Notes in Physics, edited by F.J.W. Hahne, vol. 186, 1 (Springer, Berlin, 1982).

70. M.E. Fisher and S.-Y. Zinn, *J. Phys. A.* **31**, L629 (1998).

71. A. Pelisetto and E. Vicari, *Physics Reports* **368**, 549 (2002).

72. M.E. Fisher, *J. Math. Phys*. **5**, 944 (1964).

73. H. Behnejad, J.V. Sengers and M.A. Anisimov, “Thermodynamic behavior of fluids near critical points.” (unpublished)

74. S.C. Greer and M.R. Moldover, *Annu. Rev. Phys. Chem.,* 32, 233 (1981).

75. J.V. Sengers and J.M.H. Levelt Sengers, *Annu. Rev. Phys. Chem.* **37**, 189 (1986).

76. A. Haupt and J. Straub, *Phys. Rev. E*, **59**, 1795 (1999).

77. R. Guida and J. Zinn-Justin, *J. Phys. A.* **31**, 8103 (1998).

78. M.A. Anisimov, E.E. Gorodetskii, V.D. Kulikov and J.V. Sengers, *Phys. Rev. E* **51**, 1191 (1995).

79. C.A. Cerdeiriña, M.A. Anisimov and J.V. Sengers, *Chem. Phys. Lett.* **424**, 414 (2006).

80. T. Ohta and K. Kawasaki, *Prog. Theor. Phys*. **58**, 467 (1977).

81. S-Y. Zinn, Ph.D. Thesis, University of Maryland, College Park (1997).

82. A.J. Liu and M.E. Fisher, *Physica A* **156** 35 (1989).

83. H. Chaar, M.R. Moldover and J.W. Schmidt, *J. Chem. Phys.* **85**, 418 (1986).

84. S. Middleman, *An Introduction for Fluid Dynamics: Principles of Analysis and Design* (Wiley, New York, 1998), p. 42.

85. M. Mareschal and M. Baus, *J. Chem. Phys.* **106**, 645 (1997).

86. H. El Bardouni, M. Mareschal, R. Lovett, and M. Baus, *J. Chem. Phys*. **113**, 9804 (2000).

87. Z. Li and J. Wu, "Toward a Quantitative Theory of Ultrasmall Liquid Droplets and Vapor—Liquid Nucleation," *Ind. Eng. Chem. Res.,* 10.1021/ie070578i (2007).

88. E. M. Blokhuis and D. Bedeaux, *J. Chem. Phys*. **97**, 3576 (1992).

89. W. Helfrich, *Z. Naturforsch.* **28c**, 693 (1973).

90. S.H. Park, J.G. Weng and C.L. Tien, *Int. J. Heat Mass Transfer* **44**, 1849 (2001).

91. A.E. van Giessen and E.M. Blokhuis, *J. Chem. Phys.* **116**, 302 (2002).

92. P. Phillips and U. Mohanty, *J. Chem. Phys.* **83**, 6392 (1985).

93. M.P.A. Fisher and M. Wortis, *Phys. Rev. B* **29**, 6252 (1984).

94. B. Widom and J.S. Rowlinson, *J. Chem. Phys.* **52**, 1670 (1970).

95. M.A Anisimov and J.T. Wang, *Phys. Rev. Lett.* **97**, 25703 (2006).

96. Y. C. Kim, Ph.D. Thesis, University of Maryland (2002).

97. B. Widom, *Physica A* **194**, 532 (1993).

98. A.A Povodyrev, M.A. Anisimov and J.V. Sengers, *Physica A* **264**, 345 (1999).

99. P.J. Flory, *Principles of Polymer Chemistry* (Cornell University Press, Ithaca, 1953).

100. T. Dobashi, M. Nakata and M. Kaneko, *J. Chem. Phys.* **72**, 6685 (1980).

101. M.A Anisimov, A.F. Kostko, J.V. Sengers and I.K. Yudin, *J. Chem. Phys*. **123**, 164901 (2005).

102. M.E. Fisher, "Scaling, universality, and renormalization group theory," in Lecture Notes in Physics, edited by F.J.W. Hahne, vol. 186, 1 (Springer, Berlin, 1982).

103. P.G. de Gennes, *Scaling Concepts in Polymer Physics* (Cornell University Press, Ithaca, 1979).

104. M.A. Anisimov and H.J. St. Pierre, *Phys. Rev. E* **78**, 011105 (2008).

105. M.A. Anisimov and J.V. Sengers, *Mol. Phys.* **103**, 3061 (2005).

106. I. Szleifer and B. Widom, *J. Chem. Phys.* **90**, 7524 (1989).

107. D. Broseta, *Polymer* **35**, 2237 (1994).

108. F.A.M Leermarkers, P.A. Barneveld, J. Sprakel and F.A.M. Besseling, *Phys. Rev. Lett*. **97**, 066103 (2006).

109. F.A.M Leermarkers, P.A. Barneveld, J. Sprakel and F.A.M. Besseling, Leermarkers *et al.* Reply to Comment on "Symmetric Liquid-Liquid Interface with a Nonzero Spontaneous Curvature," *Phys. Rev. Lett.* **98**, 039602 (2007).

110. J. van Male and E.M. Blockhuis, Comment on "Symmetric Liquid-Liquid Interface with a Nonzero Spontaneous Curvature," *Phys. Rev. Lett*. **98**, 039601 (2007).

111. J.M.H Levelt Sengers, J. Straub, K. Wantanabe, and P.G. Hill, *J Phys. Chem. Ref. Data* **14**,193 (1985).

112. M. Bonetti and P. Calmettes. “Small-angle neutron scattering from heavy water in the vicinity of the critical point.” In *Steam, Water, and Hydrothermal Systems: Physics and Chemistry Meeting the Needs of Industry. Proceedings of the 13th International Conference on the Properties of Water and Steam.*, edited by P.R. Temaine, P.G. Hill, D.E. Irish and P.V. Balakrishnan, (NRC Research Press, Ottowa, 2000) p 347.

113. C.E. Harmin and G. Thodos, *J. Chem. Eng. Data* **11**, 202 (1966).

114. D. Ambrose and C. Tsonopoulos, *J. Chem. Eng. Data* **40**, 531 (1995).

115. P.Y. Bruice, *Organic Chemistry*, 2nd Ed. (Prentence Hall, Upper Saddle River, 1998), p. 305.

116. M.L. Bradford and G. Thodos, *J. Chem. Eng. Data* **12**, 373 (1967).

117. M.E. Fisher, *Phys. Rev.* **176,** 257 (1968).

118. M.A. Anisimov, E.E. Gorodetskii, V.D. Kulikov, A.A. Povodyrev and J.V. Sengers, *Physica A* **220**, 277 (1995).

119. Th. W. De Loos, W.G. Penders, R.N. Lichtenthaler, *J. Chem Thermodyn.*, **14**, 83 (1982).

120. I. Abdulagatov, NIST, Boulder (private communication).

121. T. Yiling, Th. M. Michelberger, E.U. Franck, *J. Chem. Thermodyn.* **23**, 105 (1991).

122. J.T. Wang, M.A. Anisimov and J.V. Sengers, *Z. Phys. Chem.* **219**, 1273 (2005).

123. E. Brunner, *J. Chem. Thermodyn.* **22**, 335 (1990).

124. C.J. Rebert and K.E. Hayworth, *AIChE J.* **13**, 118 (1967).

125. H. Singh, F.P. Lucien and N.R. Foster, *J. Chem. Eng. Data* **45**, 131 (2000).

126. V.S. Mehra and G. Thodos, *J. Chem. Eng. Data* **10**, 211 (1965).

127. M.A. Anisimov, E.E. Gorodetskii and N.G. Shmakov, *Soviet Physics JETP* **36**, 1143 (1973).